CHALMERS
UNIVERSITY OF TECHNOLOGY

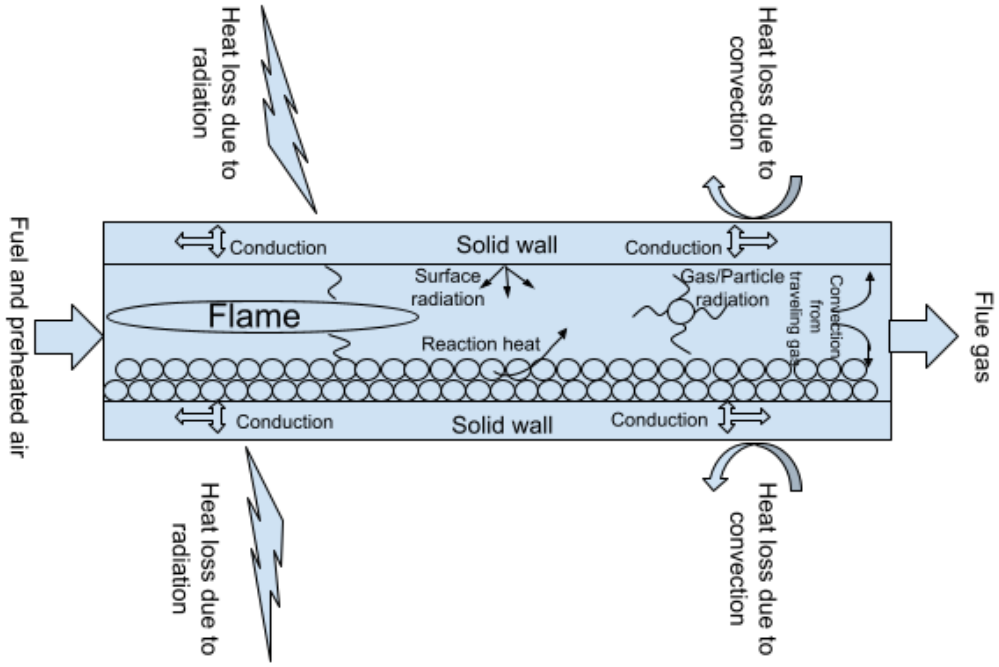

A modelling heat transfer study of a hydrogen flame in the iron ore pelletization process

An evaluation of the rotary kiln process

Master's thesis in Master Programme Sustainable Energy Systems

ELIAS EHLMÉ

DEPARTMENT OF Space, Earth and Environment

CHALMERS UNIVERSITY OF TECHNOLOGY
Gothenburg, Sweden 2022
www.chalmers.se

DEPARTMENT OF Space, Earth and Environment
CHALMERS UNIVERSITY OF TECHNOLOGY
Gothenburg, Sweden 2022
www.chalmers.se

A modelling heat transfer study of a hydrogen flame in the iron ore pelletization process

An evaluation of the rotary kiln process

Elias Ehlmé

CHALMERS
UNIVERSITY OF TECHNOLOGY

Department of Space, Earth and Environment
Division of Energy Technology
Chalmers University of Technology
Gothenburg, Sweden 2022

A modelling heat transfer study of a hydrogen flame in the iron ore pelletization process
An evaluation of the rotary kiln process
Elias Ehlmé

Supervisors: Adrian Gunnarsson, Department of Space, Earth and Environment, Fredrik Normann and Samuel Colin, LKAB.
Examiner: Klas Andersson, Department of Space, Earth and Environment

Master's Thesis 2022
Department of Space, Earth and Environment
Division of Energy Technology
Chalmers University of Technology
SE-412 96 Göteborg
Sweden
Telephone + 46 (0)31-772 1000

Cover: Figure of the rotary kiln with the pellets bed, flame, and heat transfer mechanisms.

Typeset in Microsoft Word.
Printed by Chalmers Reproservice
Gothenburg, Sweden 2022

A Heat Transfer Modelling study of a Hydrogen Flame in The Iron Ore Pelletization Process
An Evaluation of The Rotary Kiln Process
Elias Ehlmé
Department of Space, Earth and Environment
Chalmers University of Technology

Abstract

The supplied heat needed in the heat treatment of iron ore pellets commonly originates from fossil fuels that generate considerable emissions of greenhouse gases. Hence, there is a need for such mining industries to find possible solutions in order to reduce their emissions. One such company is Luossavaara-Kiirunavaara Aktiebolag, (LKAB), which is examining the suitability of a transition from combusting coal to hydrogen gas in the rotary kiln, used for a portion of their product. Their aim is by switching from coal to hydrogen, reach the climate targets set by LKAB and the Swedish government. Since such process changes may affect how the kiln should be operated it is of interest to examine the process changes with the use of modeling tools. This master thesis work focuses on examining the heat transfer conditions in a rotary kiln, using hydrogen gas by further developing a heat transfer model of a coal flame in a rotary kiln, developed at the division of Energy Technology at Chalmers University of Technology. By conducting sensitivity analyses of several parameters such as the gas temperatures, flame dimensions, and addition of coal or iron ore dust particles to the flame, suggestions on how the kiln should be operated to mimic a coal or oil flame may be evaluated.

One of the main challenges with substituting coal for hydrogen is the reduced thermal radiation from char, ash, and soot particles as well as carbon dioxide in the kiln. These components dominate the heat transfer in the kiln as they absorb, emit, and scatter radiation, hence promoting heat transfer by radiation to the pellets, which lie like a bed within the kiln. As heat transfer is reduced, flue gas temperatures increase, which leads to increased heat losses and may also lead to an uneven heat transfer load to the pellet bed, which is undesired with respect to the quality of the pellets.

The results show that by increasing the gas temperatures of the preheated air, or by adding particles, a hydrogen flame that assumes an adiabatic temperature profile, may deliver a heat transfer to the bed material similar to an oil or coal flame, respectively. However, an uneven heat load further remains an issue. The addition of particles in the extreme environment significantly influenced the emittance of radiation, resulting in elevated kiln wall temperatures, which may cause further complications in the kiln. This master thesis work concludes that while further research in the mentioned areas is required, the results may be used to evaluate the implementation of a hydrogen flame in a rotary kiln.

Keywords: Iron ore pelletizing process, rotary kiln, hydrogen combustion, radiation, heat transfer

Acknowledgements

A special thanks for the active and great level of communication from Klas Andersson and Adrian Gunnarsson, which has kept me continuously motivated and inspired and will continue to do so. Thank you, Adrian, my supervisor, for all the support, feedback, and interesting discussions. My gratitude to Klas for the opportunity to work on such an interesting topic.

Furthermore, I would like to thank my assistant supervisor Fredrik Normann as well as Samuel Colin at LKAB, for sharing process data, insight, guidance, and feedback regarding the grate-kiln process at LKAB throughout our many meetings.

Elias Ehlmé, Gothenburg, May 2022

Contents

1.

Introduction

1.1 Background

New targets are constantly being set to reduce emissions related to fossil fuel combustion and the impact on global warming in order to reach a sustainable future in a sustainable society. One such target that has been set is Sweden's national target of net-zero emissions of carbon dioxide by 2045 [1]. Thus, there is a need for heavy emitting industries, which are today dependent on fossil fuels, to transition to other renewable fuel sources. One such alternative fuel is hydrogen gas, which will mainly produce water vapor after combustion and may be considered renewable if produced using electricity from renewable sources such as solar, water, or wind power.

Luossavaara-Kiirunavaara Aktiebolag, LKAB, which is owned by the Swedish state, is a mining company that is considered to be the fourth largest emitter of CO_2 in Sweden [2]. Their emissions originate from the heating and processing of raw iron ore to produce high-quality iron ore pellets, which are sold worldwide [3]. As one of the largest emitters of CO_2 in Sweden, the company continuously strives and aims to further develop sustainable and high-quality iron ore products [2], [3]. One current goal set by LKAB is to develop carbon dioxide-free processes and products by the year 2045. Furthermore, LKAB participates in the HYBRIT project, which is a collaborative project that started in 2016 by the companies LKAB, SSAB, and Vattenfall, and aims to replace coal as a heating supply for steel processing with hydrogen gas [4], [5]. Within the project, LKAB's challenge and contribution are to exchange the heat supply in their pelletizing production, to a fossil-free fuel, and one such fuel that is of large interest is hydrogen gas. By achieving the targets from the HYBRIT project, Sweden will reduce their carbon dioxide emissions by 10% [6].

For a portion of LKAB's product, a rotary kiln is used, and is today heated using a jet-like fossil coal flame. Hence, there is a large interest in replacing this coal flame with, e.g., a hydrogen gas flame to lower the related emissions. However, replacing the heat supply could affect how the kiln should be operated since the production of high-quality pellets are dependent on several parameters, where one of the key factors is the heat transfer conditions within the kiln. Due to the rotation of the kiln, which complicates measurements, there is a lack of knowledge regarding the current heat transfer conditions. During combustion, heat is transferred from the flame due to convection, conduction, and radiation. At the high temperatures within the kiln, heat will be more effectively transferred from radiation, hence the radiative heat transfer dominates in the kiln. Therefore, it is of interest to model and study the radiative heat transfer from the flame to the bed material in the kiln. Thus, this master thesis aims to examine the effects on the iron ore pellet bed in the rotary kiln as the fuel is changed from fossil coal to hydrogen gas, by using, and to further develop, an existing in-house heat transfer modeling tool of a rotary kiln. The possible options to reduce LKAB's emissions will be evaluated by conducting sensitivity analyses of several design parameters. To validate the model, measurement data from pilot-scale furnaces using hydrogen flames from LKAB will be used, if time and resources allow. Since such process changes are expensive and could affect how the process should be operated, it is of interest to examine the process change with the use of modeling tools.

In this master thesis work, such a possibility shall be examined by increasing the understanding of the heat transfer by using a hydrogen gas flame and to further examine suggestions for how the industrial process could be operated.

1.2 Aim

The aim of this master thesis work is to further develop a heat transfer modeling tool of a rotary kiln to examine the effects on the iron ore pellets bed in the kiln, as the combustion fuel is changed from a fossil coal flame to a hydrogen gas flame. The modeling tool will be used to conduct sensitivity analyses of several parameters to study the effects on the heat transfer conditions from the flame to the pellets bed. This, in order to evaluate and find possible options to reduce LKAB's emissions of carbon dioxide.

1.3 Limitations

This master thesis work will only focus on the pellets in the rotary kiln section in the grate-kiln process, i.e, not the grate or cooler sections. Other limitations in this project include:

- The master thesis will mainly focus on the combustion fuels, hydrogen gas, oil and coal.
- This master thesis work do not examine the effects of combustion nor the propagation of the flame.
- The theoretical evaluation on the effect of replacing combustion fuel with hydrogen gas will not include the production of hydrogen gas, nor the practical aspects regarding the suggested process operations.
- This master thesis work do not discuss the emissions of NO_x, which may increase with higher flame temperatures. However, one should be aware of such possibilities when evaluating the combustion of hydrogen gas.

1.4 Specific scope of the thesis

The master thesis work aims to describe the effects on the heat transfer conditions within the kiln as well as:

- The effects on the iron ore pellets bed in the rotary kiln as the combustion is changed from fossil coal to hydrogen gas.
- The sensitivity analyses of several parameters to examine if this change is a possible alternative to reduce LKAB's emissions of carbon dioxide.
- An increased understanding of the heat transfer using a hydrogen gas flame in a rotary kiln.
- Suggestions for how the process could be operated with a hydrogen gas flame.

2.

Theory

2.1 Production of iron pellets

The high-quality iron ore pellets that LKAB produces originate from the two main minerals-, magnetite-, and hematite, which also are the main minerals extracted in the LKAB mines [7]. The production sites and mines are located in Kiruna, Malmberget, and Svappavaara [8], where the concentration of magnetite ranges between 80% and 100% [7]. The iron ore pellets are mainly used for steel processing and are produced in such a pelletized form to facilitate transportation as well as to maintian the integrity of the product during transportation from LKAB sites to around the world [8].

To produce the high-quality pellets, impurities from the mined iron ore have to be removed, in order to increase the iron content [7]. This is done in several steps that include crushing the ore into coarse pieces, then transporting the ore into a sorting plant which sorts by, in summary, continuously grinding the ore while conducting magnetic separation [7], [9]. To further remove impurities the ore is transported to a concentration plant where the iron ore is further ground into a fine powder and the impurities are removed by several separation steps. The powder is then mixed with water, different additives depending on the desired properties of the pellets that are to be produced, as well as adding a binder. One such binder is bentonite and is used to form round balls which are, before the heat treatment process, called green pellets. The green pellets are formed in a rotating drum and have a diameter of approximately 9-15 mm [10]. Some of the additives and binders that are mixed with the iron ore are presented in Table 2.1 [9].

Table 2.1: Additives and binders used in the pelletizing process at LKAB [9].

Additives	**Binders**
Lime and lime-magnesium compounds	Bentonite
Recycling materials	Slaked lime
Ores with a high bonding ability	Limestone
Quartz and quartzite	Dolomite

To reach the desired high-quality end-product, a reduction of moisture content and oxidation of magnetite to hematite, which is carried out through a heat treatment process is required [7], [10]. The heat treatment includes drying, oxidation, sintering, and cooling. The most common processes that these steps can be carried out is through a straight-grate or a grate-kiln process, where the straight-grate is mainly used for hematite and the grate-kiln process for magnetite [10]. This is because using hematite ore in the grate-kiln produces more fines which are subject to larger losses [7]. For the grate-kiln process, the kiln is represented as a cylindrical rotating furnace, where part of the sintering and oxidation takes place. As the furnace rotates, the pellets bed mixes, thus providing an even angular temperature distribution in the bed [10]. At the lower end of the kiln, a jet-like coal flame

is commonly used to supply the pellets with heat, where the key heat transfer mechanism is radiation from the flame[11]. The fuel used is mainly determined by its composition, cost, heating value and availability. Note that other heat transfer mechanisms that occur and are also of importance are, convection and conduction but heat is also released within the bed due to chemical reactions. Furthermore, heat is being transferred with the bed and wall materials in the axial and angular directions as the kiln is rotating. While LKAB uses both the straight-grate and grate-kiln process at their production sites, this master thesis work focuses on the grate-kiln process.

2.2 Grate-kiln process

In Figure 2.1, a grate-kiln process is illustrated, where the grate is divided into several zones, updraft drying, (UDD), downdraft drying, (DDD), temperate preheat, (TPH) and preheat, (PH) [10]. In these zones, the pellets undergoes drying, preheating, and oxidation, as hot gases pass through the bed of pellets. The pellets are then, as mentioned, further heated, and sintered in the rotary kiln. Afterward, the pellets undergo cooling in a rotating cooler using ambient air, C1-C4, where the air is heat exchanged with the hot pellets bed and then reused as preheated air in the grate section. Note that air from C1, is approximately 1200°C and used to combust the fuel. By using the preheated air from zones C2-C4, appropriate process temperatures in the different zones, UDD-PH are achieved, and the pellets are successively dried by evaporating the water content. The process temperatures in the zones are of importance to prevent the expansion from the evaporation of the water moisture to damage the pellets [7], [9]. The pellets bed has a height of approximately 20 cm [10], where a bed height of 23 cm should not be exceeded as the pellets at the lower bed layer could be crushed by the weight from the upper bed layers [9]. The green pellets enter the grate with a moisture content of approximately 11% and the drying begins at the UDD-zone with an air temperature at approximately 150°C, blowing upwards, through the bottom layer of the bed [10]. At the DDD-zone preheated air at approximately 400°C is blown downwards, through the upper layer of the bed to evaporate the moisture in the upper layer as well. The oxidation of magnetite to hematite, Reaction R.1 [11], mainly occurs in the TPH and PH-zone, where the TPH-zone uses preheated air around 1000°C [10]. The oxidation reaction is exothermic, releasing heat, and together with the recirculated combustion gases, which are about 1200°C, the pellets are preheated in the PH-zone, before entering the kiln. To promote the oxidation reaction, an excess air is fed to the kiln so that the O_2 concentration in the PH-zone is approximately 16% O_2 [10], [11]. The kiln is approximately 34 m in length, 5.5 in inner diameter, and rotates at 1.4 rpm, with an inclination of 4%. Inside the kiln, the bed of pellets, which corresponds to 10% of the volume of the kiln, are subject to further heating and oxidation by a coal flame with 35-40 MW_{th} [12], [10].

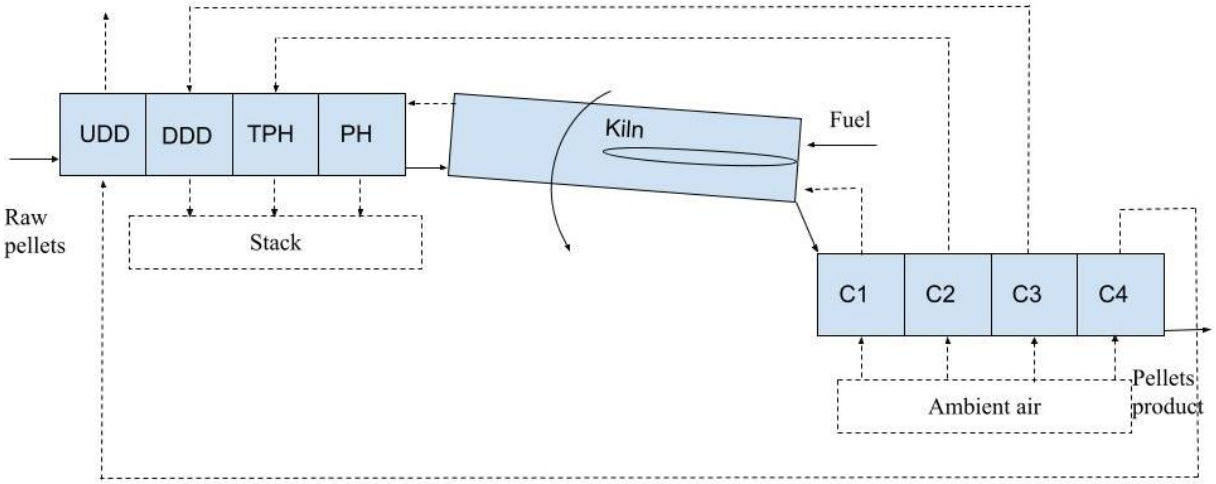

Figure 2.1: The heat treatment process in the grate-kiln system.

The oxidation reaction of magnetite to hematite, Reaction R.1 is exothermic with an enthalpy of reaction of -119 kJ/mol. The reaction reaches a maximum conversion efficiency at approximately 1100°C [7].

$$4\,Fe_3O_4 + O_2 \rightarrow 6\,Fe_2O_3 \qquad \triangle H = (-119)\ kJ/mol \ \text{[11]} \qquad \text{(R.1)}$$

2.3 Heat transfer model

The heat transfer model that is to be used within this master thesis work is developed at Chalmers for a rotating kiln with a jet-like coal and oil flame [11]. The model describes the heat transfer within the kiln and to the pellet bed material, which is heated by radiation from the flame, convection from the gas traveling through the kiln, and conduction between the bed and wall. Also, as mentioned, the pellets will continue to oxidize, see Reaction R.1, to an extent inside the kiln, thus reaction heat is generated, which is added as a source term in the bed material within the model. The model is built around the radiative heat transfer equation, RTE, since the total heat transfer in the kiln is dominated by the radiation. The RTE describes for a given wavenumber, the radiative intensity change from the summed contributions of absorption, emission, and scattering along a set direction [13]. Furthermore, as the kiln is rotating, part of the bed material, which is closest to the wall, is considered to have non-slip to the wall in the axial cross-sectional direction and follows the wall upwards with the rotation of the kiln, transporting heat with the bed material [13], [11]. Eventually, this part of the bed falls over and mixes with the bulk of the bed. Thus, the pellet bed is divided into two layers, a surface layer, and a bottom layer, which move in the opposite direction of each other. Note that the bed layer that is in contact with the wall of the kiln is subject to conductive heat transfer, while the pellets layer on top is subject to convective and radiative heat transfer [11]. It should also be noted that it is anticipated that the main contributor to the radiative heat transfer from the flame will be the result of the hot unburnt fuel particles as well as particles formed during combustion, being much larger than the gas contribution [13]. As combustion of solid fuel, coal is currently used, the hot particles include char, ash, and soot particles. Thus, when modelling the radiative heat transfer it is important to include the radiative properties of the different particles as well as the gases.

The energy flux from radiation may be described as a function of the gas temperature in accordance to Boltzmann's law, Equation 2.1 [14]. The total radiated energy over all wavelengths per surface area (W/m^2) is described as a function of the emissivity, ε, the Stefan-Boltzmann constant, σ, and the temperature of the surface, T. If a black body is assumed, the surface is assumed as a perfect absorber and emitter of radiation, where the emissivity $\varepsilon = 1$. Hence the radiated energy is proportional to the surface temperature to the power of four. The heat transfer from conduction and convection is a function of the kiln wall temperature and the gas temperature, respectively, which may be described with Fourier's law [15] and Newton's law of cooling [16], Equations 2.2 and 2.3, respectively. Equation 2.2 describes the local heat flux (W/m^2) from thermal conduction as a function of the conductivity of the material, k, and the temperature gradient, ∇T. Equation 2.3 describes the local heat flux from convection as a function of a heat transfer coefficient, h and the temperature difference, ΔT.

$$E = \varepsilon * \sigma * T^4 [14] \quad (2.1)$$

$$q = -k\nabla T [15] \quad (2.2)$$

$$q = h\Delta T \ [16] \quad (2.3)$$

In the model, a discrete-ordinates method (DOM) is used to solve the RTE, in which the cylindrical kiln volume is divided into cells in the angular, axial, and radial directions [11]. The cells holds values of temperatures, concentration, and radiative properties for gases and particles [11], [12]. The radiative properties of the present gases are calculated from a weighted sum of grey gases (WSGG) model, which accounts for the concentrations of CO_2 and H_2O. Using Planck averaging, spectral particle properties which are calculated using Mie theory for fuel and ash particles, and Rayleigh theory for soot particles, can be transformed into grey properties and used together with the gas properties from the WSGG model. Thus, by solving the RTE for all cells, which is done iteratively based on an initial guess, the achieved results yield a bed and wall temperature profile for the kiln. The initial guess, specified as input data to the heat transfer model, is a temperature profile, gas concentration, and particle concentration. A summary of the data inputs, outputs, and sub-models used in the heat transfer model, are described in, Figure 2.2.

Note that heat losses are also taken into account in the model by including heat losses from the outside surface of the kiln to the surrounding by radiative and convective transport [11].

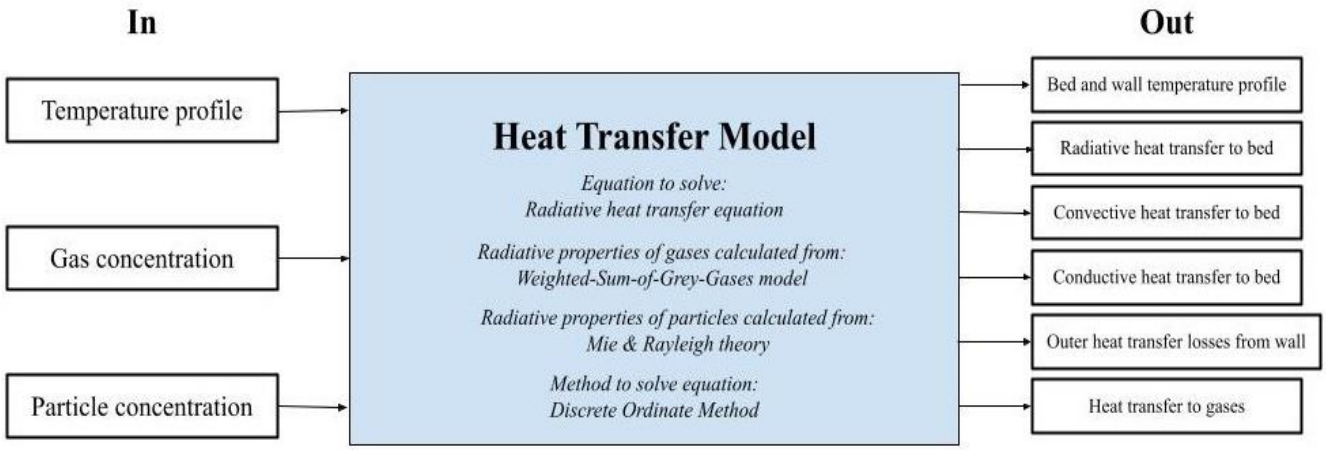

Figure 2.2: Describes the inputs, outputs, and sub-models used in the heat transfer model.

The RTE is expressed in Equation 2.4, describing the radiative intensity change from a direction $\hat{s}$ and for a wavenumber v. The absorption coefficient, κ_v is dependent on the gases and particles present [13]. The scattering of thermal radiation is defined by the scattering coefficient σ_s and is dependent on the particles present only. The term $I_v(\hat{s_i})$ describes the spectral intensity that is scattered from the direction $\hat{s_i}$ into direction $\hat{s}$ and depends on the scattering phase function, Φ_v, and the solid angle, $d\Omega_i$ [12]. These terms describe the probability of scattering from $\hat{s_i}$ into the $\hat{s}$ direction and the solid angle of the ray in the $\hat{s_i}$ direction, respectively [13].

$$\frac{dI_v}{ds} = \kappa_v I_{bv} - \kappa_v I_v - \sigma_{sv} I_v + \frac{\sigma_{sv}}{4\pi}\int_0^{4\pi} I_v(\hat{s_i})\Phi_v(\hat{s_i},\hat{s})d\Omega_i \quad (2.4)$$

As mentioned, the scattering coefficient is not included for gases, thus the radiation intensity change of the gases is simplified to Equation 2.5 [13]. Note that the absorption coefficient, κ is in Equation 2.5, a function of the wavenumber, v. Hence radiative properties of the gases are required for each wavenumber in the heat transfer model. However, such calculations would be too demanding for the model and the properties are obtained by using a simplified model, called a weighted-sum-of-grey-gases (WSGG) model according to Equation 2.6 [13].

$$\frac{dI_v}{ds} = \kappa_v I_{bv} - \kappa_v I_v = \kappa_v (I_{bv} - I_v)[13] \quad (2.5)$$

$$\kappa_j = K1_j + K2_j \frac{Y_{H2O}}{Y_{CO2}}[13] \quad (2.6)$$

The WSGG model describes the absorption coefficient for a grey gas, j, as a function of the gas concentrations of H_2O and CO_2. Note that the coefficients $K1$ and $K2$ are specific coefficients related to a grey gas. By using several such grey gases, the model aims to describe all spectral regions, using an absorption coefficient in a specific range, and each grey gas is weighted. The grey gases selected are dependent on the desired range of temperature, molar ratios, and pressure path lengths. The WSGG used in this master thesis work is adapted for hydrocarbon flames, i.e., coal and oil flames.

Rayleigh theory was applied to describe the particle radiation of soot particles, according to Equation 2.7, and Mie theory was used to simulate the particle radiation of fuel and ash particles, according to Equation 2.8 [13]. Rayleigh theory describes the absorption coefficient as a function of the particle volume fraction, f_v, at a given wavelength, λ, and a function of the complex refractive index $E(m_\lambda)$. The complex refractive index, in accordance to Equation 2.9, describes the optical properties related to a specific type of particle. Mie theory are complex but describes the absorption and scattering coefficients as a function of the efficiency factors Q_{abs}, Q_{sca}, and the projected surface areas of the particles, A_{proj}. The efficiency factors are also dependent on the complex refractive index.

$$\kappa_\lambda = E(m_\lambda)\frac{6\pi f_v}{\lambda} \quad (2.7)$$

$$\kappa = Q_{abs}A_{proj}$$
$$\sigma_s = Q_{sca}A_{proj} \quad (2.8)$$

$$m_\lambda = n_\lambda - ik_\lambda \quad (2.9)$$

The spectral particle properties, defined as the summed absorption coefficients from soot, coal and ash, as well as the summed scattering coefficients from coal and ash, are, transformed into grey gas particle properties using Planck averaging, Equation 2.10. With the grey particle properties and gas properties from the WSGG model, the RTE is ultimately solved.

$$\kappa_{gray,particles} = \frac{1}{I_b}\sum \Delta v\, I_v \kappa_v$$
$$\sigma_{s\,gray,particles} = \frac{1}{I_b}\sum \Delta v\, I_v \sigma_s \tag{2.10}$$

In summary, in the grate-kiln process, the majority of the heat transfer lies in the radiation from the coal flame. Therefore, replacing this flame with that of a hydrogen gas flame is complex since the hydrogen gas flame does not contribute to the same radiatiative properties since it is lacking radiating particles and CO_2. Thus, implementing a hydrogen gas flame will most likely change how the kiln should be operated.

Figures 2.3a and 2.3b illustrate the heat transfer mechanisms in a kiln in both vertical and horizontal positions, which the heat transfer model includes.

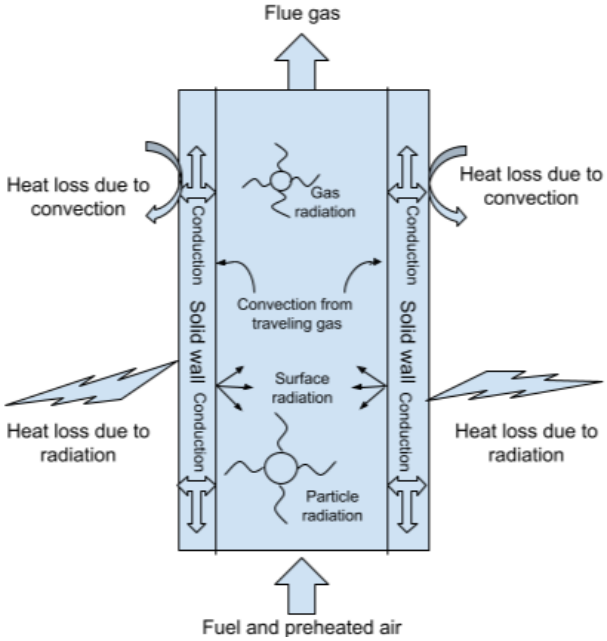

Figure 2.3a: Example of the heat transfer mechanisms in a kiln without the pellets bed or flame profile.

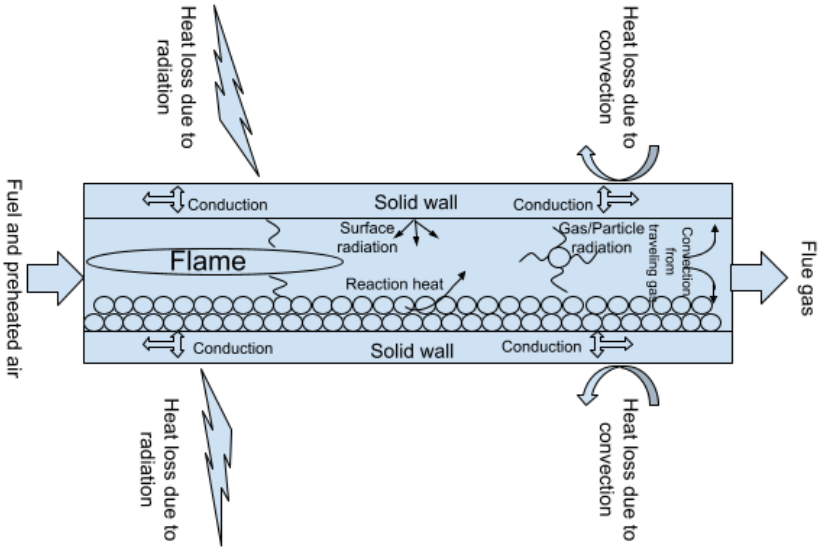

Figure 2.3b: Example of the heat transfer mechanisms in a kiln in horizontal position with a simplified pellets bed and flame profile included.

The figures represent the heat transfers in the kiln which is included in the model. A detailed summary of the heat that is transported by radiation, convection, and conduction in the kiln, is listed in, Table 2.2.

Table 2.2: Describes a summary of the heat transfers from radiation, convection, and conduction.

Heat Transported by Radiation between:	**Heat Transported by Convection between:**	**Heat Transported by Conduction:**
Flame and bed material	Gas inside the kiln and bed material	Between bed material and kiln wall
Flame and kiln wall		
Bed material and kiln wall *(Both above and underneath the bed material)*	Gas inside the kiln and kiln wall	
Kiln wall and kiln wall		Within bed material and kiln wall
The outer surface of the kiln wall and surroundings	The outer surface of the kiln wall and surroundings	

2.4 Implementing combustion of hydrogen gas

The production of hydrogen gas originates from several processes and can be considered a renewable fuel if produced from water electrolysis or biomass gasification powered by wind, water, or solar power [17]. The overall combustion of hydrogen gas, (H_2), is described in Reaction R.2 [18]. Note that the combustion of H_2 should not generate particle emissions if not the combustion air is contaminated with a small number of particles [17]. In addition, as can be concluded from Reaction R.2, the significant radiating species that should be considered is the excited state of the water vapor molecule, H_2O [17], [19]. The lack of char, ash and soot particles as well as carbon dioxide in the hydrogen flame, compared to the fossil coal flame, results in a flame with less radiative heat transfer characteristics, hence can store more energy in the flue gas rather than radiate that energy to the surroundings [17]. This may cause complications in the kiln as the combustion of hydrogen reaches higher flame temperatures, influencing the heat transfer to the pellet bed. Furthermore, this may increase fuel consumption and reduce thermal efficiency [20].

$$H_2 + \frac{1}{2}O_2 \rightarrow H_2O \quad \text{(R.2)}$$
$$\Delta H = -241.81 \frac{kJ}{mol\ H_2} \text{ [18]}$$

In this master thesis work, the focus has been to analyze and influence the radiative heat transfer to the bed material by a hydrogen flame. However, all complications when the flame temperature increases within the kiln are not discussed in detail. One such complication that one should be aware of arises when the flame temperature reaches approximately 1300°C, promoting the thermal formation of NO_x emissions by the oxidation of nitrogen in the air, according to the Zeldovich mechanisms, Reactions R.3a, R.3b, R.3c [21]. These reactions are sensitive to high temperatures due to the activation energy of Reaction R.3a, being 320 kJ/mol. As the local concentration of oxygen in the flame increase with increasing temperature, this will promote NO_x formation as shown in Reaction R.3a. Such NO_x emissions must be taken care of in the flue gas as they are harmful for the environment. However, as the complications due to increased NO_x emissions is not the focus of this master thesis work, the topic is not further discussed. In summary, one should, however, be aware of such complications that may arise when combusting hydrogen gas in a rotary kiln.

Zeldovich mechanisms [21]:

$$O + N_2 \leftrightarrow NO + N \quad \text{(R.3a)}$$
$$N + O_2 \leftrightarrow NO + O \quad \text{(R.3b)}$$
$$N + OH \leftrightarrow NO + H \quad \text{(R.3c)}$$

In the rotary kiln, the aim is to achieve a flame that extends far into the kiln and supplies an even heat load to the bed material, as it is considered beneficial for the heat treatment process of the pellets [22]. Furthermore, the heat transfer rate in the kiln will affect the quality of the pellets [22], [23]. Since a too fast heat transfer will only oxidize the outer shell of the pellet, but not the core, which is undesired for the quality of the pellets product [23]**.** It has also been concluded from previous research for coal combustion in cylindrical furnaces, that coal and char particles were the main contributors to the heat flux at the wall. Furthermore, the information regarding the temperature and particle concentration distributions, was found more important when studying flames, than the gas concentration in order to predict the heat transfer from radiation [13]. Particles and gases in the current coal flame will absorb, emit and scatter radiation from the surrounding, thereby affecting the heat transfer from radiation and extending the heat load to the pellet bed. Note that the particles are larger than the gases and characterized as broad-band emitters, as they absorb, emit, but also scatter radiation continuously across the spectrum.

By exchanging the coal for hydrogen combustion, a shorter flame length is expected due to the physical properties of hydrogen, such as the low molecular weight and rapid radial molecular diffusion, which causes an increase in flame width, thus, controversially decreasing the flame length proportionally. Additionally, the increase in radicals from combustion, such as H and OH, enhances the combustion rate, thereby reducing the flame length [24]. This expectation is further strengthened by experimental experiences from a measurement campaign conducted in a pilot scale rotary kiln. The combustion of natural gas and several coal fuels resulted in a shorter flame length and higher flame temperatures for the gas flame, likely above 2000°C, compared to combusting pulverized coal (1500-1600°C) [22]. The results concluded that the shorter flames with higher local flame temperatures may cause complications with an uneven heat transfer load to the pellet bed. A shorter flame length affects the length of the highly radiating part of the flame, which influences the length where the emittance of thermal radiation dominates, in comparison to other heat transfer mechanisms. Note, that compared to coal, combusting natural gas does not include radiation from char or ash particles. Thus, with a lesser contribution from particle radiation and shorter flame length, the heat transfer to the pellet bed will be influenced. In summary, using hydrogen gas as fuel may complicate the heat transfer load to the pellet bed and consequently the quality of the pellets. Furthermore, as flue gas temperatures are expected to increase, the heat losses will increase as well.

Figures 2.4a and 2.4b present a hypothesis of the expected temperature of the flue gas exiting the kiln and the heat transfer load to the pellet bed, respectively, along the axis of the kiln. The figures are based on the description above, and as is illustrated in Figure 2.4a the expected overall flue gas temperature inside the kiln is higher for a hydrogen and natural gas flame, than for a coal flame, which is due to less effective heat transfer conditions. In Figure 2.4b, the expected peak heat transfer to the pellet bed is higher for both hydrogen and natural gas in comparison to coal. Figure 2.4b further shows the rate at which the heat transfer to the pellet bed is expected to decrease and how the desired heat transfer load to the bed material is not achieved throughout the length of the kiln, when combusting hydrogen or natural gas.

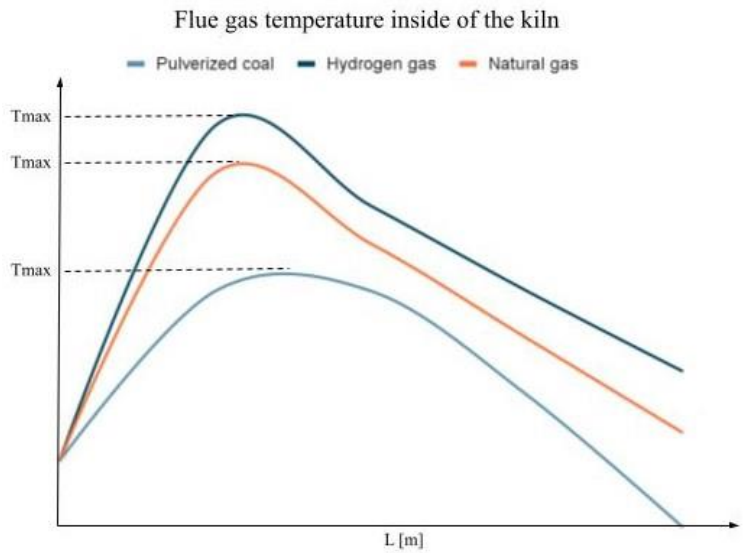

Figure 2.4a: An example of what the predicted flue gas temperature along the furnace axis on the inside the kiln may look like, using pulverized coal, hydrogen gas, or natural gas, as combustion fuel. In the figure, the burner is located to the left and the bed material would enter from the right.

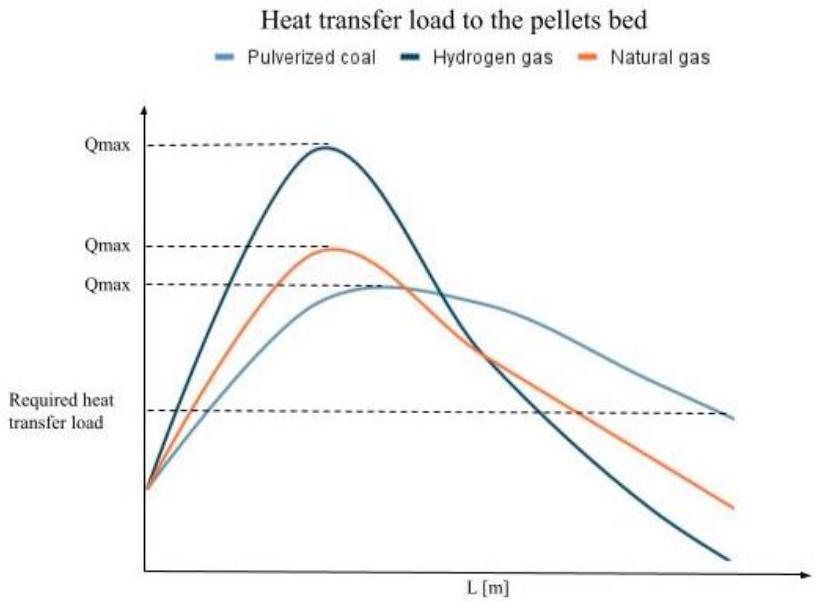

Figure 2.4b: An example of what the predicted heat transfer load to the pellet bed along the furnace axis on the inside the kiln may look like, using pulverized coal, hydrogen gas, or natural gas, as combustion fuel. Note that there is a required level of heat transfer load needed to achieve a certain amount of quality and that in the figure, the burner is located to the left and the bed material would enter from the right.

In summary, it is likely that using hydrogen gas as fuel, compared to natural gas and pulverized coal, increases the local flame temperatures. In addition, because of its radiative properties, less heat radiates to the surroundings, resulting in a higher flue gas temperature leaving the kiln, as illustrated in Figure 2.4a. Furthermore, regarding the heat transfer load to the pellet bed, using hydrogen gas as fuel may result in an undesired heat load to the pellet bed, as seen in Figure 2.4b. Thereby, possibly affecting the quality of the pellets.

3.

Methodology

An important part of this master thesis work has been to further develop the previous modeling work carried out at the division of Energy Technology at Chalmers in collaboration with LKAB. This is to increase the understanding of the heat transfer in the rotary kiln for different combustion fuels and how the process could be operated to combust hydrogen gas and receive a product with the desired properties. By applying theory of the heat transfer mechanisms and flame profile of hydrogen gas flames from similar processes to the existing model, a hydrogen flame was implemented. The heat transfer conditions of the flames from hydrogen and other fuels, were then further studied by, conducting sensitivity analyses of several design parameters. The working procedure in this master thesis work has been to calculate the theoretical maximum flame temperatures from combusting the fuels, hydrogen, coal, and oil, with regard to the airflow in the kiln, predict the flame temperatures inside the kiln by a simple air mixing function, and examine the effects of several design parameters and how this influences the heat transfer from the flame to the bed material inside the kiln.

3.1 Model

This section describes the reference settings specified with the heat transfer model. Furthermore, this section includes, which parameters were kept constant, calculated, and studied in the sensitivity analyses for the fuels, hydrogen gas, coal, and oil. Note that the radiative properties calculated for the gases using a weighted sum of grey gases model, is in the heat transfer model adapted for hydrocarbon flames, such as coal or oil flames. Since the flame temperatures are expected to increase with a hydrogen flame, the already implemented model was extrapolated for all cases studied in this master thesis work.

3.1.1 Reference settings

To simulate a case, the heat transfer model requires some parameters to be specified as constant as listed in Table 3.1. The table describes the bed temperature of the pellets entering the kiln from the PH-zone and the thermal power of the fuel fed to the kiln, as well as the gas temperature from the cooler (C1), and to the PH-zone. The values listed in Table 3.1 are taken as process data of a full scale kiln at LKAB. As mentioned in Section 2.2, the preheated air from the cooler is approximately 1200°C, and the flue gases fed to the PH-zone are around 1200°C. As mentioned in Section 2.4, the energy from the flue gases of combusting hydrogen is likely higher than of combusting coal. Thus, the gas temperature to the PH-zone was set to 1300°C. Furthermore, in order to compare the cases with different fuels, 1300°C to the PH-zone was used as the reference setting for all the types of fuels studied in this master thesis work.

Table 3.1: The constant parameters used as the reference settings used with the heat transfer modeling tool. The data is based on process data from a full scale kiln at LKAB.

Constant Parameter:	Value:	Unit:
Bed temperature to kiln	1000	°C
Gas temperature from cooler	1200	°C
Gas temperature to PH	1300	°C
Thermal power from fuel	35	MW

The heat sources and heat sinks are described in Figure 3.1, including the parameters from Table 3.1. The calculated parameters from the heat transfer modeling tool are listed as heat sinks in the kiln, see Figure 3.1. The total amount of energy needed to heat the preheated air fed to the kiln, to that of the combustion gases exiting the kiln, is listed as, total heat to gas. The outer heat losses are quantified as the heat loss from the outer walls of the kiln to the surroundings. The pellets bed fed to the kiln is dependent on the bed temperature entering the kiln and the degree of oxidation of the pellets. As mentioned in Section 2.3, the reaction energy from the oxidation of magnetite to hematite, Reaction R.1 is exothermic and added as a source term assumed as 9 MW. Furthermore, all heat sources listed in Figure 3.1 are kept constant for all cases. The bed temperature exiting the kiln is dependent on the energy transferred to the bed material and is quantified as the sum of the heat transfer from, radiation, convection, and conduction to the bed material.

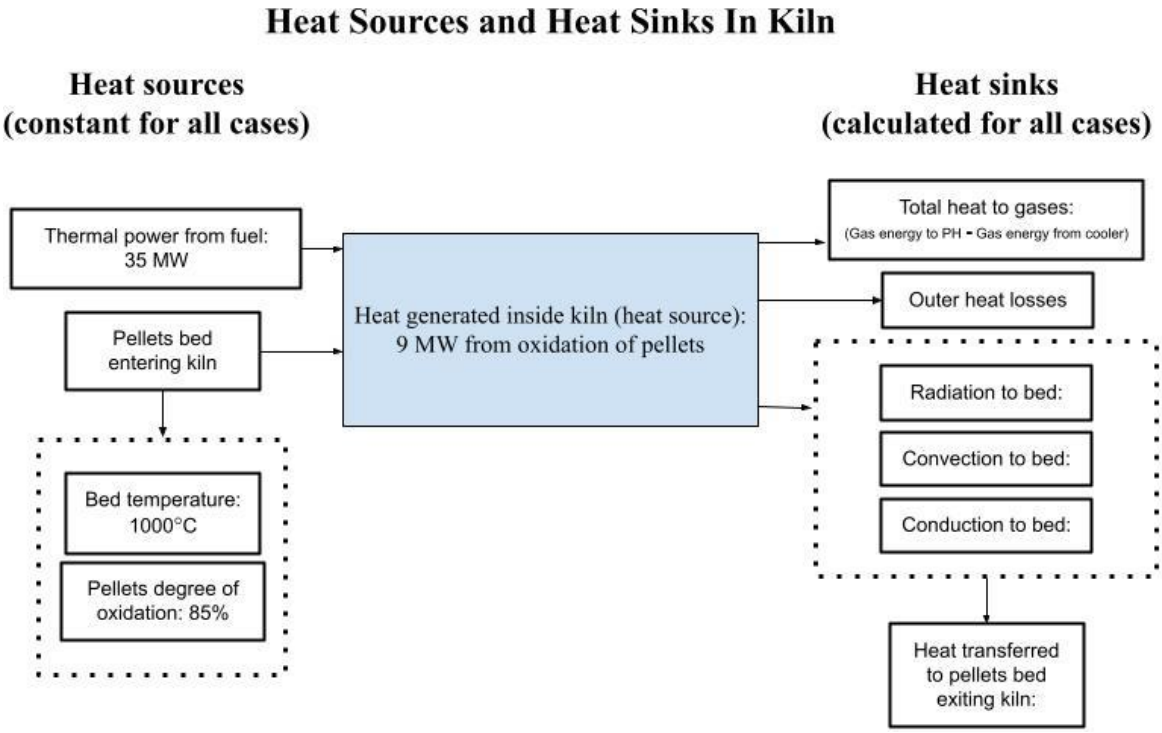

Figure 3.1: Heat sources and heat sinks in the kiln; the heat sources are constant for all cases studied. The heat sinks are calculated for all cases.

The heat transfer model assumes an energy balance over the flame to the bed material, where the supplied thermal power from the fuel shall be equal to the calculated heat sinks. The energy balance is illustrated in Figure 3.2. In summary, the energy balance is satisfied when the energy supplied through combustion, equals to the sum of the transferred heat in the kiln, i.e., 35 MW.

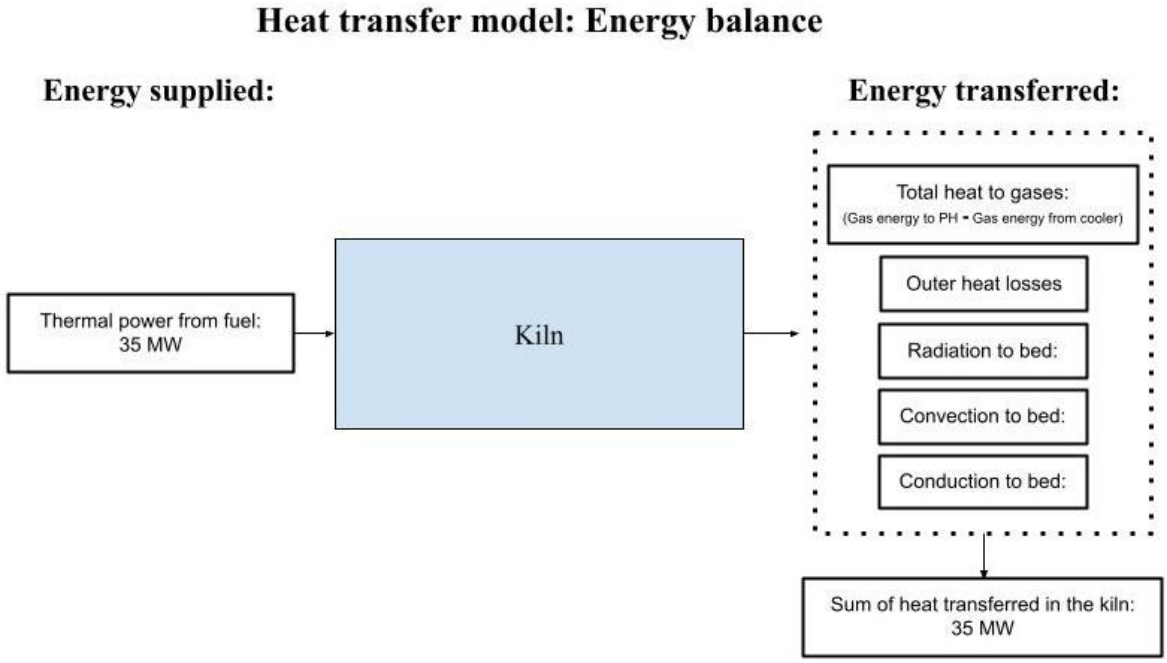

Figure 3.2: Energy balance solved with the heat transfer model.

The heat transfer model calculates the possible heat that can be transferred from the flame to the bed, which may exceed or be less than the supplied thermal power. Thus, the constant parameter, the gas temperature to the PH-zone, has to be specified such that the energy balance is solved. In summary, the gas temperature to the PH-zone may differ from the reference settings in each case. Alternatively, other parameters may be examined such as temperature, particle radiation, flame composition, and flame dimensions. These were further studied in sensitivity analyses for different cases and are described in Section 3.1.2.

3.1.2 Sensitivity analysis

The idea of conducting sensitivity analyses is to show that it is possible to obtain a similar bed temperature exiting the kiln with a hydrogen flame as with an coal or oil flame. Matrix M.1 describes the constant parameters studied, how they were studied, and the effect of influencing that parameter. Matrix M.2 describes the constant parameters studied for the corresponding fuel type examined.

Constant parameter studied	Studied by	Calculated parameter influenced
Temperature:	• Increasing the overall gas temperatures in kiln • Increasing gas temperature from cooler • Increasing gas temperatures to PH • Adding dissociation reaction	↓ Total heat to gas ↓ Convection to bed + Radiation to bed ↓ Conduction to bed + Outer heat losses ↓ Sum of heat + Bed temperature out
Particle radiation:	• Adding coal particles in the flame • Adding iron ore dust particles in the flame	Calculated parameter influenced ↓ Radiation to bed ↓ Conduction to bed ↓ Sum of heat + Bed temperature out
Flame composition:	• Adding hydrogen gas	Calculated parameter influenced ↓ Radiation to bed + Total heat to gas ↓ Conduction to bed + Convection to bed ↓ Sum of heat + Bed temperature out
Dimensions:	• Increasing flame length	Calculated parameter influenced ↓ Radiation + convection to bed ↓ Conduction to bed ↓ Sum of heat + Bed temperature out

Matrix M.1: Constant parameters examined and how the parameters were studied. The matrix also shows the calculated parameters influenced and a simplified cascade effect by affecting that parameter

Case: Hydrogen flame	
Constant parameter studied	**Studied by**
Temperature:	• Increasing the overall gas temperature in kiln • Increasing gas temperature from cooler • Increasing gas temperatures to PH • Adding dissociation reaction (R.4)
Particle radiation	• Adding coal particles in the flame • Adding iron ore dust particles in the flame
Dimensions:	• Increasing and decreasing flame length
Case: Coal flame	
Constant parameter studied	**Studied by**
Temperature:	• Decreasing gas temperatures to PH • Adding dissociation reaction
Dimensions:	• Increasing flame length • Increasing flame width
Flame composition:	• Adding hydrogen gas
Case: Oil flame	
Constant parameter studied	**Studied by**
Temperature:	• Increasing gas temperatures to PH • Adding dissociation reaction
Dimensions:	• Increasing flame length

Matrix M.2: The constant parameters studied for the different fuels, hydrogen, coal and oil.

To study the effect of increasing the temperature, four parameters were studied as described in the matrixes, M.1 and M.2. Increasing the overall gas temperature in the kiln, meaning that the temperatures used as input data for all cells increased, i.e. the gas temperature from the cooler, gas temperature to the PH-zone, and the flame temperatures increased. This was executed by multiplying the temperature in each cell with a certain factor. Alternatively, the effect of increasing the gas temperature from the cooler, or to the PH-zone, may be studied by altering the specification from the reference settings. Lastly, the effect of dissociation was examined for each fuel by including a dissociation reaction to the combustion reaction, which is presented in detail in Section 3.2. By including the dissociation reactions, less H_2O is produced in the hydrogen combustion, and less CO_2 is produced from combusting coal or oil. The idea of examining the various temperatures is to study the gas energies in the kiln and how this affects the calculated parameter, total heat to gas, and the radiation from H_2O, which also affects the energy balance, as shown in the cascade in Matrix M.1.

In order to examine the contribution of particle radiation to a hydrogen flame, particles were included in the model. The particle radiation was implemented by introducing coal or iron ore dust particles into the flame. To study different concentrations of particles, three hydrogen flame lengths, described in Section 3.4, were included in the study. The particles were implemented by including a representative particle diameter, defined as a maximum projected surface area of coal particles, which is used to calculate the absorption and scattering of radiation in accordance to Mie theory, Equation 2.8. The maximum projected surface area of coal particles is gathered from [25], where the area is calculated from a size distribution based on particle measurements in the center of a coal flame in a pilot scale furnace. The particle size distribution is assumed to follow a cosine profile with a peak value, the maximum projected surface area, at the centerline of the kiln. Since the model uses this variable for the current coal and oil flame, a certain factor of the maximum projected surface area could be added to the hydrogen flame. This resulted in sensitivity analyses for different factors of particles, affecting the particle concentration, used as a data input to the heat transfer model. Increasing the flame length or cell resolution adds more particles since this allows more cells to store values of particle concentration. Thus, it was also of interest to study the flame lengths of the respective coal and oil flames. Note that the factor of the maximum projected surface area is listed in the results as a factor of particles added into the flame, which corresponds to the studied flame length.

One type of particle that could be considered to be added to the flame is iron ore dust since it is a residual product from the heat treatment of the pellets available at the production site. To examine the effects of the optical properties of particles, iron ore dust, (IOD) particles, were implemented in the model. The following assumptions were made to predict the radiative contribution from iron ore dust particles. The maximum projected surface area was assumed the same as coal particles. As, the particles may contain 97% hematite, [17], the IOD was assumed in the model as 100% hematite. The particles were assumed to be spherical with a particle diameter of 40 microns [17]. Mie theory was used to calculate the radiative particle properties for the IOD, with the optical properties examined and gathered from, [26], [27], [28], [29]. It should be noted that data taken from, [26] may overpredict the optical properties of hematite according to [29]. The data taken from [27] is the optical properties of magnetite and the data taken from [28] is that of ash containing 5.47% hematite. The data taken from [29] is a summary of simulated values from several sources.

As an alternative to adding particles to the hydrogen flame, the effects of adding hydrogen gas to the coal flame was examined as well. A sensitivity analysis was conducted by adding a factor of thermal power from hydrogen while decreasing the same power from coal, keeping the power from the fuel constant at 35 MW. However, this also caused decreasing the maximum projected surface area of coal particles with the same factor. The resulting factors of thermal power from hydrogen used in this master thesis work, were 10%, 15%, and 20%, which is based on discussions with LKAB. The idea is to study the effects of influencing the flame temperature in the coal flame, in consequence of decreasing the particle concentration. Furthermore, the combustion of additional hydrogen produces more water vapor and the reduction of thermal power from coal reduces the amount of carbon, which produces less carbon dioxide. Thus, the data input of the gas concentration to the heat transfer model is affected by the addition of hydrogen.

3.2 Adiabatic flame temperature profile

3.2.1 Hydrogen flame profile

For the prediction of the hydrogen flame temperatures at various airflows in the kiln, the adiabatic flame temperatures from hydrogen combustion at various excess of air were calculated. This resulted in a flame temperature profile as a function of the excess air ratio. The inputs, outputs, assumptions, and calculations of the flame temperature profile are described in Figure 3.3, which includes the combustion reaction of hydrogen, Reaction R.2. Furthermore, the profile assumes a constant thermal power of fuel, a gas temperature from the cooler, and an airflow from the cooler. As mentioned in Section 2.3, the specified airflow is due to the excess O_2 concentration in the flue gas (~17%), which is required to oxidize the magnetite to hematite, Reaction R.1. The purpose of the profile is to yield an adiabatic flame temperature profile as a function of the excess air ratio, the H_2O composition as a function of the excess air ratio, and the amount of dissociated H_2O if dissociation is assumed. The equations used to calculate the adiabatic flame temperature are described in detail in Appendix A. The figures and tables for the case with respect to dissociation are listed in Appendix B.

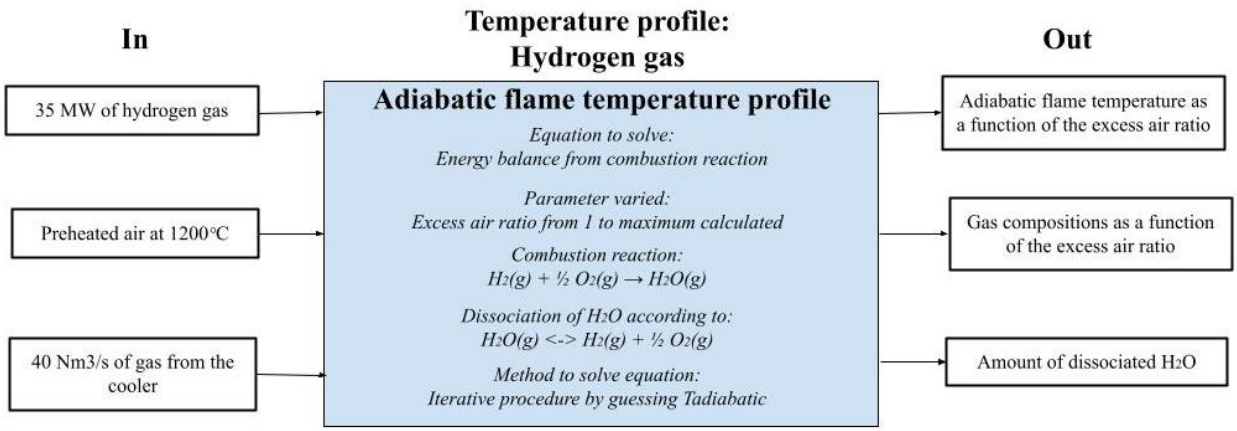

Figure 3.3: Describes the inputs and outputs from the constructed adiabatic flame tempertature function for combusting hydrogen gas.

Figure 3.4 illustrates the calculated dissociated amount of H_2O based on the equilibrium reaction Equation 3.4. From Figure 3.4 it may be concluded that the dissociation of H_2O may be assumed neglected at a temperature below approximately 2200K since the dissociated amount of H_2O then has an insignificant effect on the flame temperature.

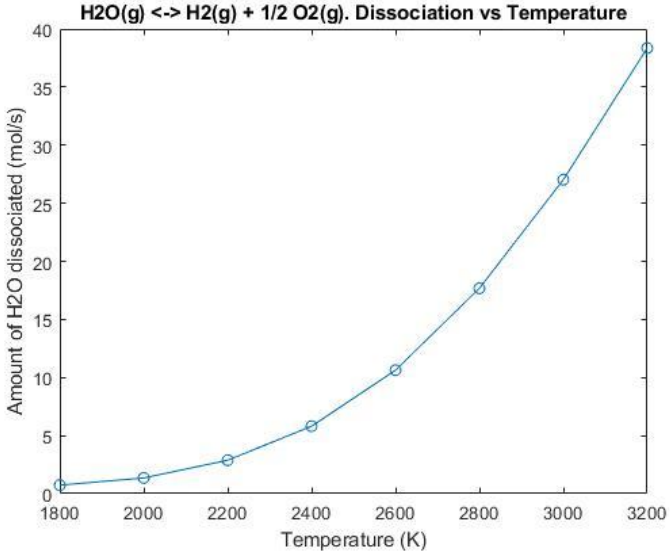

Figure 3.4: Amount of dissociated H_2O as a function of temperature based on the equilibrium reaction R.4.

The energy balance, Equation 3.1, which is to be solved, describes the sum of the energy for each component in the combustion reaction, Reaction R.2. The energy was calculated using the heat of formation at 298K, with respect to stoichiometry, and the specific heat capacity with respect to the change in temperature. The specific heat capacity for component, j is described according to Equation 3.2, where values for a and b are related to component, j and gathered from [30].

$$\sum n_j \left(\Delta Hf_{j,298K}\right) + \int_{Tref}^{T} Cp_j \, dT = \sum n_i \left(\Delta Hf_{i,298K}\right) + \int_{Tref}^{Tadiabatic} Cp_i \, dT \quad (3.1)$$

$$Cp_j = a_j + b_j * T \quad (3.2)$$

The adiabatic temperature was calculated ranging from, the minimum required airflow for the reaction to occur, corresponding to an excess air ratio value of 1, to the maximum available airflow, 40 Nm^3/s which, corresponds to λ_{max}, Equation 3.3. The minimum airflow was calculated from the minimum molar flow rate of oxygen, which is dependent on the molar flow rate of fuel, i.e., hydrogen.

$$\lambda_{max} = \frac{n_{O2,max}*2}{n_{H2}} \quad (3.3)$$

Note that the adiabatic flame temperature was calculated using an iterative procedure by guessing a range of, $T_{adiabatic}$ until both the energy from the reactants and products are equal, thus satisfying the energy balance, Equation 3.1. Furthermore, the stoichiometric coefficients from Reaction R.2, were included, ½ and 1, respectively. In order to include the dissociation of the water vapor, Reaction R.4 was introduced with an equilibrium constant according to Equation 3.4 [30].

$$H_2O(g) \leftrightarrow H_2(g) + \frac{1}{2}O_2(g) \text{ [30]} \quad (R.4)$$

$$Kp = 855 * e^{-29840/T_{adiabatic}} \text{ [30]} \quad (3.4)$$

The results from the calculations yielded the following adiabatic flame temperature profile, Figure 3.5, which represents the flame temperature without respect for dissociation. Table 3.2 is the tabular results from Figure 3.5.

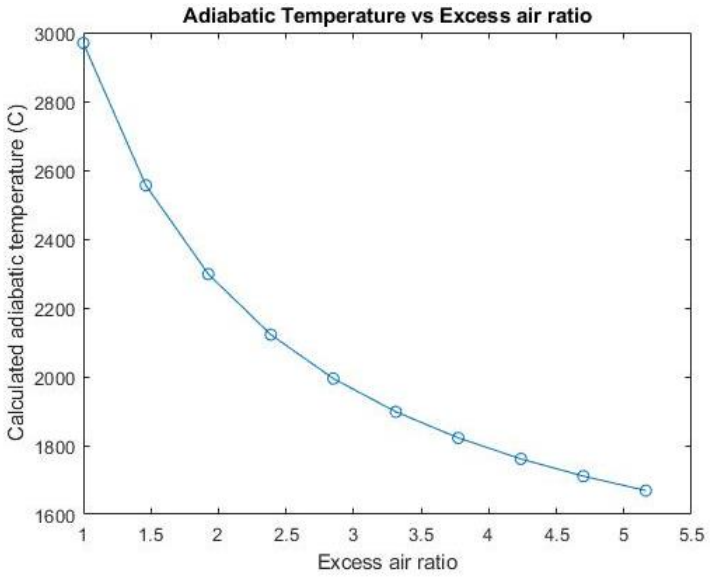

Figure 3.5: The adiabatic flame temperature of hydrogen combustion as a function of the excess air ratio without respect to the dissociation of water vapor.

Table 3.2: The calculated adiabatic flame temperatures of hydrogen, the H_2O composition in the product gases, without respect to dissociation.

Excess air ratio	Adiabatic flame temperature (°C)	H_2O composition (vol%)
1.00	2969	34.7
1.50	2556	25.1
1.90	2298	19.7
2.40	2122	16.2
2.90	1995	13.7
3.30	1898	11.9
3.80	1822	10.5
4.20	1761	9.40
4.70	1711	8.60
5.20	1669	7.80

3.2.2 Coal and Oil flame profile

As mentioned in Section 3.2, the fuels coal and oil were also studied using the reference settings. In order to calculate the adiabatic flame temperatures, the following assumptions and calculations were made in accordance to Figure 3.6. The calculations assumed complete combustion hence the combustion reactions listed in, Figure 3.6. A gas temperature from the cooler of 1200°C and an airflow of 40 Nm^3/s, which corresponds to a O_2 concentration of ~17% exiting the kiln, were further assumed. Furthermore, since the calculated adiabatic flame temperatures resulted in less than 2200K, the dissociation of water vapor was assumed, negligible, see Figure 3.4. Thus, the dissociation of CO_2, according to Reaction, R.5, and the equilibrium equation according to Equation 3.5, are included in the calculations instead of the dissociation of H_2O [30]. Note that the equations used to calculate the adiabatic flame temperature of coal and oil are described in detail in Appendix A. Furthermore, the figures of the adiabatic flame temperatures for the cases with respect to dissociation are listed in Appendix B.

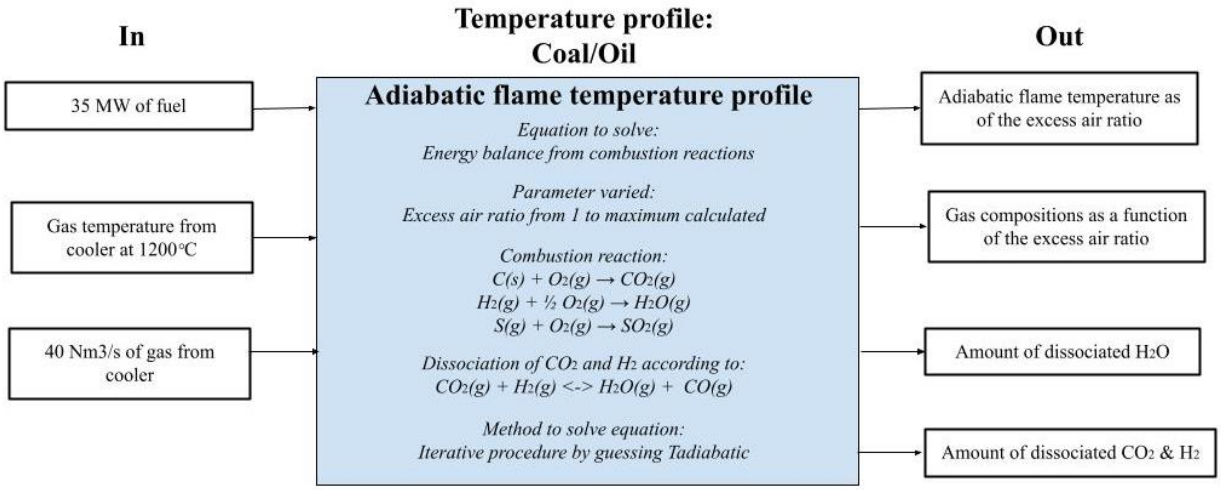

Figure 3.6: Describes the inputs, outputs and assumptions from the constructed adiabatic flame temperature function for combusting coal and oil.

$CO_2 + H_2 \leftrightarrow CO + H_2O$ [30] (R.5)

$Kp = 33.7 * e^{-\frac{-4094}{T_{adiabatic}}}$ [30] (3.5)

The adiabatic flame temperature curves as a function of the excess air ratio were calculated for the fuels, coal, and oil, similar to how the adiabatic flame temperature function for hydrogen was calculated. Note that the excess air ratio was calculated according to Equation 3.6, where n_{fuel} corresponds to the molar flow rate of fuel, which is calculated from the thermal power of the fuel, heating value and the fuel composition. For a detailed description see Appendix A. The composition of the coal and oil are listed in Table 3.3, where the coal is taken from process data at LKAB as a carbon-rich coal [31]. The oil is assumed as fuel oil and gathered from [17], where the heating value is taken from [31]. Note that the sum of the components from the oil is ~107%, which is due to an overestimated ash content. This was, however, disregarded since the ash composition has a small effect on the adiabatic flame temperature. Furthermore, the coal was assumed with a temperature of 25°C, and the oil was assumed with a storage temperature of 55°C [32].

$\lambda_{max} = \frac{n_{O2,max}}{n_{fuel}}$ (3.6)

Table 3.3: Composition of the coal and oil fuel used in this master thesis work.

Component	**Coal [31]**	**Oil [17]**
Moist (%):	0.90	0.10
Ash (%):	13.2	7.32
C (%)	75.4	87.0
H (%)	3.90	12.0
N (%)	1.40	0.31
O (%)	5.10	-
S (%)	0.30	0.39
Sum (%):	100	107
Lower heating value (MW/kg):	29.4	41.5 [31]

The calculations yielded the adiabatic flame temperature curve as a function of the excess air ratio for coal and oil, Figure 3.7, with the respective tabular data, Table 3.4 and Figure 3.8, with the respective tabular data, Table 3.5. Note that Table 3.4 and Table 3.5 also describe the H_2O and CO_2 composition for the respective excess air ratio.

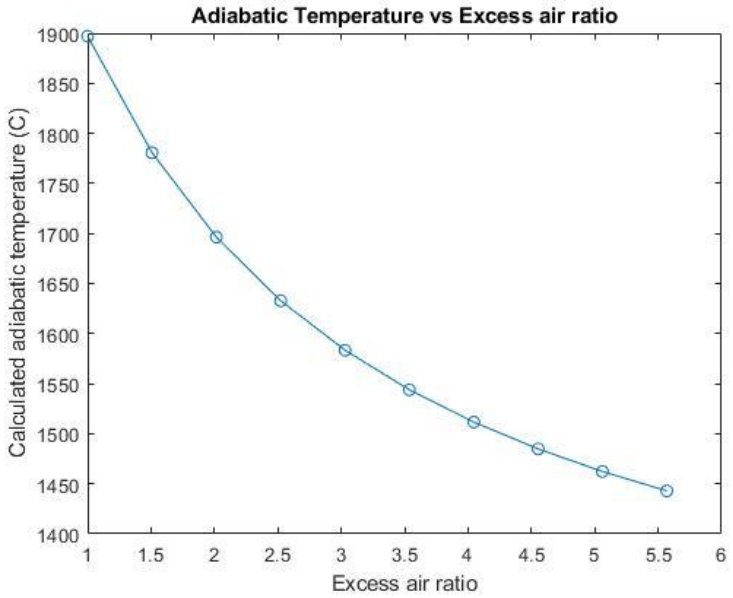

Figure 3.7: The adiabatic flame temperature of coal, without the respect of dissociation, as a function of the excess air ratio.

Table 3.4: The calculated adiabatic flame temperatures of coal, the H_2O and CO_2 composition in the product gases.

Excess air ratio	**Adiabatic flame temperature (°C)**	**H_2O composition (vol%)**	**CO_2 composition (vol%)**
1.00	1897	3.20	19.3
1.50	1781	2.10	12.9
2.00	1696	1.60	9.70
2.50	1633	1.30	7.70
3.00	1583	1.00	6.50
3.50	1544	0.90	5.50
4.00	1512	0.80	4.80
4.60	1485	0.70	4.30
5.10	1462	0.60	3.90
5.60	1443	0.60	3.50

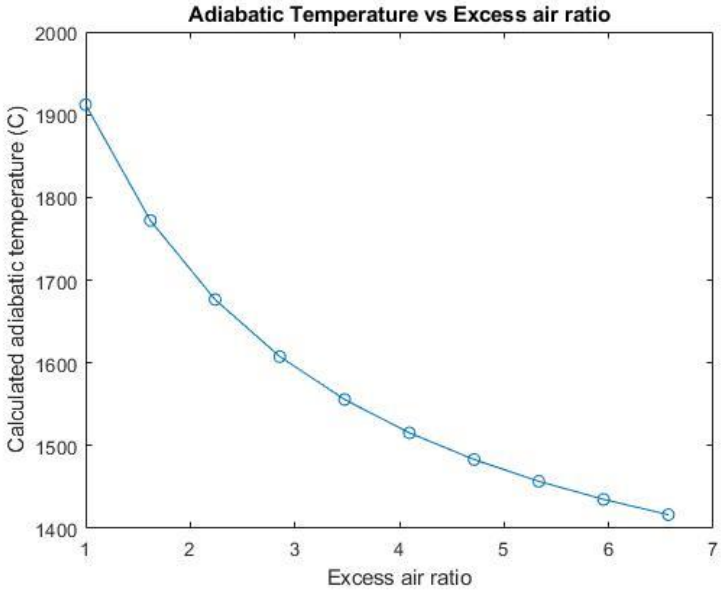

Figure 3.8: The adiabatic flame temperature of oil, without the respect of dissociation, as a function of the excess air ratio.

Table 3.5: The calculated adiabatic flame temperatures of oil, the H_2O and CO_2 composition in the product gases.

Excess air ratio	**Adiabatic flame temperature (°C)**	**H_2O composition (vol%)**	**CO_2 composition (vol%)**
1.00	1912	7.0	16.8
1.60	1772	4.40	10.5
2.20	1677	3.20	7.60
2.90	1608	2.50	6.00
3.50	1556	2.10	5.00
4.10	1515	1.70	4.20
4.70	1483	1.50	3.70
5.30	1457	1.30	3.20
6.00	1435	1.20	2.90
6.60	1417	1.10	2.60

3.3 Flame-air mixing function

To facilitate the initial temperature profile required as a data input in the heat transfer model, a generalized flame-air mixing function was constructed. The function assumes the flame as a geometrical cone inside the kiln with a specified flame length, see Figure 3.9. The flame cone is further divided into cells in the radial and axial direction within the DOM, which is adjusted to how the kiln is divided into cells specified in the heat transfer model. Note that in one axial position there are several cells in the radial and angular directions. The idea is to calculate and store values of temperatures in these cells, thus creating a temperature profile. At the burner position, it is assumed that the flame is at its first axial cell, and at the center of that axial cell, the flame is at its first radial cell. The center of the flame is assumed dense, where no excess air has been mixed. Thus, the excess air ratio may be assumed as 1, and by then using the adiabatic temperature function, this results in a maximum temperature. In the radial direction, closer to the walls, the temperature is assumed to decrease to that of the preheated air, 1200°C, which surrounds the flame cone, Figure 3.10. To clarify, in an axial position on the flame cone there are several cells in the radial and angular directions, where the temperature decreases from the center of the flame towards the surrounding walls, since more air mixes with the flame. Further away from the burner in the second axial position, more air has been consumed, resulting in a higher excess air ratio and lower flame temperatures in the resulting cells. At the last axial position on the flame cone, the preheated air close to the walls is assumed consumed, resulting in the maximum calculated excess air ratio and the corresponding flame temperature at that excess air ratio, see Figures 3.4, 3.7, and 3.8. An example of three axial positions is illustrated in Figure 3.11, where the radius of the flame cone varies at each position. In comparison to the mixing function, depending on the cell resolution specified, the flame cone is divided into several cells in the axial direction, where the distance between each cell is calculated.

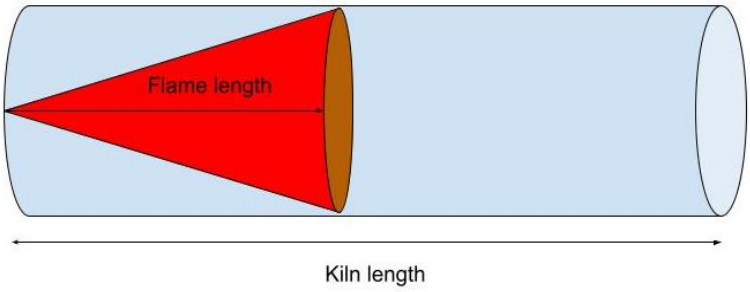

Figure 3.9: The assumed flame shape inside the kiln.

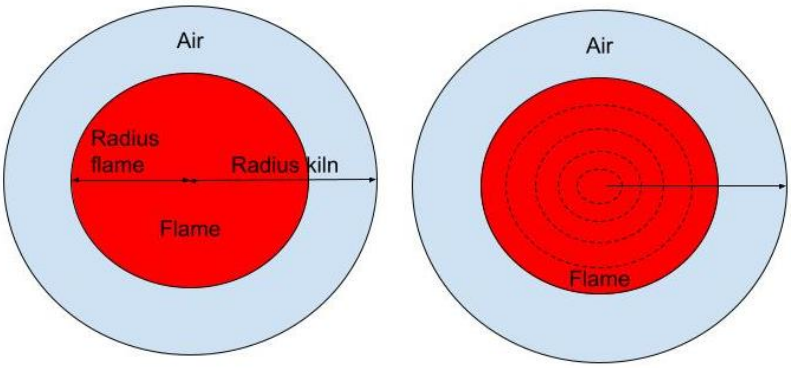

Figure 3.10: The flame cone which includes the flame radius, kiln radius (left), and when it is divided into several radial layers (right).

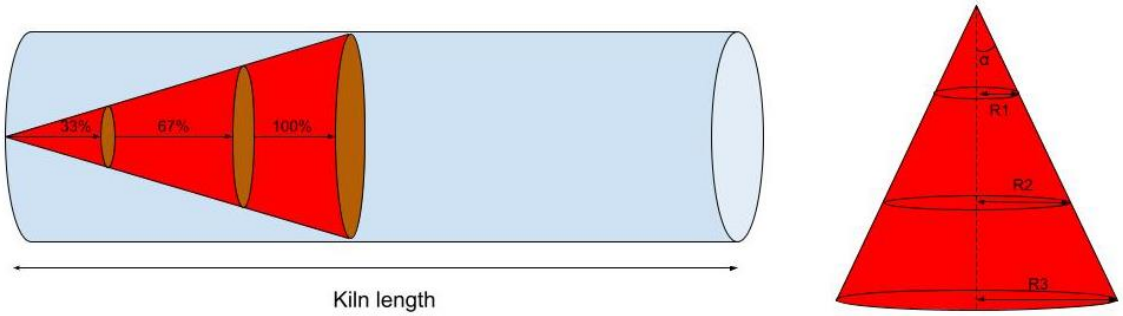

Figure 3.11: The flame cone, where the flame length is divided in 3, both inside the kiln (left) and alone in a vertical position (right).

As the adiabatic flame temperature curves are a function of the excess air ratio, the excess air ratio must be calculated. Thus, the excess air ratio is assumed as the ratio between the number of radial cells occupying the flame cone and the radial cells in the kiln, at a certain axial distance. The ratio is assumed proportional to the maximum calculated excess air ratio, as shown in Equation 3.7. Equation 3.7 is used to calculate the adiabatic temperature at an axial cell and is further used in an energy balance, Equation 3.8. Note that the volume of the flame cone, $V_{flame\ cone}$ is the volume calculated from the axial radius, R_i. T_{air} is the gas temperature from the cooler. $\sum V_{rad.layer}$, is the volume of all flame cone layers, illustrated in Figure, 3.12. T_i, is a temperature function for the radial layers.

Equation 3.7 describes the excess air ratio at an axial position, *i*, which is determined as the radius of an axial position, R_i divided by the radius of the kiln, R_{kiln}. This is then proportional to the maximum excess air ratio, λ_{max}, which is taken from the adiabatic flame temperature function.

$$\lambda_i = \frac{R_i * radial\ cells}{R_{kiln} * radial\ cells} * \lambda_{max} \tag{3.7}$$

$$\dot{Q}_{tot} = A_{flame\ cone} * (T_{adiabatic} - T_{air}) * \rho * Cp = \sum A_{rad.layer} * (T_i - T_{air}) * \rho * Cp \tag{3.8}$$

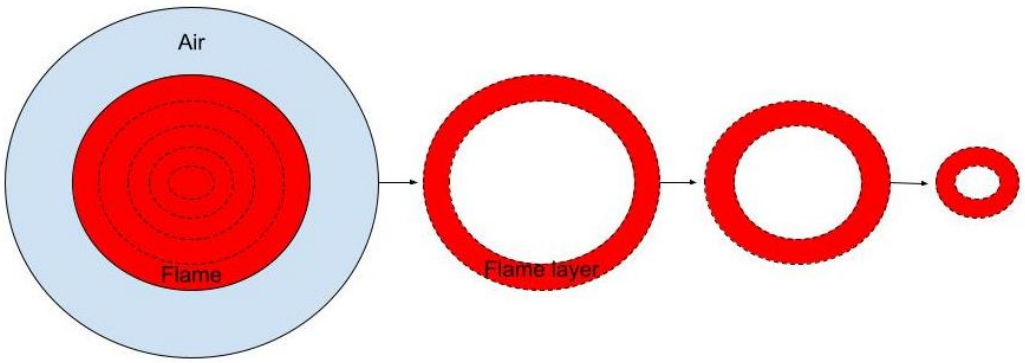

Figure 3.12: The area of each radial cell at an axial cell that occupies the flame cone. This is used in the energy balance.

To determine T_i, each radial cell at the center of the flame cone is assumed to have a guessed peak temperature. A linear function could then be constructed, where the temperature in the different radial cells, which occupies the flame cone could be determined as a function of, a guessed peak temperature, the air temperature, and the number of radial cells.

When, Equation 3.8 is satisfied the iteration ended and the linear function of the guessed peak temperatures, T_i, are imported to the heat transfer model for each axial position. Furthermore, in order to determine the compositions of CO_2 and H_2O in each cell, the temperature function, T_i, together with the adiabatic flame temperature curve, is used to determine the excess air ratio, which is used to calculate the gas concentration from the adiabatic flame temperature function.

3.4 Data input for each studied case

As mentioned in Section 2.3, an initial guess is required as data input in order to specify where the calculations in the heat transfer model will begin. Table 3.6 describes the parameters included in the initial guess for the different fuels studied. Furthermore, a selection of the most interesting cases, hydrogen with added coal particles, oil with different flame lengths, and coal with added hydrogen, were re-simulated with a higher cell resolution to improve the accuracy of the results. This section includes a selection of figures from the data input used with the heat transfer model. A detailed list of all cases studied is listed in Table 3.7, where the corresponding figures of the data input are listed in Appendix B. Note that the data input of the particle and soot concentrations depends on the flame length and cell resolution and causes a changed total amount of particles, hence, may vary depending on the studied case. The particle and soot concentrations in a coal flame are, as mentioned in Section 3.1.2, based on measurements gathered from [25]. The concentrations used for an oil flame are also based on measurements on a pilot scale kiln and gathered from [22]. The data input of the gas concentration is dependent on the excess air ratio, which is dependent on the fuel and composition. The data input of the temperature profile is dependent on the gas temperature from the cooler, to the PH-zone and the adiabatic flame temperature function. Furthermore, the calculated excess air ratio at each axial position the flame occupies is also presented and is dependent on the flame length, number of cells, and the composition of the fuel. In summary, the data input of the temperature and gas concentration profiles are determined by using the flame-air mixing function, which is dependent on the adiabatic flame temperature profile. Note that the adiabatic profile is dependent on the fuel combusted as well as the gas temperature from the cooler, thermal power of the fuel and airflow, taken as process data from a full scale kiln at LKAB.

In order to simplify the assumed flame length in the hydrogen cases, the flame length chosen was the same as the existing oil flame in the heat transfer model, 5.4m. The oil flame length is taken from [11], which is based on the upscaling of experimental data gathered from measurements on a pilot scale furnace at LKAB. The existing coal flame, 11.4m in the heat transfer model, is also taken from [11] and the result of upscaling of experimental data. However, from observations and experiences at LKAB, the flame length may be longer or shorter. To study the effects of the flame length, a hydrogen flame shorter and longer than the assumed 5.4m was chosen. Thus, a 3.4m flame was chosen, which can be hypothesized due to its reactivity and physical properties. To simplify the examination of the effects with a longer hydrogen flame, a flame length that mimics the existing coal flame in the heat transfer model, 11.4m was chosen. For the oil cases, an 11.4m flame was chosen in order to make a simpler and direct comparison to the coal flame. This assumption is strengthened as the same flame length as a coal flame is applied when combusting oil during full scale operation at LKAB. To study a longer coal and oil flame, a flame length of approximately 22m was chosen.

Table 3.6: Parameters included in the initial guess for each fuel studied.

Fuel	Temperature profile	Gas concentration	Particle concentration
Hydrogen gas	Adiabatic flame temperature profile	H_2O	-
Coal	Adiabatic flame temperature profile	CO_2, H_2O	Char, ash and soot
Oil	Adiabatic flame temperature profile	CO_2, H_2O	Soot

Table 3.7 presents the resulting cases used with the heat transfer model, when the supplied heat from the fuel equals the heat transferred in the kiln, thus satisfying the energy balance, see Figure 3.2. The exception is the three hydrogen flame lengths studied in this work with the reference settings as described in detail in Section 4.1.1. The resulting cases were also derived to achieve an adequate radiative contribution from the flame to the bed material in order to acquire a sufficient bed temperature leaving the kiln. Table 3.7 includes the hydrogen cases when increasing gas temperatures, a dissociation case, and the resulting factor of the maximum projected surface area as a factor of coal and IOD particles. Table 3.7 also includes a case where the coal and oil flame lengths were increased as well as the addition of hydrogen to a coal flame, and a case that includes dissociation.

Table 3.7: The resulting cases when the energy balance is solved for the fuels, hydrogen, coal, and oil. The exeption being the reference cases for the hydrogen flames.

Hydrogen gas Case:	Coal Case:	Oil Case:
Reference settings: 3.4m flame	Reference settings: 11.4m flame	Gas temperature to the PH-zone: 1370°C, 11.4m flame.
Reference settings: 5.4m flame		
Reference settings: 11.4m flame	Gas temperature to the PH-zone: 1240°C, 21.8m flame.	
Gas temperature to the PH-zone: 1440°C, 5.4m flame.		
Gas temperature: 1300°C from C1 and 1440°C to the PH-zone, 5.4m flame.	Added hydrogen: 10%, 11.4m flame	
Increase overall gas temperatures: 8%, 5.4m flame		
Dissociation: Reference settings, 5.4m flame	Added hydrogen: 15%, 11.4m flame	Gas temperature to the PH-zone: 1320°C, 21.8m flame.
Coal particles: 13%, 3.4m flame		
Coal particles: 7%, 5.4m flame		
Coal particles: 2.8%, 11.4m flame		
IOD particles: 16%, 3.4m flame	Added hydrogen: 20%, 11.4m flame	Dissociation: 1370°C Gas temperature to the PH-zone, 11.4m flame
IOD particles: 7%, 5.4m flame	Dissociation: Reference settings, 11.4m flame	
IOD particles: 3%, 11.4m flame		

3.4.1 Data input: Hydrogen Case

In this section, the data input of the temperature profile for a 5.4m hydrogen flame with the reference settings is presented in Figure 3.13. Figure 3.13 illustrates the temperature profile as cells with stored temperature values, which are color-coded and calculated from the flame-air mixing function and the adiabatic profile. Figure 3.13 also includes three radial positions equally distributed on the flame length. Figure 3.14 presents the calculated excess air ratios from the flame-air mixing function for each axial position in a 5.4m hydrogen flame. As the excess air ratio increase with the flame length, the flame temperature decrease in accordance to the adiabatic profile, see Figure 3.5. Figure 3.15 shows the gas concentration map of H_2O that is formed during hydrogen combustion in the kiln, which is calculated from the flame-air mixing function and adiabatic profile. As may be noted in Figure 3.13 and 3.15 the values of the cells at the center at the fourth axial position tends to be lower than at the fifth axial position. This may be due to convergence error when iterating the guessed temperature required to satisfy the energy balance, Equation 3.8.

The temperature data input for a hydrogen flame with added coal particles, which is simulated with a higher cell resolution, is presented in Figure 3.16. Figure 3.17 shows the calculated excess air ratio used to obtain the temperature profile shown in Figure 3.16. Figure 3.18 shows the gas concentration map of H_2O for this case. Table 3.8 presents the resulting coal particles needed to solve the energy balance, i.e., the sum of all heat transferred in the kiln is equal to the supplied 35 MW from the fuel, as a factor of the maximum projected surface area as described in Section 3.1.2. Table 3.8 further includes the three different hydrogen flame lengths studied and the resulting particle concentrations obtained from the factor of the projected area. Note that for the reference settings cases, where the flame length is studied, the data input varies, thus not all the data input is presented in this section. Similar figures of the data inputs for the hydrogen cases are listed in Appendix B**.** In summary, the effects of increasing the gas temperatures in the kiln, see Table 3.7, were carried out to simulate and capture the influence on the radiative heat transfer from H_2O to the bed material. By adding particles to the flame the effects of influencing the radiative heat transfer by particle radiation are simulated and studied.

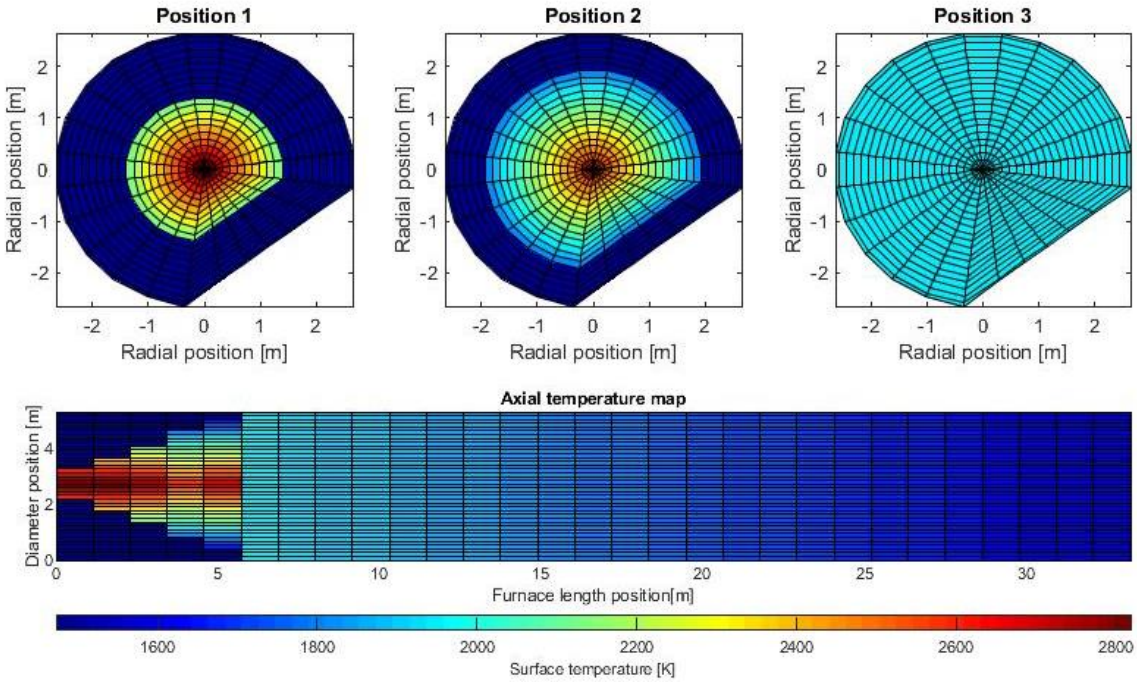

Figure 3.13: The data input of the temperature profile for a 5.4m hydrogen flame with the reference settings.

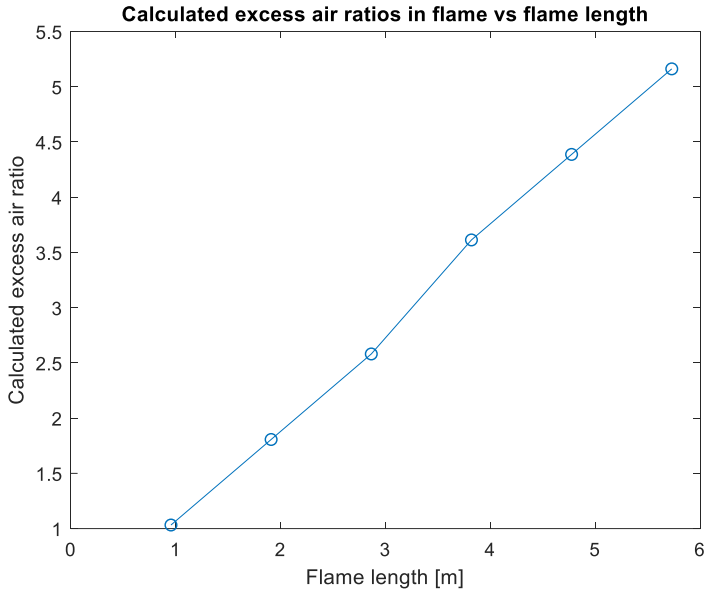

Figure 3.14: The data input of the calculated excess air ratios as a function of the flame length, for a 5.4m hydrogen flame.

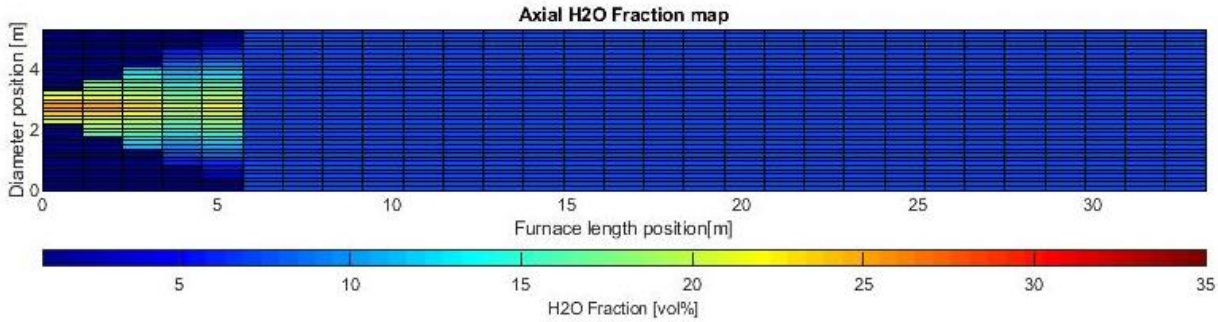

Figure 3.15: The data input of the H_2O concentration for a 5.4m hydrogen flame.

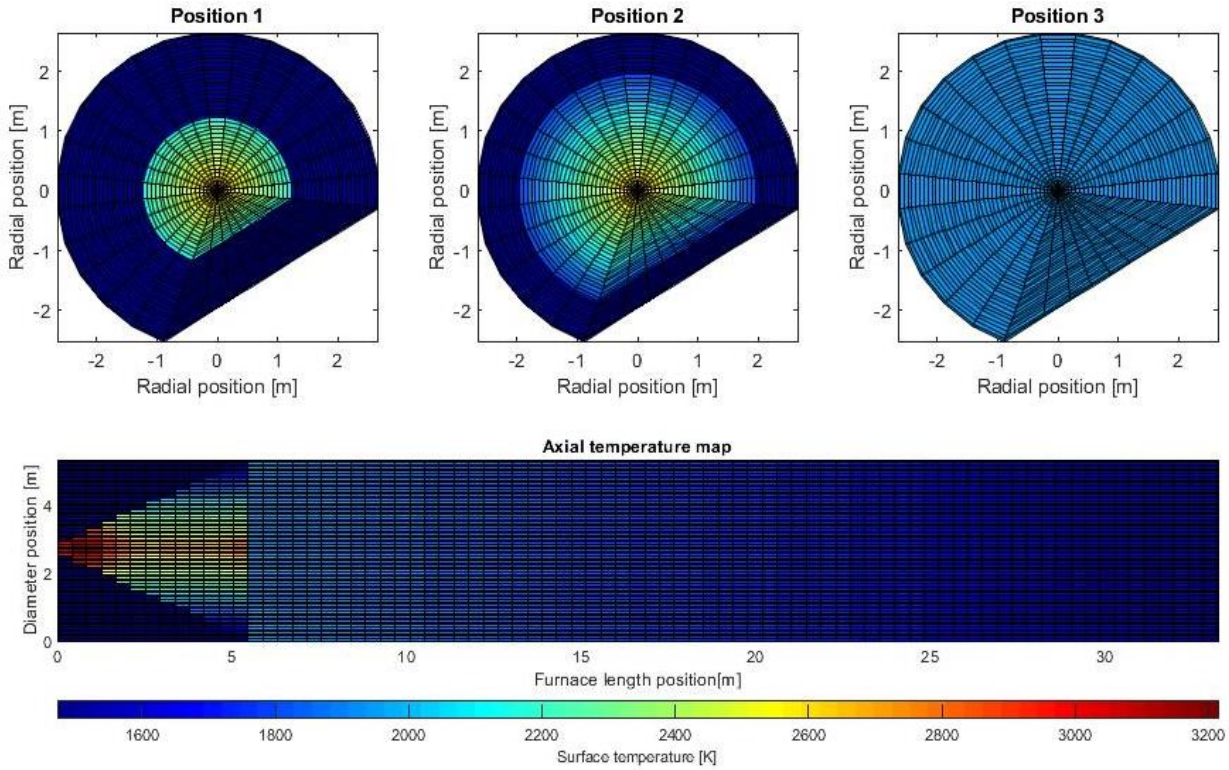

Figure 3.16: The data input of the temperature profile for a 5.4m hydrogen flame with 7% added coal particles.

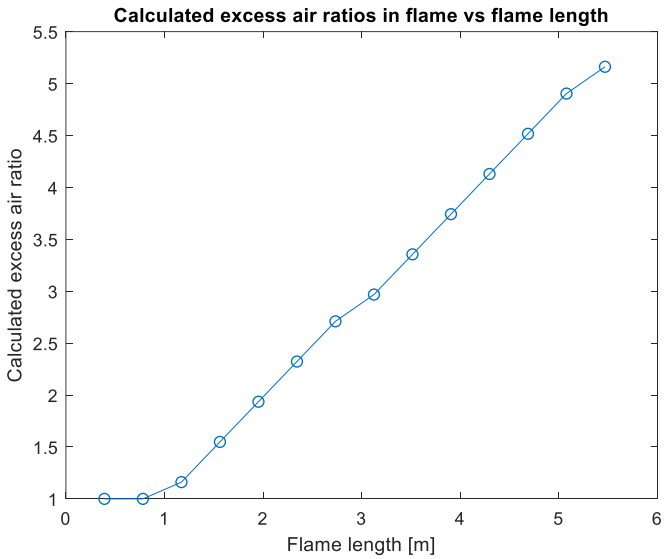

Figure 3.17: The data input of the calculated excess air ratios as a function of the flame length, for a 5.4m hydrogen flame with a higher cell resolution.

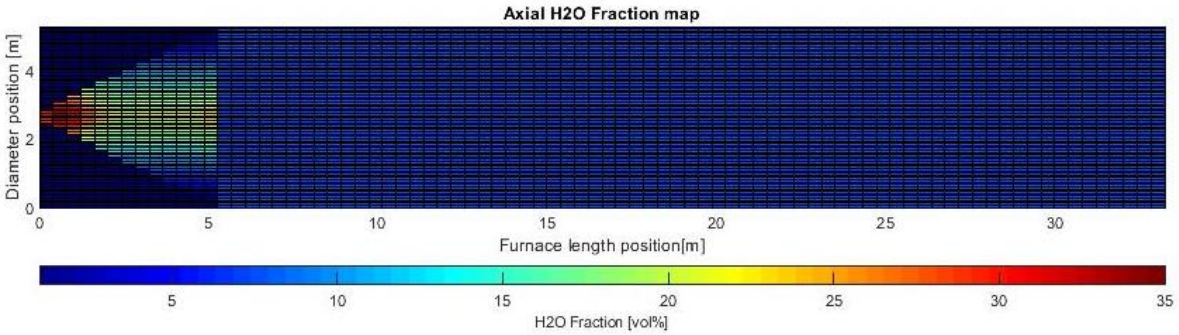

Figure 3.18: The data input of the H_2O concentration for a 5.4m hydrogen flame with a higher cell resolution.

Table 3.8: The data input of the particle concentration for a hydrogen flame with added coal particles. Note that this case was simulated with a higher cell resolution.

Flame length [m]	**Added coal particles in flame [%]**	**Particle concentration $[m^2 particles/m^3 air * 10^{-2}$]**
11.4	2.8	0.79
5.4	7	1.11
3.4	13	1.58

3.4.2 Data input: Coal case

The following section presents the temperature input data for a coal case with a flame length of, 11.4m with the reference settings, see Figure 3.19. The corresponding excess air ratio calculated in the flame-air function and used to obtain the temperature profile is shown in Figure 3.20. Figures 3.21 and 3.22 illustrates the gas concentration map of CO_2 and H_2O formed during combustion, respectively. As can be noted in Figure 3.22 the concentration of H_2O is considerably less than the concentration of CO_2, which is mainly due to the content of carbon (C) and hydrogen (H) in the fuel, see Table 3.3. Lastly, the input data of the particle and soot concentrations for an 11.4m coal flame are listed in Table 3.9. Note that the data input for a 21.8m coal flame and cases with, 10%, 15%, and 20% added H_2 to the coal flame are listed in Appendix B. Increasing the flame length by approximately 10m, see Table 3.7, was carried out to simulate the effects on the radiative heat transfer as particle concentration in the flame is influenced. Adding hydrogen to the coal flame was carried out to simulate the effects of increasing flame temperatures as particle radiation decrease.

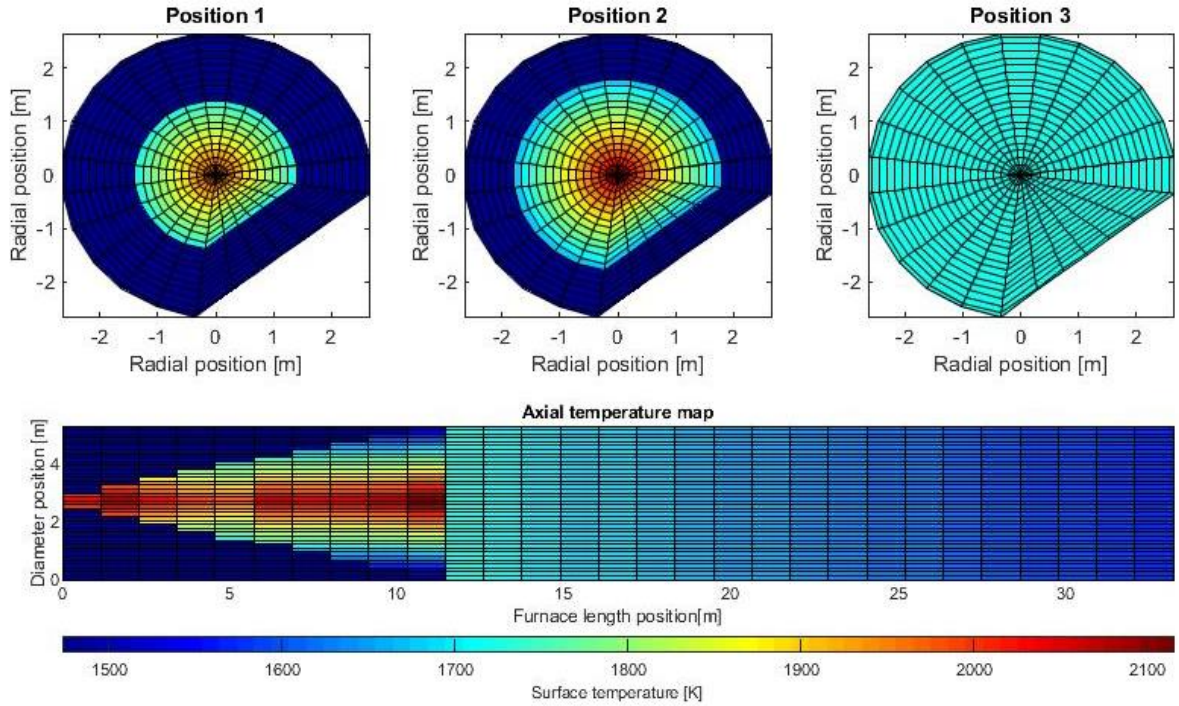

Figure 3.19: The data input of temperature profile of a 11.4m coal flame with the reference settings.

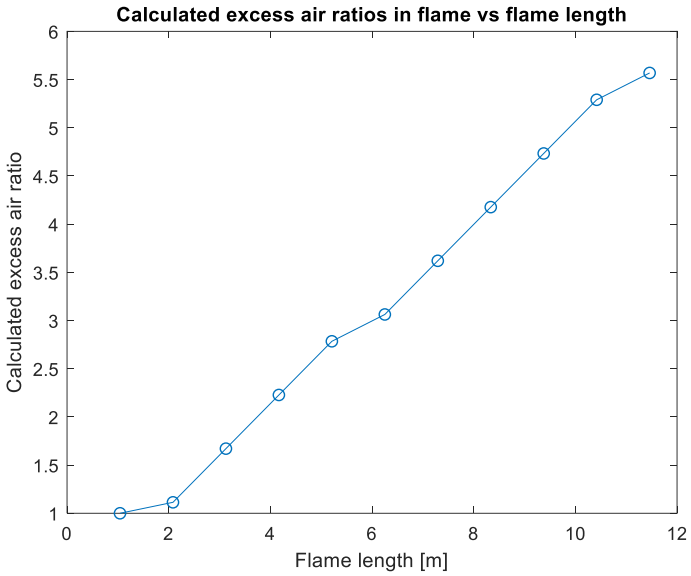

Figure 3.20: The data input of the calculated excess air ratios as a function of the flame length, for a 11.4m coal flame.

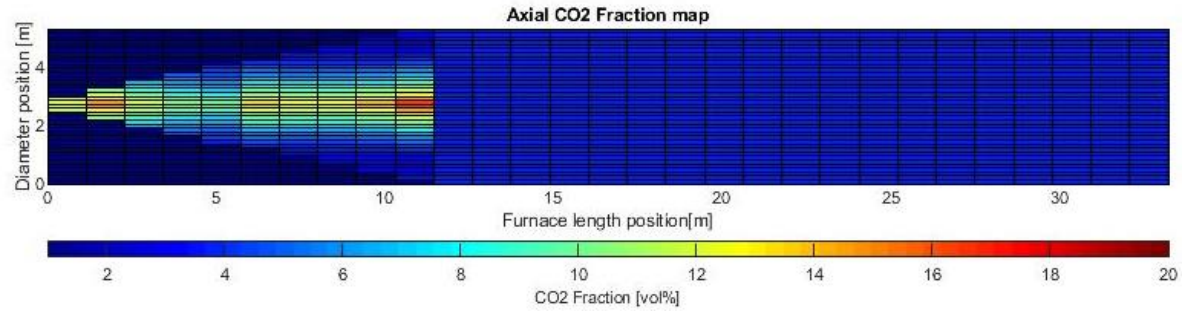

Figure 3.21: The data input of the CO_2 concentration for a 11.4m coal flame.

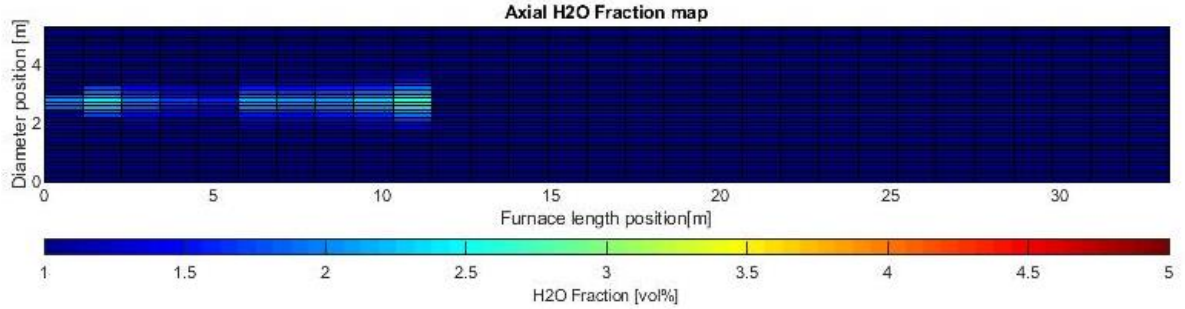

Figure 3.22: The data input of the H_2O concentration for a 11.4m coal flame.

Table 3.9: The data input of the particle concentration of coal particles and soot particles for a 11.4m coal flame.

Particle concentration: Coal flame 11.4m	**Soot concentration: Coal flame 11.4m**
$27.1*10^{-2}$ $[m^2 particles/m^3 air]$	$2.75*10^{-9}[m^2 soot/m^3 air]$

3.4.3 Data input: Oil case

In this section, the data input for an 11.4m oil flame, where the gas temperature to the PH-zone had to be increased to 1370°C in order to solve the energy balance is presented. The temperature profile of the data input is presented in Figure 3.23, where a higher cell resolution has been applied. The calculated excess air ratios used to obtain the temperature profile, see Figure 3.23 are presented in Figure 3.24. If the calculated excess air ratio results in a value below 1 the flame-air mixing function assigns an excess air ratio of 1, which may explain the line seen in Figure 3.24. The corresponding gas concentration maps of CO_2 and H_2O are presented in Figures 3.25 and 3.26, respectively. Table 3.10 presents the corresponding particle and soot concentration for the oil flame, gathered from [22]. The data input for a 21.8m oil flame is listed in Appendix B. Increasing the flame length by approximately 10m, see Table 3.7, was carried out to simulate the effects on radiative heat transfer as particle concentration in the flame is influenced.

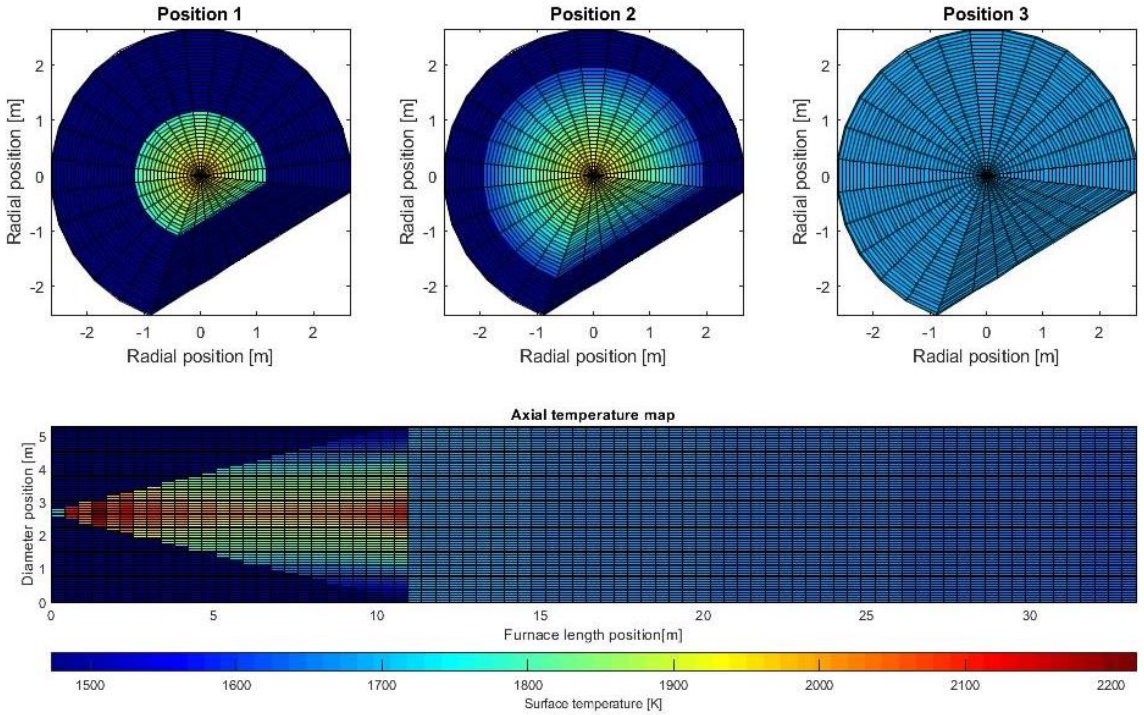

Figure 3.23: The data input of temperature profile of an 11.4m oil flame with a gas temperature of 1370°C to the PH-zone.

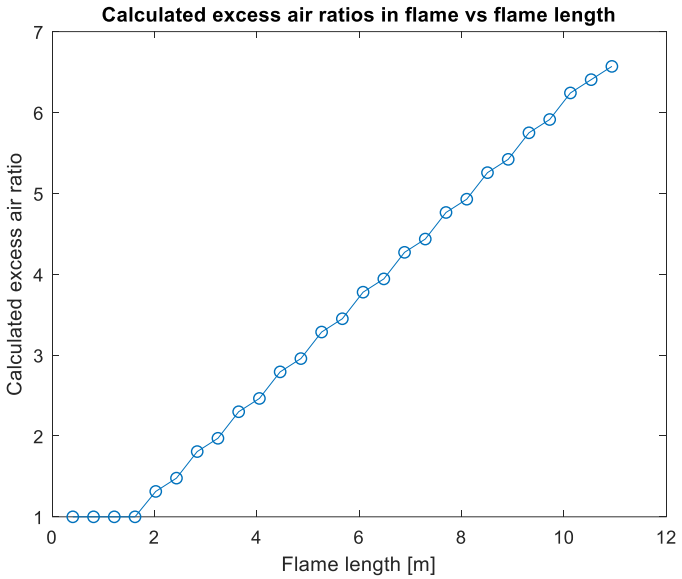

Figure 3.24: The data input of the calculated excess air ratios as a function of the flame length, for an 11.4m oil flame.

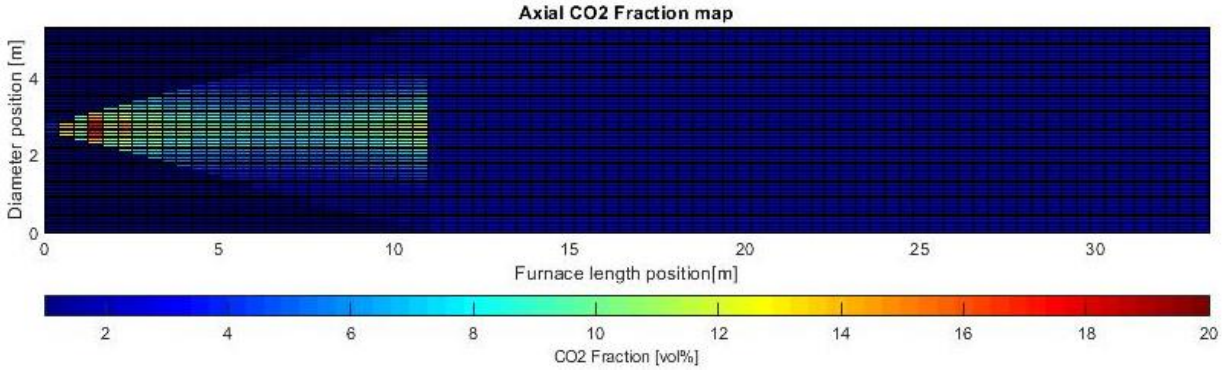

Figure 3.25: The data input of the CO_2 concentration for an 11.4m oil flame.

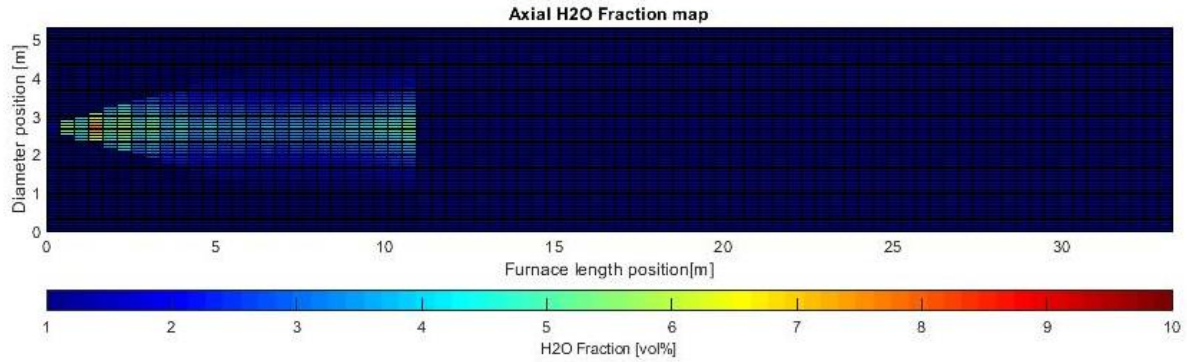

Figure 3.26: The data input of the H_2O concentration for an 11.4m oil flame.

Table 3.10: The data input of the particle and soot concentration for a 11.4m oil flame. Note that the oil flame was simulated with a higher number of cells than the coal flame.

Particle concentration: Oil flame 11.4m	**Soot concentration: Oil flame 11.4m**
$23.0*10^{-2}$ $[m^2 particles/m^3 air]$	$2.26*10^{-9}[m^2 soot/m^3 air]$

4.

Results & Discussion

In this section, the results from the cases described in Section 3.1.2, are presented. The results are listed in tables that include some of the constant parameters. The bed and wall temperature profiles are also included for the studied cases. At the end of each result section, the results are followed by a discussion. An energy diagram is also included for a selection of one of the cases in each study. This serves as an overview of the energy balance over the kiln. Furthermore, in the case of including dissociation or not, the result yielded a similar bed and wall temperature profile. Thus, the bed and wall temperature profile for the dissociation case is not included. All cases aim to satisfy the energy balance, Figure 3.2, where the supplied thermal power equals the total heat transferred within the kiln. The cases further aim to achieve a heat transfer load to the pellet bed that obtains a bed temperature exiting the kiln similar to a coal or oil flame since its desired for the heat treatment of the pellets.

4.1 Results from Hydrogen cases

4.1.1 Hydrogen: Reference settings

Table 4.1 presents the constant parameters and the results from each calculated parameter for a hydrogen flame with different flame lengths, using the reference settings described in Section 3.1.1, where the thermal power from the fuel is constant for all cases as 35 MW.

Table 4.1: The studied constant parameters and the results of the heat transfer model (listed as calculated parameters) from the hydrogen flames reference settings study. Note that the energy balance is unsolved for the cases studied here.

Constant Parameters	**Unit**	**Case: Hydrogen 3.4m**	**Case: Hydrogen 5.4m**	**Case: Hydrogen 11.4m**	**Case: Dissociation, 5.4m**
Bed temperature in	(°C)	1000	1000	1000	1000
Gas temperature from cooler	(°C)	1200	1200	1200	1200
Gas temperature to the PH-zone	(°C)	1300	1300	1300	1300
Particles in flame	(%)	0	0	0	0
Thermal power from fuel	(MW)	35	35	35	35
Calculated Parameters	**Unit**	**Case: Hydrogen 3.4m**	**Case: Hydrogen 5.4m**	**Case: Hydrogen 11.4m**	**Case: Dissociation, 5.4m**
Bed temperature out	(°C)	1200	1203	1206	1201
Max. Calculated adiabatic flame temp	(°C)	2969	2969	2969	2659
Max. Kiln wall temperature	(°C)	1279	1283	1284	1280
Radiation to bed	(MW)	13.5	14.2	15.3	14
Convection to bed	(MW)	4.6	4.3	3.7	4.3
Conduction to bed	(MW)	0.73	0.8	0.81	0.8
Total heat to gas	(MW)	6.2	6	5.9	6
Outer heat losses	(MW)	0.79	0.79	0.8	0.8
Total heat to bed	(MW)	18.9	19.3	19.7	19.1
Sum of all heat transferred in kiln:	(MW)	25.8	26.2	26.4	25.9

From the results, it can be concluded that the flame length of a hydrogen flame with the reference settings results in an unsolved energy balance as the sum of all heat transferred is not equal to the supplied thermal power as seen in Table 4.1. This means that more energy in the flue gases is exiting the kiln than the energy specified from the gas temperature to the PH-zone.

Thus, the gas temperature to the PH-zone should hold a higher value in order to solve the balance. Furthermore, similar bed temperatures exiting the kiln, which does not reach a sufficiently high temperature are obtained. The effect of including dissociation did not have a significant impact on the result. It did, however, decrease the flame temperatures and the concentration of H_2O, thus decreasing the heat transfer due to radiation. As may be concluded from Table 4.1 influencing the flame length affects the radiative heat transfer, which in consequence, affects the convective heat transfer to the bed material. The radiation to the bed material increases with a longer flame since the volume of hot gases from the flame increases, leading to a higher gas concentration of H_2O. As the flame length increases the length of the radiating part of the flame, where radiation dominates increases, leading to a higher radiative heat transfer, increasing the temperature of the bed material. This reduces the temperature difference between the hot gases and the bed material, thus decreasing the convective heat transfer in accordance to Equation 2.3. This results in similar bed temperatures exiting the kiln for the studied flame lengths. Since the flame lengths did not have a significant impact on the results, a 5.4m hydrogen flame is used in further modeling cases, except for in the particle studies. Figure 4.1 illustrates an energy diagram for a 5.4m hydrogen flame with the reference settings. The energy diagram describes the heat sources, heat sinks, and an error margin, which is the heat transfer needed to solve the energy balance as well as the calculated radiation, convection, and conduction to the bed material in the kiln. It should also be noted that, as mentioned, the energy balance remains unsolved for the hydrogen flames studied in this section. From Figure 4.1, it can, however, be concluded that the majority of the heat transfer to the bed material lies with the heat transfer due to radiation. From the heat transfer model, a bed and wall temperature profile is obtained, which describes the surrounding kiln wall temperature throughout the length of the kiln as color-coded cells. The resulting bed temperature profile is also included to the right of the kiln wall profile in the figure. Figure 4.2 describes the bed and kiln wall temperature profile for a 5.4m hydrogen flame with the reference settings, where it can be concluded that the temperature of the wall and bed increases closer to the flame. In summary, as seen in Figure 4.3, an uneven heat transfer load to the pellet bed is achieved for the studied 5.4m hydrogen flame.

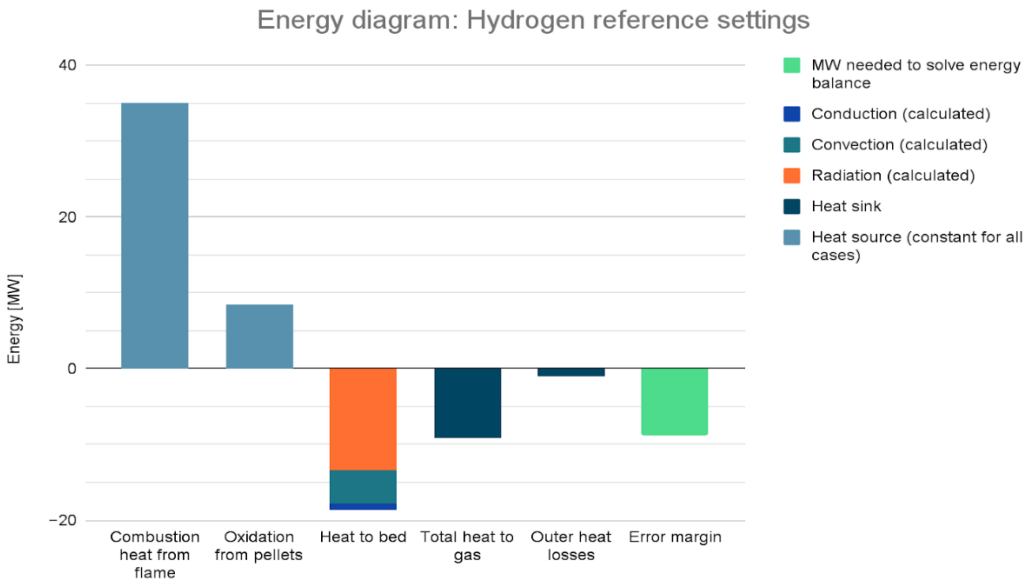

Figure 4.1: The heat sinks, heat sources, error margin, and calcuated radiation, convection, and conduction in the kiln for a 5.4m hydrogen flame with the reference settings, where the energy balance is unsolved.

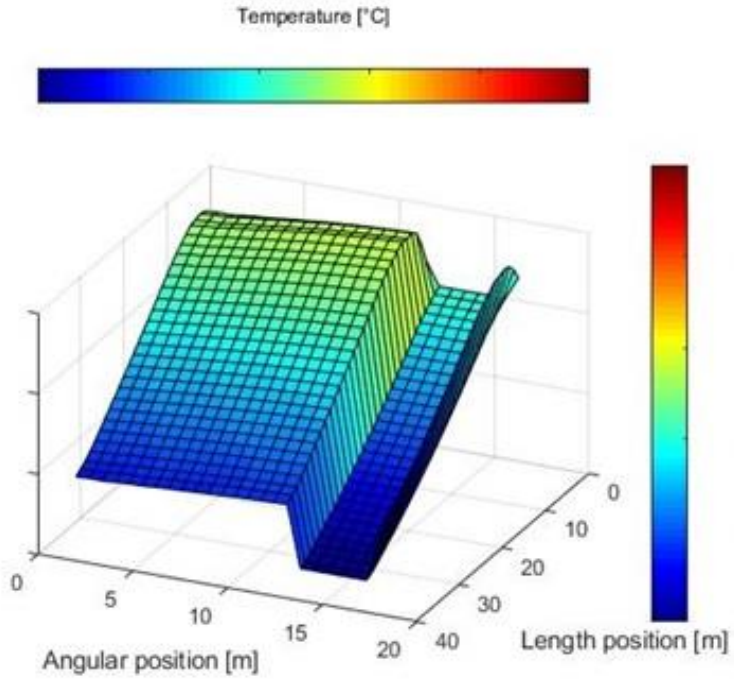

Figure 4.2: The bed and wall temperature profile for a 5.4m hydrogen flame with the reference settings.

4.1.2 Hydrogen: Temperature studies

This section presents the results from the temperature studies for a 5.4m hydrogen flame. The results from the heat transfer model are listed in Table 4.2, describing the percentage increase in temperature from that of the reference settings in all the cells required in order to solve the energy balance. Furthermore, Table 4.2 presents a case, where the gas temperatures from the cooler and to the PH-zone were studied, respectively.

Table 4.2: The studied constant parameters (extra bold) and the results of the heat transfer model (listed as calculated parameters) from the hydrogen flames temperature study.

Constant Parameters	**Unit**	**Case: 8% increase of all gas temperatures**	**Case: Gas temperature from cooler**	**Case: Gas temperature to PH**	**Case: Gas temperature to PH & from cooler**
Bed temperature in	(°C)	1000	1000	1000	1000
Gas temperature from cooler	(°C)	**1318**	**1400**	1200	**1300**
Gas temperature to the PH-zone	(°C)	**1426**	1300	**1440**	**1440**
Particles in flame	(%)	0	0	0	0
Thermal power from fuel	(MW)	35	35	35	35
Calculated Parameters	**Unit**	**Case: 8% increase of all gas temperatures**	**Case: Gas temperature from cooler**	**Case: Gas temperature to PH**	**Case: Gas temperature to PH & from cooler**
Bed temperature out	(°C)	1252	1247	1224	1246
Max. Calculated adiabatic flame temp	(°C)	3206	3091	2969	3030
Max. Kiln wall temperature	(°C)	1357	1346	1297	1330
Radiation to bed	(MW)	20.6	18.9	16.3	18.7
Convection to bed	(MW)	5.7	5.5	4.9	5.5
Conduction to bed	(MW)	1	0.95	0.86	0.95
Total heat to gas	(MW)	6.6	-5.9	12.9	8.3
Outer heat losses	(MW)	0.84	0.82	0.81	0.83
Total heat to bed	(MW)	27.3	25.4	22.1	25.1
Sum of all heat transferred in kiln:	(MW)	34.8	20.4	35.7	34.2

In Figure 4.3, an energy diagram for the case of a 5.4m hydrogen flame, where all gas temperatures are increased is presented, which may as mentioned in Section 4.1.1 serves as an overview of the heat sources, sinks as well as the calculated radiation, convection, and conduction in the kiln. Figure 4.4 describe the bed and wall temperature profiles for a case where all gas temperatures in all cells were increased by 8%. Figure 4.5 illustrates the effects on the profile as the gas temperature from the cooler increases to 1400°C. Figure 4.6 illustrates the profile when the gas temperature to the PH-zone increase to 1440°C. Lastly, Figure 4.7 shows the effects on the profile when using a 1300°C gas temperature from the cooler and 1440°C to the PH-zone. It can be concluded that an uneven bed and wall temperature profile is obtained as illustrated in Figures 4.4, 4.5, 4.6, and 4.7 for the cases listed in Table 4.2 in comparison to the cases presented in Sections 4.2 and 4.3.

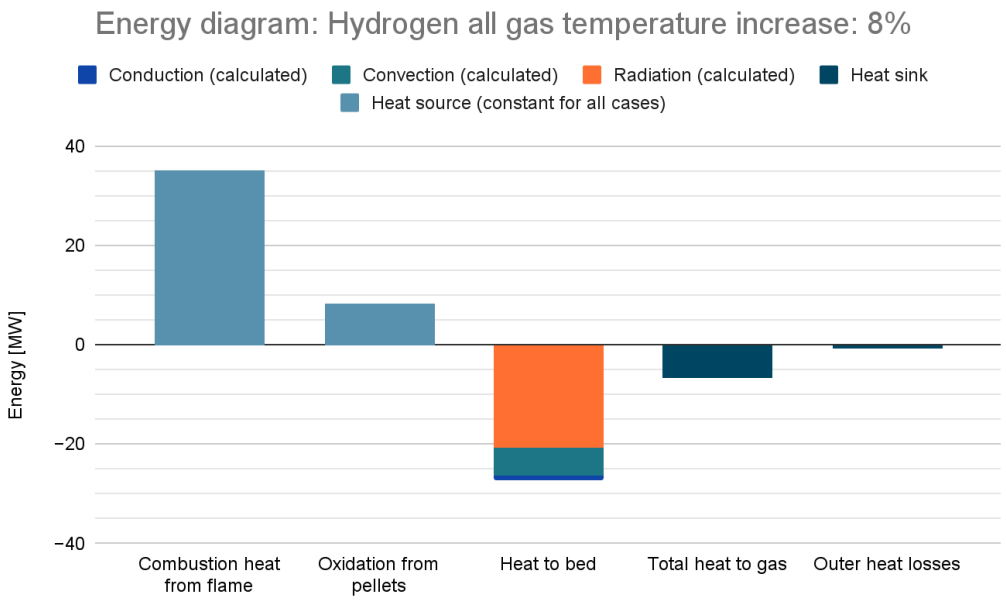

Figure 4.3: The heat sinks, heat sources, and calcuated radiation, convection, and conduction in the kiln for a 5.4m hydrogen flame with an 8% gas temperature increase in all cells.

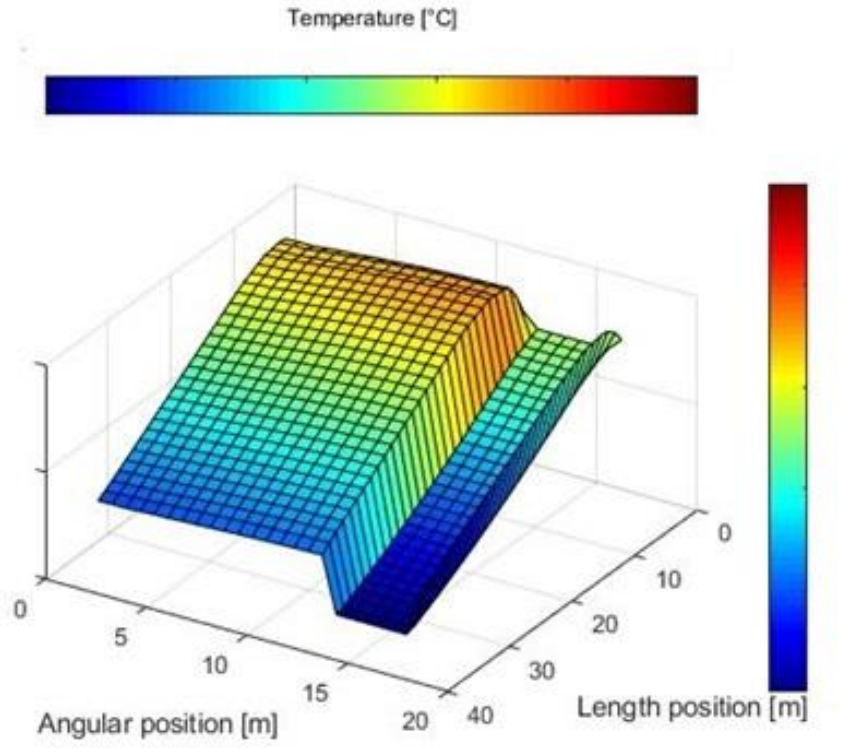

Figure 4.4: The bed and wall temperature profile for a 5.4m hydrogen flame with 8% increased gas temperatures.

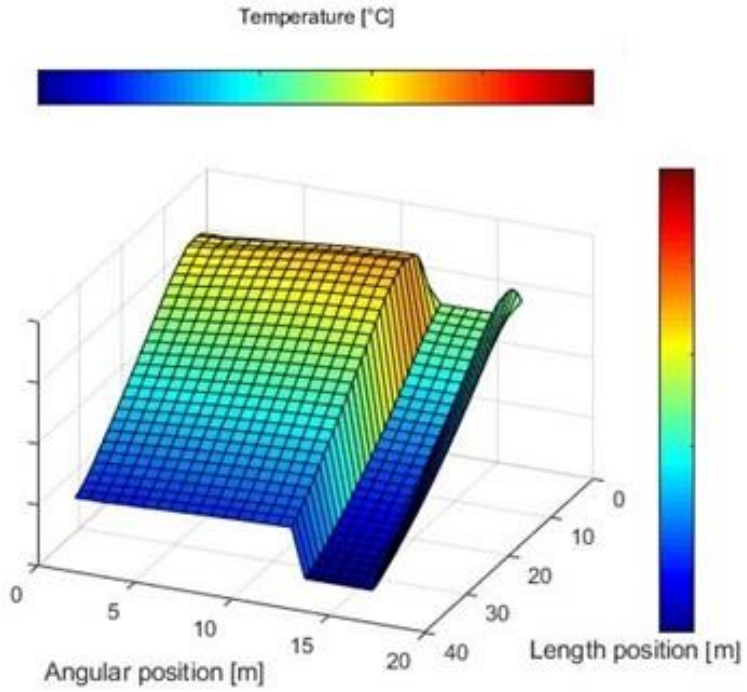

Figure 4.5: The bed and wall temperature profile for a 5.4m hydrogen flame with a gas temperature of 1400°C from the cooler.

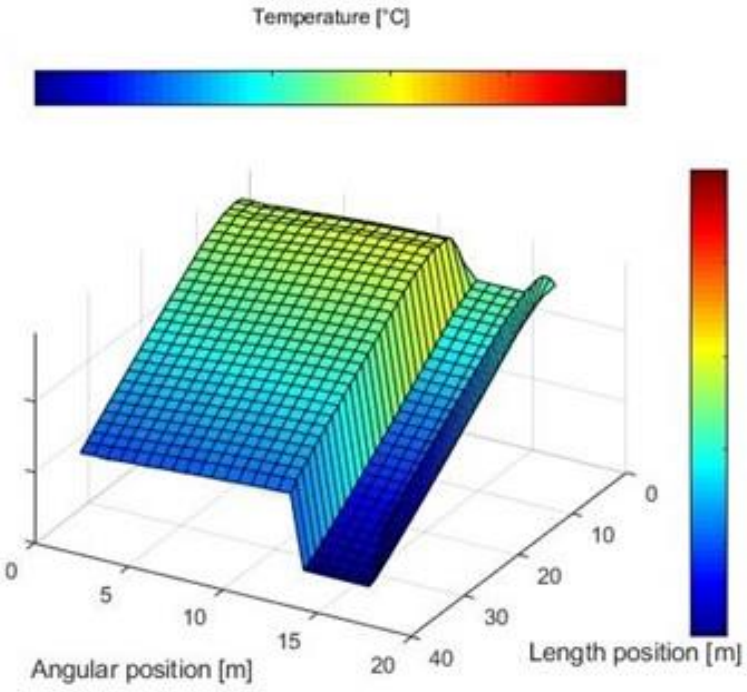

Figure 4.6: The bed and wall temperature profile for a 5.4m hydrogen flame with a gas temperature of 1440°C to the PH-zone.

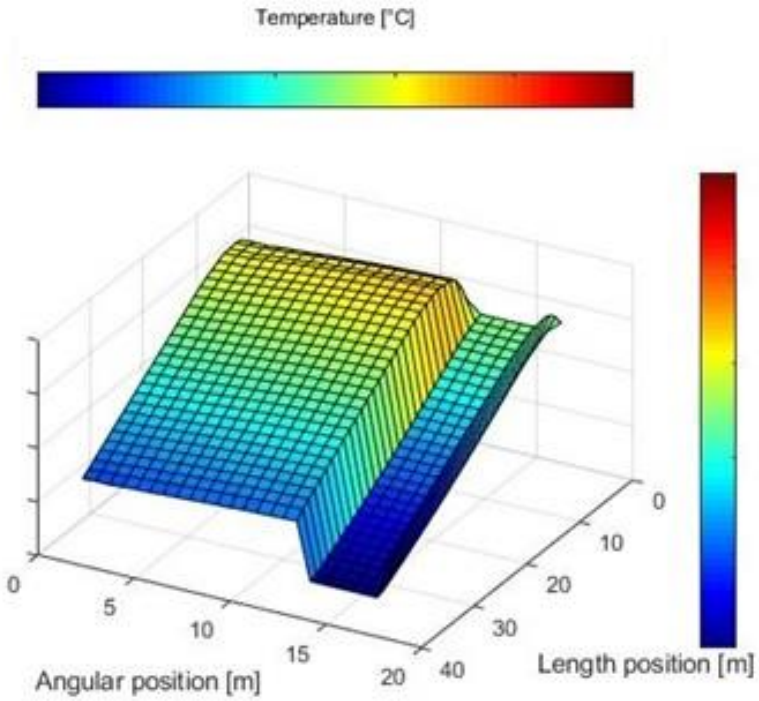

Figure 4.7: The bed and wall temperature profile for a 5.4m hydrogen flame with a 1300°C gas temperature from the cooler and a 1440°C gas temperature to the PH-zone.

An increased temperature from the cooler that is higher than the temperature to the PH-zone, results in more energy absorbed from the preheated air than the energy of the flue gases produced from the combustion process. This results in the calculated parameter, total heat to gas, becoming negative, leading to an unsolved energy balance. However, as shown from the results, increasing the temperature of the gas from the cooler also increases the adiabatic flame temperature, which increases flame temperatures, affecting the radiative, convective, and conductive heat transfer mechanisms. The effects of increasing flame temperatures are also shown on the bed and wall temperature profile, see Figures 4.4 and 4.5. The gas temperature to the PH-zone describes the energy old by the leaving the kiln. It can be concluded from the results that by iteratively increasing the PH-zone temperature, the energy balance may be solved. Note that the parameter, total heat to gas, increases with increasing the gas temperature to the PH-zone since more energy is produced from combustion than absorbed from the supplied preheated air. By doing so, the temperatures in the kiln increases, thus increasing the heat transfer due to radiation, convection, and conduction. From the results of increasing the gas temperature from the cooler and to the PH-zone, the energy balance may also be solved. The effects of higher flame and flue gas temperatures in the kiln increase radiation, convection, conduction, and the total heat to gas as well. Alternatively, as presented in Table 4.2, increasing all gas temperatures by 8% solved the energy balance by using the reference settings. Note that the result of increasing all gas temperatures serves as an example of the required increase needed in all cells in order to solve the energy balance and would not be possible in reality. The reason is that the cells corresponding to the gas temperature from the cooler will increase, leading to increased flame temperature. Then the cells corresponding to the flame temperature will also increase by 8%, thus may result in a flame temperature higher than the calculated maximum adiabatic temperature, which may not be very realistic.

In conclusion, increasing the gas temperatures results in a higher energy flux from the radiation of H_2O, see Equation 2.1, to the pellet bed as well as the surrounding wall. An increased wall temperature inside the kiln follows, thus increasing the surface radiation from the wall to the bed material. A warmer wall increase the conductive heat transfer and warmer gases increase the heat transfer from convection in accordance to Equations 2.3 and 2.4. As a result of the increase in radiation, convection, and conduction to the bed material, the bed temperature exiting the kiln increases as well.

Influencing the gas temperatures may, however, cause complications in the grate-kiln process. Increasing the gas temperature from the cooler may be achieved by adding supplementary firing with a non-CO_2 emitting fuel between the kiln and the cooler. Without supplementary firing, increasing the gas temperature from the cooler would require more energy from the cooler. If the bed temperature exiting the kiln is constant, then this would decrease the supplied energy to the grate system, resulting in a less dried pellet bed with a lower degree of oxidation fed to the kiln. Furthermore, the consequence of increasing the gas temperature to the PH-zone is that the temperature of the bed material entering the kiln increases. If the bed temperature fed to the kiln is constant at 1000℃, the mass flow of pellets may be reduced in order to compensate for the increased gas energy in the PH-zone. Alternatively, in order to keep the mass flow of pellets and the bed temperature constant, the excess gas energy to the PH-zone may be directed to the stack after preheating to the desired bed temperature. This would, however, decrease the effectiveness of the process. Note that these complications are not included in the simulations since the heat transfer model only includes the energy balance over a kiln. The heat sources are limited in this master thesis work by the assumptions listed in Figure 3.1. Furthermore, this exceeds the scope of this master thesis work and is not further discussed.

4.1.3 Hydrogen: Particle studies

In Table 4.3, the constant parameters are listed where the particles in the flame that were studied are listed with extra bold characters. The factor of, particles in flame, listed in Table 4.3 describes the factor of the maximum projected surface area of coal particles, as mentioned in Section 3.1.2, required in order for the supplied heat from the fuel to be equal to the sum of all heat transferred in the kiln. Furthermore, as mentioned in Section 3.2.2, in the coal particle study, a higher number of cells were used in order to improve the accuracy of the results. Figure 4.8 shows the heat sources, heat sinks, and calculated radiation, convection, and conduction for a 5.4m hydrogen flame with 7% added coal particles. Figures 4.9, 4.10, and 4.11 illustrate the bed and wall temperature profiles of a 3.4m. 5.4m and 11.4m hydrogen flame with 13%, 7%, and 2.8% added coal particles, respectively. Furthermore, the data input of the temperature profile, gas concentration, and calculated excess air ratios as a function of the flame length, are the same as a 3.4m, 5.4m, and 11.4m hydrogen flame and are listed in, Appendix B.

Table 4.3: The studied constant parameters (extra bold) and the results of the heat transfer model (listed as calculated parameters) from the hydrogen flames coal particle study.

Constant Parameters	**Unit**	**Case: Hydrogen 3.4m**	**Case: Hydrogen 5.4m**	**Case: Hydrogen 11.4m**
Bed temperature in	(°C)	1000	1000	1000
Gas temperature from cooler	(°C)	1200	1200	1200
Gas temperature to the PH-zone	(°C)	1300	1300	1300
Particles in flame	(%)	**13**	**7**	**2.8**
Thermal power from fuel	(MW)	35	35	35
Calculated Parameters	**Unit**	**Case: Hydrogen 3.4m**	**Case: Hydrogen 5.4m**	**Case: Hydrogen 11.4m**
Bed temperature out	(°C)	1276	1280	1308
Max. Calculated adiabatic flame temp	(°C)	2969	2969	2969
Max. Kiln wall temperature	(°C)	1498	1494	1469
Radiation to bed	(MW)	21.5	22.1	24.2
Convection to bed	(MW)	5	4.8	3.8
Conduction to bed	(MW)	1	1	1.1
Total heat to gas	(MW)	5.9	5.8	5.8
Outer heat losses	(MW)	0.93	0.94	0.96
Total heat to bed	(MW)	27.5	27.9	29
Sum of all heat transferred in kiln:	(MW)	34.3	34.6	35.7

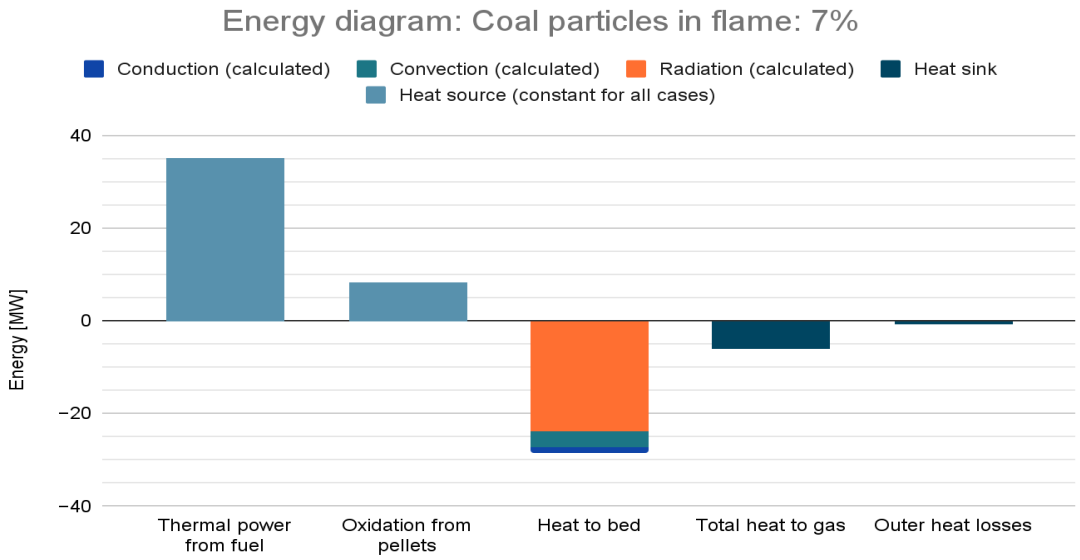

Figure 4.8: The heat sources, heat sinks as well as the calculated radiation, convection, and conduction in the kiln for a 5.4m hydrogen flame with 7% added coal particle.

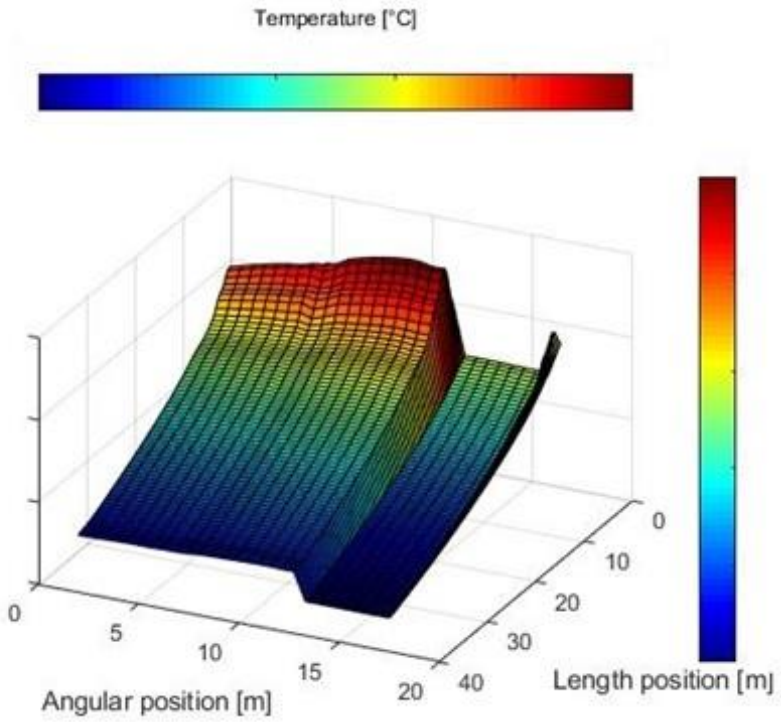

Figure 4.9: The bed and wall temperature profile for a 3.4m hydrogen flame with 13% added coal particles.

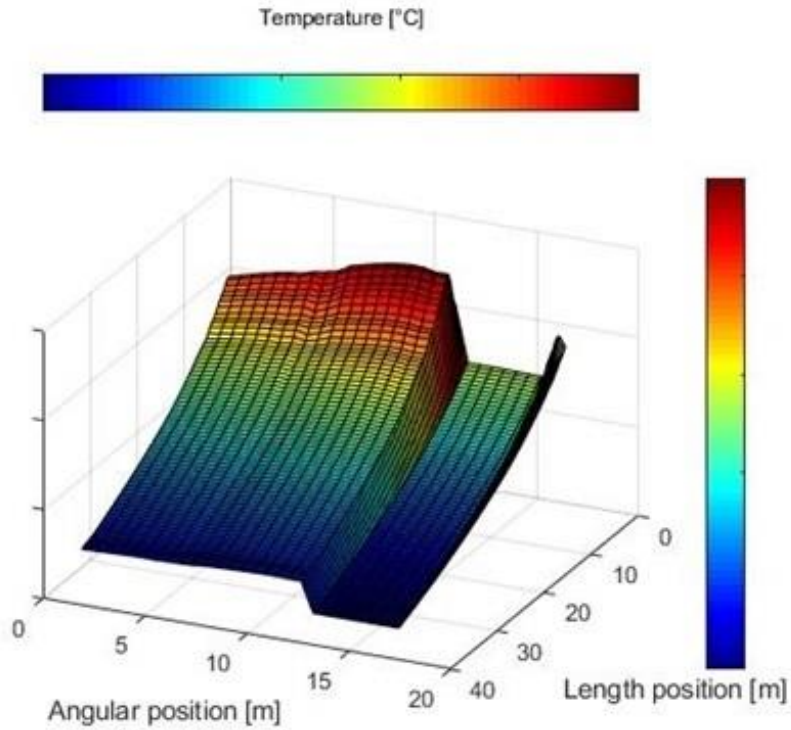

Figure 4.10: The bed and wall temperature profile for a 5.4m hydrogen flame with 7% added coal particles.

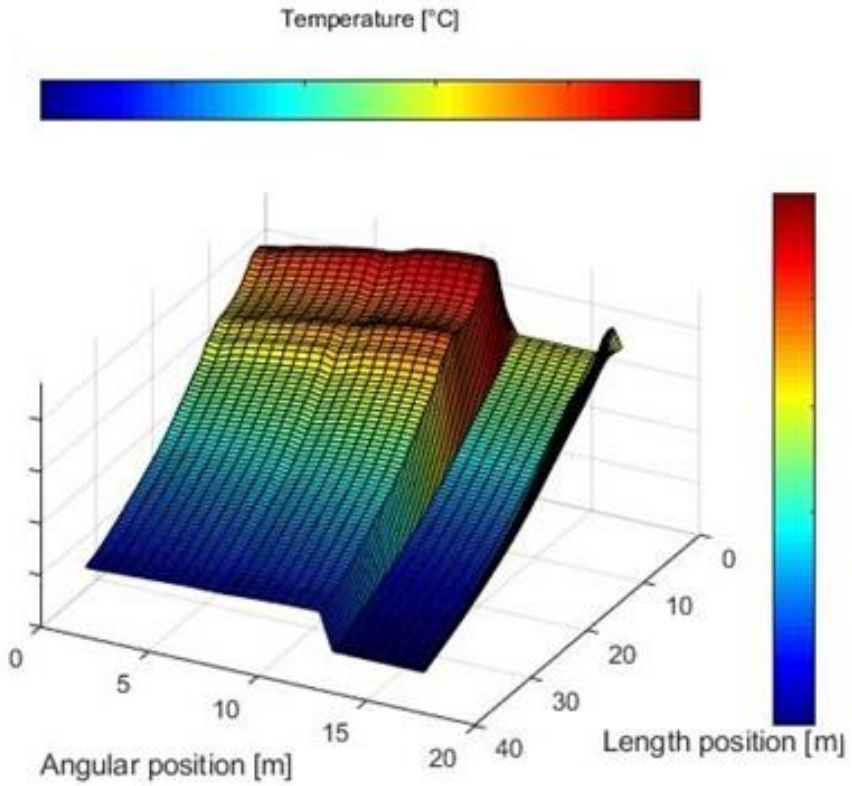

Figure 4.11: The bed and wall temperature profile for a 11.4m hydrogen flame with 2.8% added coal particles.

Table 4.4: The studied constant parameters (extra bold) and the results of the heat transfer model (listed as calculated parameters) from the hydrogen flames IOD particle study

Constant Parameters	**Unit**	**Case: Hematite [26]**	**Case: Magnetite [27]**	**Case: Hematite in ash [28]**	**Case: Simulated optical values, [29]**
Bed temperature in	(°C)	1000	1000	1000	1000
Gas temperature from cooler	(°C)	1200	1200	1200	1200
Gas temperature to the PH-zone	(°C)	1300	1300	1300	1300
Particles in flame	(%)	**7**	**8**	**21**	**100**
Thermal power from fuel	(MW)	35	35	35	35
Calculated Parameters	**Unit**	**Case: Hematite [26]**	**Case: Magnetite [27]**	**Case: Hematite in ash [28]**	**Case: Simulated optical values, [29]**
Bed temperature out	(°C)	1260	1262	1265	1234
Max. Calculated adiabatic flame temp	(°C)	2969	2969	2969	2969
Max. Kiln wall temperature	(°C)	1477	1485	1493	1421
Radiation to bed	(MW)	22.6	22.8	23.2	18.9
Convection to bed	(MW)	4.2	4.2	4.2	4.3
Conduction to bed	(MW)	1.1	1.1	1.1	1
Total heat to gas	(MW)	6.1	6.1	6.1	6.1
Outer heat losses	(MW)	0.83	0.83	0.83	0.897
Total heat to bed	(MW)	27.8	28.1	28.5	24.2
Sum of all heat transferred in kiln:	(MW)	34.7	35	35.4	31

A study using the optical properties of IOD from [26] with the three different hydrogen flame lengths, 3.4m, 5.4m, and 11.4m, are presented in Table 4.5. The corresponding bed and wall temperature profiles for a 3.4m, 5.4m, and 11.4m hydrogen flame with 16%, 7%, and 3% added IOD particles are presented in Figures 4.12, 4.13, 4.14.

Table 4.5: The results from the iron ore dust particle cases with different hydrogen flame lengths, using the optical properties form source [26].

Constant Parameters	**Unit**	**Case: Hydrogen 3.4m**	**Case: Hydrogen 5.4m**	**Case: Hydrogen 11.4m**
Bed temperature in	(°C)	1000	1000	1000
Gas temperature from cooler	(°C)	1200	1200	1200
Gas temperature to the PH-zone	(°C)	1300	1300	1300
Particles in flame	(%)	**16**	**7**	**3**
Thermal power from fuel	(MW)	35	35	35
Calculated Parameters	**Unit**	**Case: Hydrogen 3.4m**	**Case: Hydrogen 5.4m**	**Case: Hydrogen 11.4m**
Bed temperature out	(°C)	1258	1271	1267
Max. Calculated adiabatic flame temp	(°C)	2969	2969	2969
Max. Kiln wall temperature	(°C)	1487	1449	1401
Radiation to bed	(MW)	22.1	21.9	23.5
Convection to bed	(MW)	4.5	4.8	3.4
Conduction to bed	(MW)	1.1	1	1.1
Total heat to gas	(MW)	6.2	5.8	5.9
Outer heat losses	(MW)	0.83	0.94	0.84
Total heat to bed	(MW)	27.7	27.6	28
Sum of all heat transferred in kiln:	(MW)	34.7	34.4	34.7

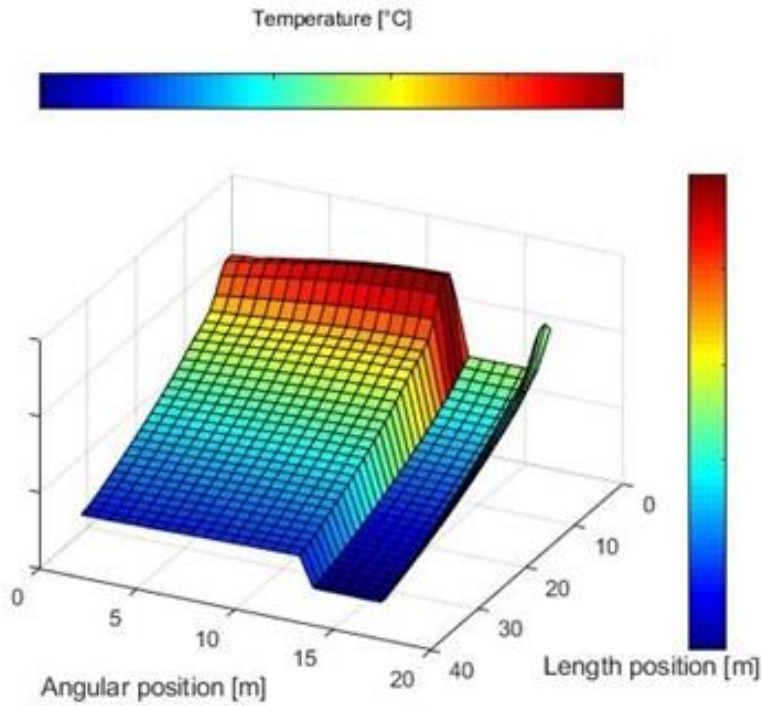

Figure 4.12: The bed and wall temperature profile for a 3.4m hydrogen flame with 16% added IOD particles, based on optical properties from [26].

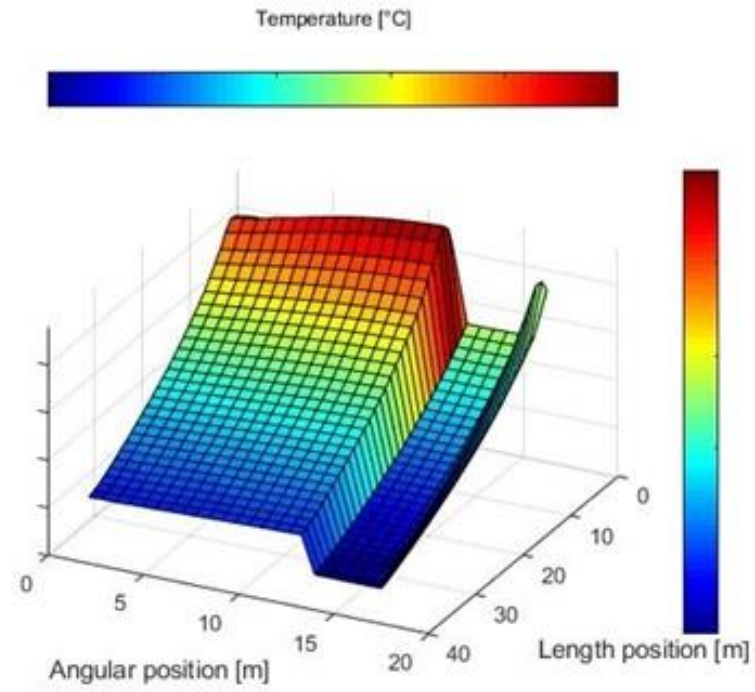

Figure 4.13: The bed and wall temperature profile for a 5.4m hydrogen flame with 7% added IOD particles, based on optical properties from [26].

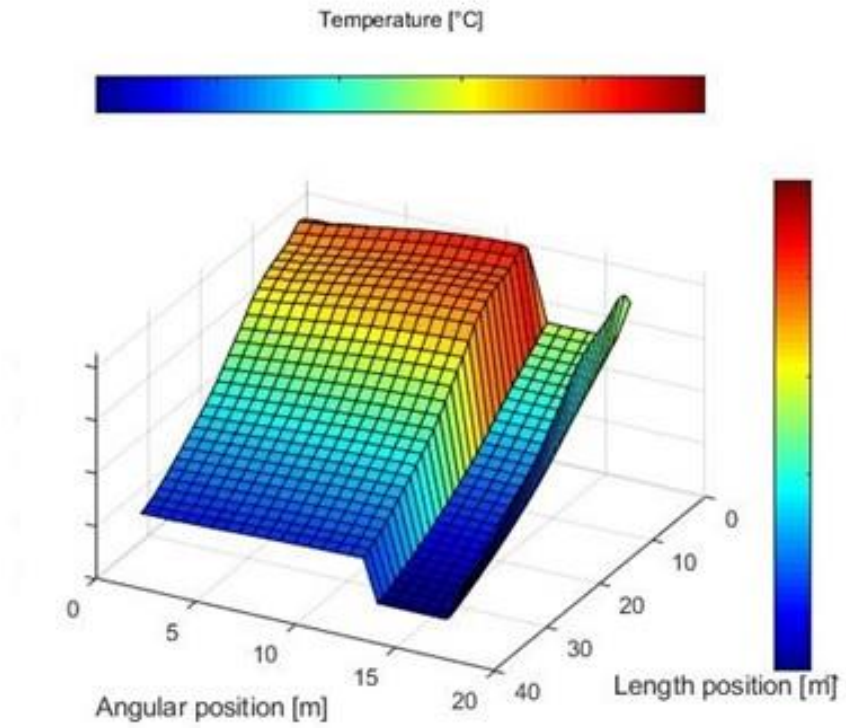

Figure 4.14: The bed and wall temperature profile for a 11.4m hydrogen flame with 3% added IOD particles, based on optical properties from [26].

The results of adding particles to the flame show an alternative to solve the energy balance using the reference settings. By adding particles, the radiation to the bed increases, and due to the high flame temperatures, only 7% coal particles were needed in a 5.4m hydrogen flame. In conclusion, the particles will absorb and emit radiation, i.e., accumulate heat from the flame, and release some of that heat to the bed material as the particles travel in the kiln. This enhances the radiative heat transfer and as energy from the flame is absorbed local peak temperatures in the kiln may be reduced, as well as extending the heat transfer load to the bed material through emittance. It can be noted that the maximum kiln wall temperature resulted with the 7% coal particle case at approximately 1490℃, while a maximum kiln wall temperature between 1300℃ -1370℃ was obtained from the sensitivity analyses of the temperature study. The results of the bed and wall temperature profiles show that the added particles transfer some of the accumulated heat from the flame, where the temperatures are highest, which increases the heat transfer to the kiln wall closer to the flame. This results in an uneven wall temperature profile seen in Figures 4.9, 4.10, 4.11, 4.12, 4.13, and 4.14 compared to the profiles shown from the temperature study seen in Figures 4.4, 4.5, 4.6, and 4.7. The results further show that increasing the flame length produces a more even wall temperature profile, as shown in Figures 4.9, 4.10, 4.11, 4.12, 4.13, and 4.14. This may be explained with the theory described in Section 2.4. As the flame length increases, the length of the highly radiating part of the flame, where the emittance from radiation dominate compared to other heat transfer mechanisms, increases as well, thus promoting radiative heat transfer to the bed material. Furthermore, some of the particles also transfer some of the accumulated heat as they travel further in the kiln, thus increasing the wall temperature further down the kiln as well. From the energy diagrams between the particle study and the temperature study, Figure 4.8 and Figure 4.3, it may also be noted how the heat transfer due to radiation increases in both cases, while the convective heat transfer is not affected in the particle study.

The cases of adding iron ore dust particles to the hydrogen flame show, that the heat transfer model yielded a non-repetitive result based on the different references used to obtain the optical properties of iron ore dust. However, it can be concluded that in order to solve the energy balance 7% and 8% particles were needed in a 5.4m hydrogen flame, according to [26], [27], respectively. These references also yielded similar radiative heat transfer to the bed material, as with the case of a 5.4m hydrogen flame with 8% coal particles, but resulted in different bed temperatures exiting the kiln. Thus, it can be concluded that while similar particle concentrations were needed for iron ore dust as for coal, the optical properties of particles do have an impact on the bed temperature exiting the kiln. The coal particles may emit radiation more effectively than the iron ore dust particles studied, thus obtaining a higher bed temperature. Furthermore, using the optical properties of ash with hematite [28], resulted that a higher concentration of particles being needed to solve the energy balance. Using the simulated optical properties [29], yielded that the energy balance could not be solved. Thus, more research on the optical properties, which are to be used as iron ore dust particles in a hydrogen flame is required, as some of the sources may over- or underestimate the properties needed to obtain accurate results.

In conclusion, by adding particles, heat transfer through particle radiation is included, increasing the radiative heat transfer, leading to higher temperatures in the bed material and surrounding kiln wall. Increasing the kiln wall temperature influences the surface radiation from the wall to the bed material, which also increases the conductive heat transfer from the wall to the bed. As a result, the bed temperature exiting the kiln increases, as more energy is transferred from the flame to the bed material. By adding different amounts of particles depending on the flame length the energy balance may be solved with the reference settings. Note that a small portion of particles was needed to solve the energy balance, which may be explained by the high flame temperatures from combusting hydrogen gas compared to coal and oil. As mentioned in Section 2.4, combusting hydrogen gas may produce a warmer flue gas compared to coal due to the lesser heat transfer from radiation, which accumulates heat from the flame and transfers that heat to the surroundings. For a hydrogen flame, such an extreme environment with elevated temperatures causes the particles to absorb and emit significantly more thermal radiation. The explanation may be simplified with black-body radiation, where the radiative energy flux is a function of a black body’s surface temperature at thermal equilibrium, see Equation 2.1.

Increasing the flame length increases the length of the radiative part of the flame, which influences the radiative heat transfer to the bed material. This may explain why an 11.4m hydrogen flame required fewer particles than a 5.4m hydrogen flame. In summary, the studied cases in this section may show the influence of including particle radiation in a 3.4m, 5.4m, and 11.4m hydrogen flame. If the implementation of particles is to achieve a zero-emission flame in the grate-kiln process, it may be possible to examine the addition of biomass particles, instead of coal. Adding iron ore dust may also be an alternative as shown in the results. These alternatives do, however, require more research if trustworthy results are to be achieved.

4.2 Results from Coal Cases

This section presents the results from the coal studies, which includes the effect of different flame lengths, dissociation and the addition of hydrogen to the coal flame.

4.2.1 Coal: Flame dimensions and Dissociation case

Table 4.6 describes the results from studying an 11.4m and 21.8m coal flame as well as a case that includes dissociation. Note that the bed and wall temperature profiles for an 11.4m and 21.8m coal flame are also included in this section, Figure 4.15 and Figure 4.16.

Table 4.6: The studied constant parameters (extra bold) and the results of the heat transfer model (listed as calculated parameters) from the coal, flame length study.

Constant Parameters	**Unit**	**Case: Coal 11.4m.**	**Case: Coal 21.8m.**	**Case: Coal 11.4m. Dissociation**
Bed temperature in	(°C)	1000	1000	1000
Gas temperature from cooler	(°C)	1200	1200	1200
Gas temperature to the PH-zone	(°C)	1300	**1230**	1300
Particles in flame	(%)	100	100	100
Thermal power from fuel	(MW)	35	35	35
Calculated Parameters	**Unit**	**Case: Coal 11.4m.**	**Case: Coal 21.8m.**	**Case: Coal 11.4m. Dissociation**
Bed temperature out	(°C)	1266	1299	1248
Max. Calculated adiabatic flame temp	(°C)	1897	1897	1823
Max. Kiln wall temperature	(°C)	1391	1398	1363
Radiation to bed	(MW)	24.1	29.4	21.8
Convection to bed	(MW)	2.4	1.1	2.4
Conduction to bed	(MW)	1.2	1.4	1.1
Total heat to gas	(MW)	6.1	2.3	6.2
Outer heat losses	(MW)	0.85	0.89	0.84
Total heat to bed	(MW)	27.7	31.9	25.2
Sum of all heat transferred in kiln:	(MW)	34.6	35.1	32.3

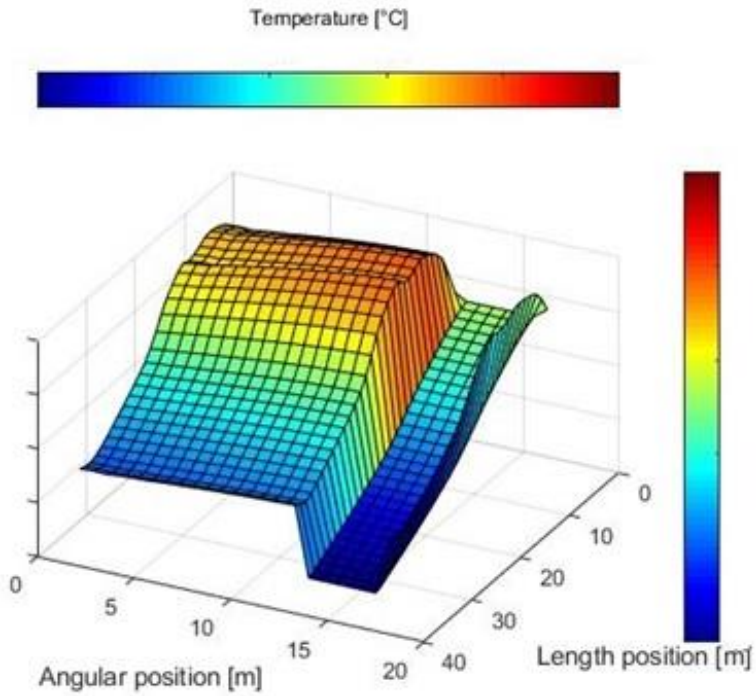

Figure 4.15: The bed and wall temperature profile for a 11.4m coal flame with the reference settings.

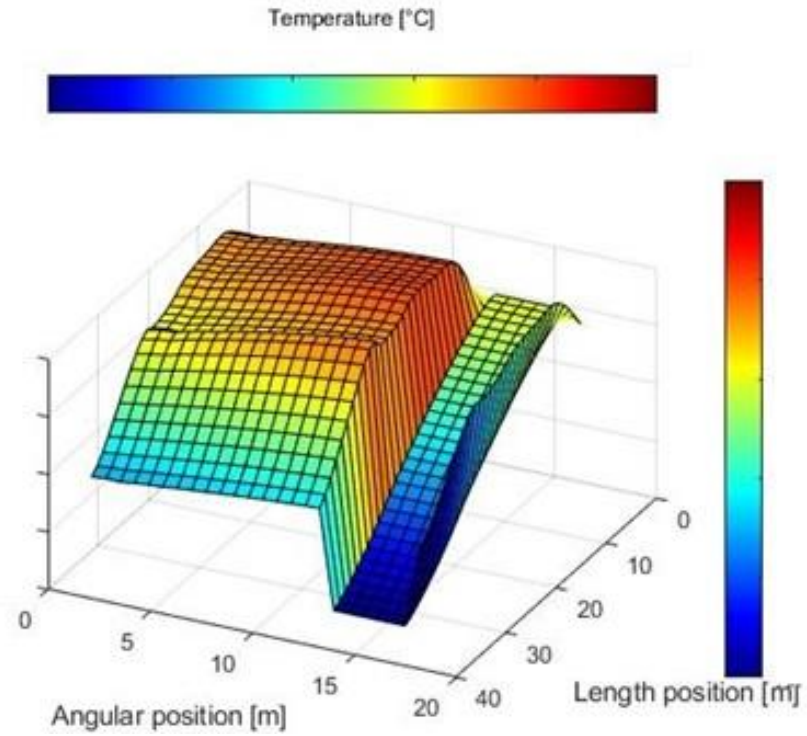

Figure 4.16: The bed and wall temperature profile for a 21.8m coal flame with a 1230°C gas temperature to the PH-zone.

It can be concluded from the results of the coal cases that by increasing the flame length the particle concentration and the length of the radiative part of the flame, increase. The increase in particle concentration is shown in the data input, Appendix B. As the particle concentration increases, the energy flux from radiation increases, which influences the wall and pellet bed temperature. This also affects the surface radiation and the conductive heat transfer to the bed material, increasing the temperature of the bed exiting the kiln. This also meant that the gas temperature to the PH-zone had to be decreased in order to solve the energy balance. As mentioned, decreasing the temperature to the PH-zone influences the parameters, total heat to gas, radiation, convection, and conduction to the bed. Note that including dissociation resulted in an unsolved energy balance due to a lesser heat transfer due to radiation, mainly since the flame temperature decreases. The energy balance can, however, be solved with dissociation by increasing the gas temperature to the PH-zone. Furthermore, the concentration of CO_2 decreases with dissociation leading to an increased concentration of H_2O, but has a small effect on influencing the radiative heat transfer. In conclusion, increasing the flame length increases the particle concentration as well as the length of the radiative part of the flame, which influences the radiative heat transfer to the bed material. Furthermore, the enhanced absorption and emittance of radiation from a higher particle concentration may explain the bed and wall temperature profiles shown in Figures 4.15 and 4.16.

4.2.2 Coal: Flame Composition case

The results from the study of adding hydrogen to the coal flame are presented in Table 4.7. Note that an energy diagram over the heat sources, heat sinks, and calculated radiation, convection, conduction in the kiln, is presented for an 11.4m coal flame with 10% added hydrogen as well, Figure 4.17. Since the bed and wall temperature profiles did not change significantly, the profile for one of the cases is shown, in Figure 4.18. Figure 4.18 illustrates a similar profile as seen in Figure 4.15, where an even heat transfer load to the bed material is obtained in comparison to the profiles seen for the hydrogen cases.

Table 4.7: The studied constant parameters (extra bold) and the results of the heat transfer model (listed as calculated parameters) from the coal flames, adding hydrogen study.

Constant Parameters	**Unit**	**Case: Coal 11.4m**	**Case: Coal 11.4m**	**Case: Coal 11.4m**
Bed temperature in	(°C)	1000	1000	1000
Gas temperature from cooler	(°C)	1200	1200	1200
Gas temperature to the PH-zone	(°C)	**1270**	**1260**	**1240**
Particles in flame	(%)	**90**	**85**	**80**
Hydrogen added in flame	(%)	**10**	**15**	**20**
Thermal power from fuel	(MW)	35	35	35
Calculated Parameters	**Unit**	**Case: Coal 11.4m**	**Case: Coal 11.4m**	**Case: Coal 11.4m**
Bed temperature out	(°C)	1250	1255	1259
Max. Calculated adiabatic flame temp	(°C)	1957	1988	2022
Max. Kiln wall temperature	(°C)	1390	1400	1411
Radiation to bed	(MW)	25.6	26.3	27
Convection to bed	(MW)	2.9	2.9	2.8
Conduction to bed	(MW)	1.2	1.3	1.3
Total heat to gas	(MW)	4.5	4	2.8
Outer heat losses	(MW)	0.95	0.96	0.96
Total heat to bed	(MW)	29.8	30.5	31.1
Sum of all heat transferred in kiln:	(MW)	35.2	35.4	34.9

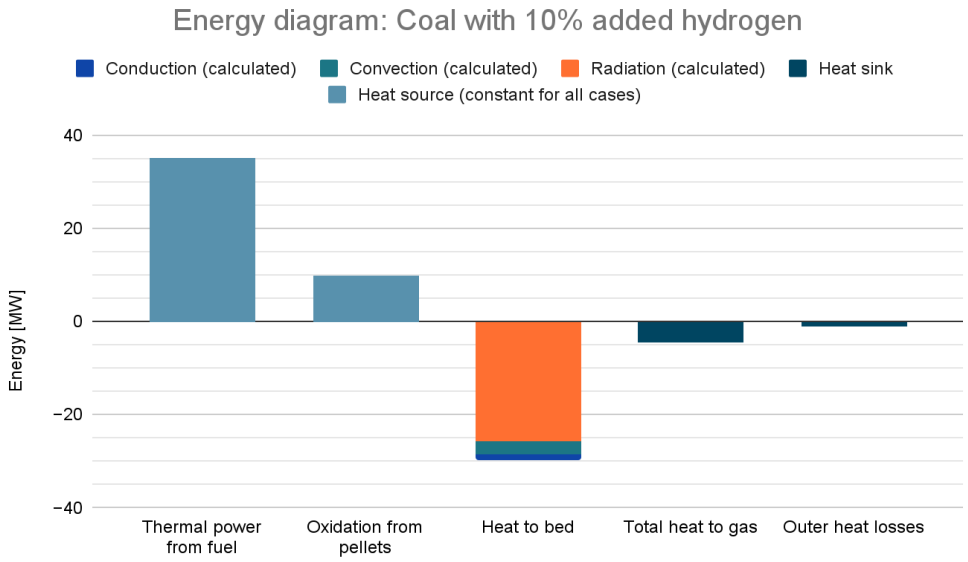

Figure 4.17: The heat sources, heat sinks as well as the calculated radiation, convection, and conduction in the kiln for a 11.4m coal flame with 10% added hydrogen.

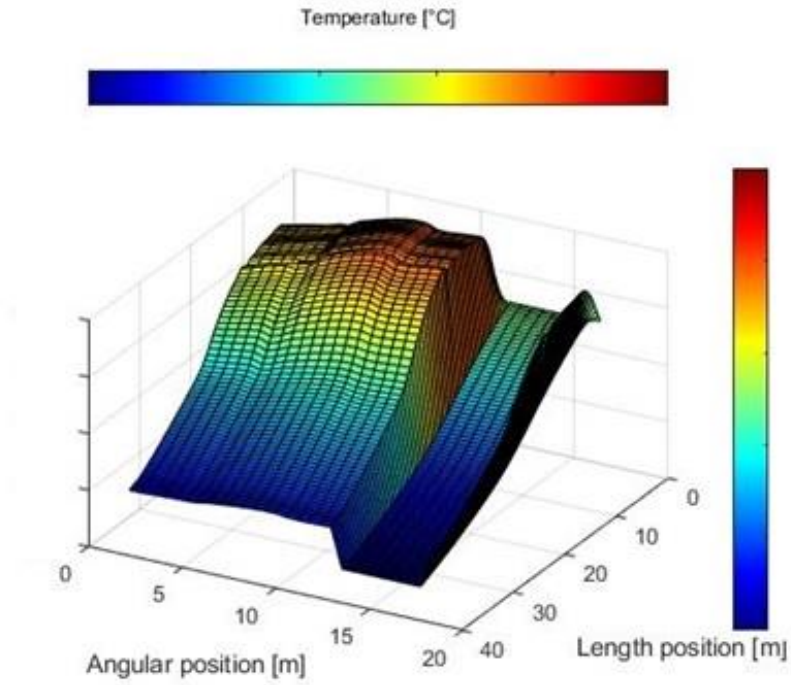

Figure 4.18: The bed and wall temperature profile for a 11.4m coal flame with 10% added hydrogen gas to the flame.

The results of adding H_2 to the coal flame yielded that an amount of added H_2 increased the adiabatic flame temperature. This is due to the added reaction heat from H_2 combustion, which is higher than the heating value from coal combustion. As mentioned in Section 4.1.3, a higher flame temperature has a significant impact on the particles that absorb and emit heat, thus increasing the heat transfer due to radiation. Furthermore, to solve the energy balance, the gas temperature to the PH-zone had to be decreased since the increase in flame temperature is not equally reduced with the decrease of particle concentration. Thus, the reduced heat transfer from the lesser particle concentration in the flame is less than the heat transfer gained by increasing the flame temperatures. The results also show that the increase in added H_2 increases the wall temperatures in the kiln. With 15% and 20% added H_2 to the coal flame, the results showed that the energy balance could be solved by further decreasing the gas temperature to the PH-zone. By adding more H_2 to the coal flame, the flame temperatures increase further, resulting in a greater heat transfer from particle radiation, causing a further increase of the wall temperatures. This influences the heat transfer from surface radiation and conduction from the wall to the bed material. However, since this meant that the gas temperature to the PH-zone had to be decreased, the total heat to gas decreased, which also decreases the heat transfer due to convection, radiation, and conduction. This ultimately results in bed temperatures exiting the kiln around 1250°C for the three cases. It can also be concluded from the gas concentrations in the data input listed in Appendix B, that increasing the added hydrogen, reduces the vol% of CO_2, but increases the vol% of H_2O, produced from combustion. Thus, by co-combusting coal with hydrogen, one may achieve a bed temperature exiting the kiln at a desired level and reduce CO_2 emissions, in consequence of increasing the gas concentration of H_2O and wall temperatures.

4.3 Results from Oil Cases

This section presents the results from the oil studies, which include an 11.4m and 21.8m oil flame as well as a case that includes dissociation. The results from the heat transfer model are listed in Table 4.8. The bed and wall temperatures for an 11.4m and 21.8m oil flame and an energy diagram for an 11.4m oil flame, are also presented in this section, see Figures 4.19, 4.20, and 4.21.

Table 4.8: The studied constant parameters (extra bold) and the results of the heat transfer model (listed as calculated parameters) from the oil, flame length study.

Constant Parameters	**Unit**	**Case: Oil 11.4m.**	**Case: Oil 21.8m.**	**Case: Oil 11.4m. Dissociation.**
Bed temperature in	(°C)	1000	1000	1000
Gas temperature from cooler	(°C)	1200	1200	1200
Gas temperature to the PH-zone	(°C)	**1370**	**1320**	**1370**
Particles in flame	(%)	100	100	100
Thermal power from fuel	(MW)	35	35	35
Calculated Parameters	**Unit**	**Case: Oil 11.4m.**	**Case: Oil 21.8m.**	**Case: Oil 11.4m. Dissociation.**
Bed temperature out	(°C)	1251	1270	1231
Max. Calculated adiabatic flame temp	(°C)	1912	1912	1751
Max. Kiln wall temperature	(°C)	1355	1366	1321
Radiation to bed	(MW)	20.9	24.9	18.4
Convection to bed	(MW)	3	1.3	2.9
Conduction to bed	(MW)	1	1.2	0.92
Total heat to gas	(MW)	9.7	7.1	9.6
Outer heat losses	(MW)	0.95	0.99	0.93
Total heat to bed	(MW)	24.9	27.2	22.2
Sum of all heat transferred in kiln:	(MW)	35.5	35.4	32.8

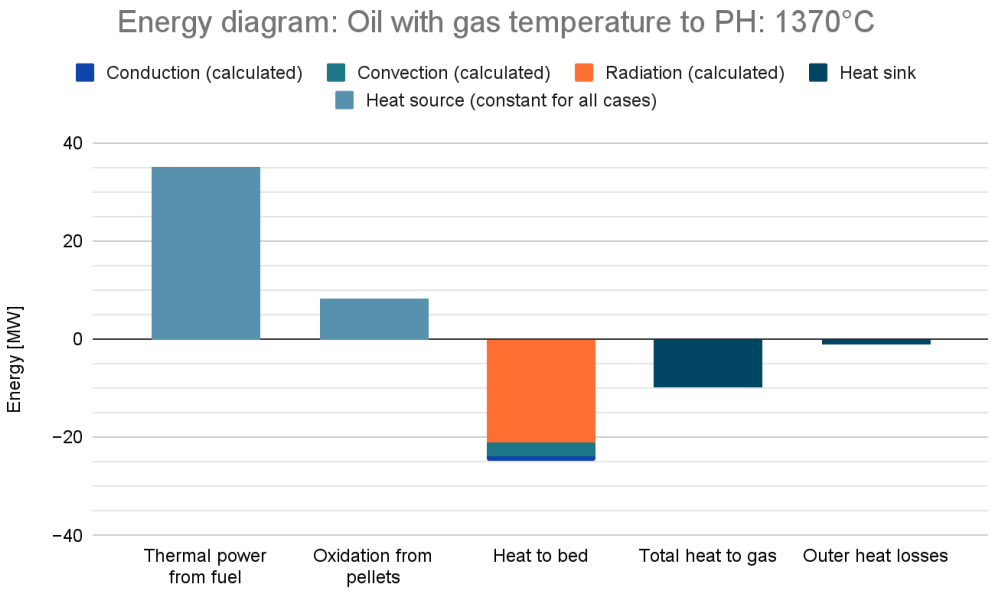

Figure 4.19: The heat sources, heat sinks as well as the calculated radiation, convection, and conduction in the kiln for a 11.4m oil flame with a gas temperature of 1370°C to the PH-zone.

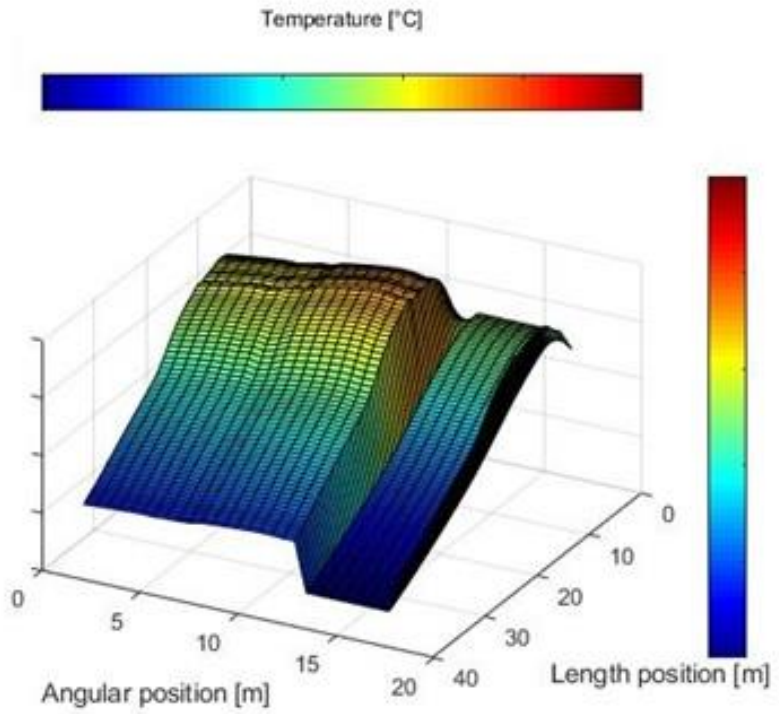

Figure 4.20: The bed and wall temperature profile for a 11.4m oil flame with a gas temperature of 1370°C to the PH-zone.

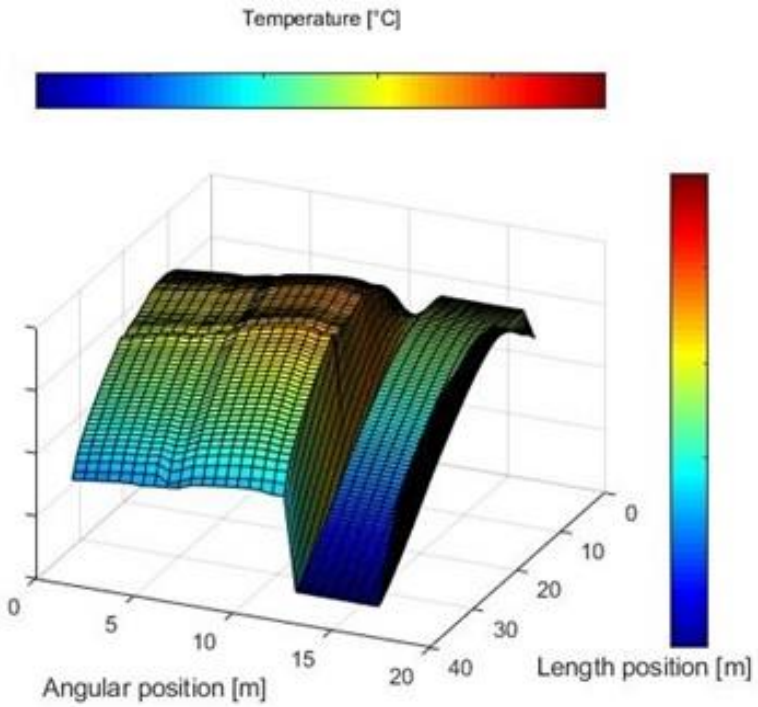

Figure 4.21: The bed and wall temperature profile for a 21.8m oil flame with a gas temperature of 1320°C to the PH-zone.

By increasing the flame length, a higher particle concentration is achieved, thus increasing the heat transfer due to radiation. This resulted in the gas temperature to the PH-zone having to be decreased in order to solve the energy balance. This affects the heat transfer due to radiation, convection, and conduction and reduces the parameter, total heat to gas. Furthermore, as mentioned in Section 2.4, an even heat load to the pellet bed is preferable in order to reach the desired degree of oxidation and quality of the pellets. As shown in the bed and wall temperatures, Figures 4.16 and 4.21 an even bed and wall temperature profile are achieved for a 21.8m coal and oil flame. As concluded in Section 4.2.1, increasing the flame length generates a higher particle concentration and increases the length of the radiative part of the flame where radiation dominates. Thus, the effects from the particles that absorb and emit radiation as they travel in the kiln become greater, extending the heat transfer in the kiln. This may explain the resulted bed and wall temperature profile for a 21.8m coal and oil flame seen in Figures 4.16 and 4.21. In the data input of the particle and soot concentrations of the coal and oil flames, listed in Appendix B, it can be noted that the coal flames include a higher concentration of particles than the oil flames, while the amount of soot particles is the same for both cases. This may explain why an 11.4m oil flame required a higher gas temperature to the PH-zone than an 11.4m coal flame in order to solve the energy balance.

4.4 Compilation: Selection of cases

Figure 4.22 describes the bed temperature exiting the kiln for a selection of the cases. The figure also presents the preferred cases if the desired temperature exiting the kiln is to mimic that of a coal or oil flame, see the green and black lines in Figure 4.22. As seen in Figure 4.22 to reach the same bed temperature as an 11.4m oil flame with a gas temperature of 1370°C to the PH-zone, a 5.4m hydrogen flame requires a gas temperature of 1300°C from the cooler and should hold a temperature of 1440°C to the PH-zone. Alternatively, the overall gas temperature in the kiln can be increased by 8%. For an 11.4m coal flame to reach the same bed temperature, 10% (based on heat load) of the coal fuel may be exchanged for hydrogen, with a gas temperature of 1270°C to the PH-zone. In summary, for a hydrogen flame to mimic the bed temperature exiting the kiln as that of an oil flame it may be concluded that influencing the gas temperatures is more preferable than influencing the flame by adding particles. This is seen by the green line in Figure 4.22. Furthermore, if a bed temperature exiting the kiln similar to an 11.4m coal flame with the reference settings is desired for a hydrogen flame. Then it may be concluded that influencing the flame by adding particles is a more preferable option than increasing the gas temperatures, as seen by the black line in Figure 4.22.

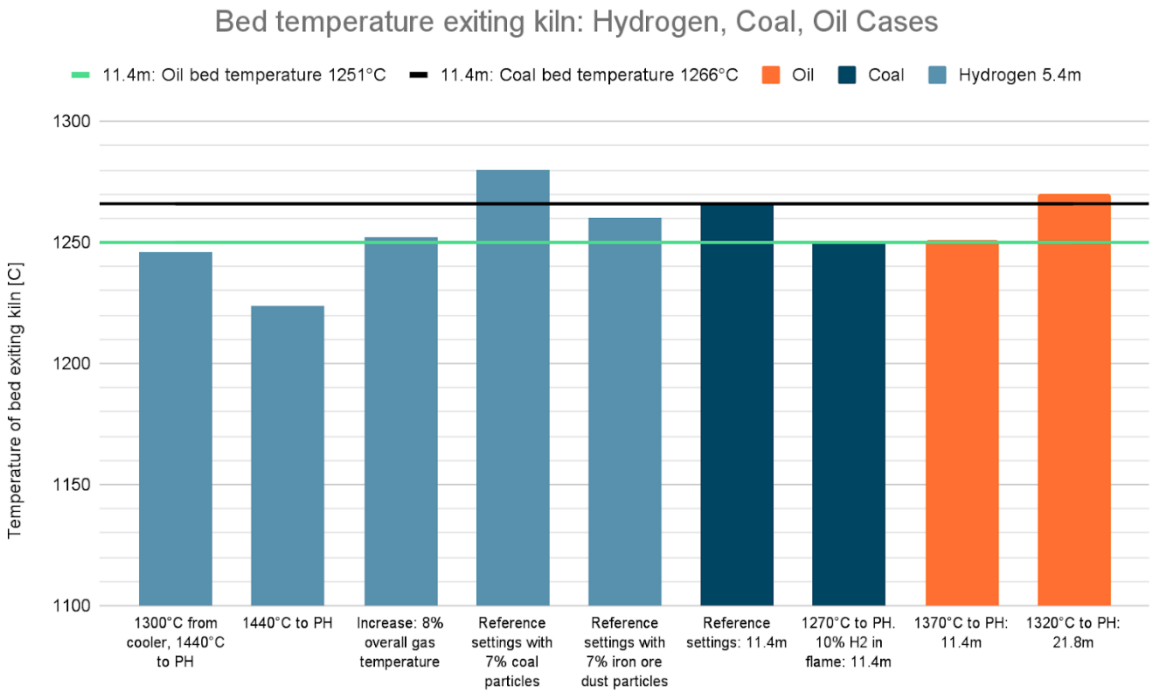

Figure 4.22: The resulting parameter, bed temperature exting the kiln, for a selection of cases. Lines that illustrate a desired bed temperature similar to a coal or oil flame are also included.

Figure 4.23 describes the resulting maximum kiln wall temperature for the same selection of cases as shown in Figure 4.22. Figure 4.23 further illustrates the calculated maximum kiln wall temperature for an 11.4m coal and oil flame by a black and green line, respectively. It may be concluded from, Figure 4.23 and from the respective bed and wall temperature profiles, see Figures 4.10 and 4.13, that the wall temperature is largely affected by adding particles to a hydrogen flame. The elevated wall temperatures may impose larger stresses on the kiln, which may not be favorable. Figure 4.23 further shows that the maximum kiln wall temperature for a 5.4m hydrogen flame with a gas temperature of 1300°C from the cooler and 1440°C to the PH-zone is less than the respective oil and coal flames.

Furthermore, when comparing the bed and wall temperature profiles from the coal and oil cases, see Figures 4.15, 4.18, 4.20, and 4.21 with the hydrogen cases, see Figures 4.4, 4.6, 4.7, 4.10, and 4.13, it may be concluded that the hydrogen flames do not mimic a similar and desired moderate long heat profile. In conclusion, in order to evaluate if the preferable cases derived from the desired bed temperatures exiting the kiln is a favorable option, more research on how the kiln wall temperature and how the resulting heat load affects the kiln and pellet bed is required.

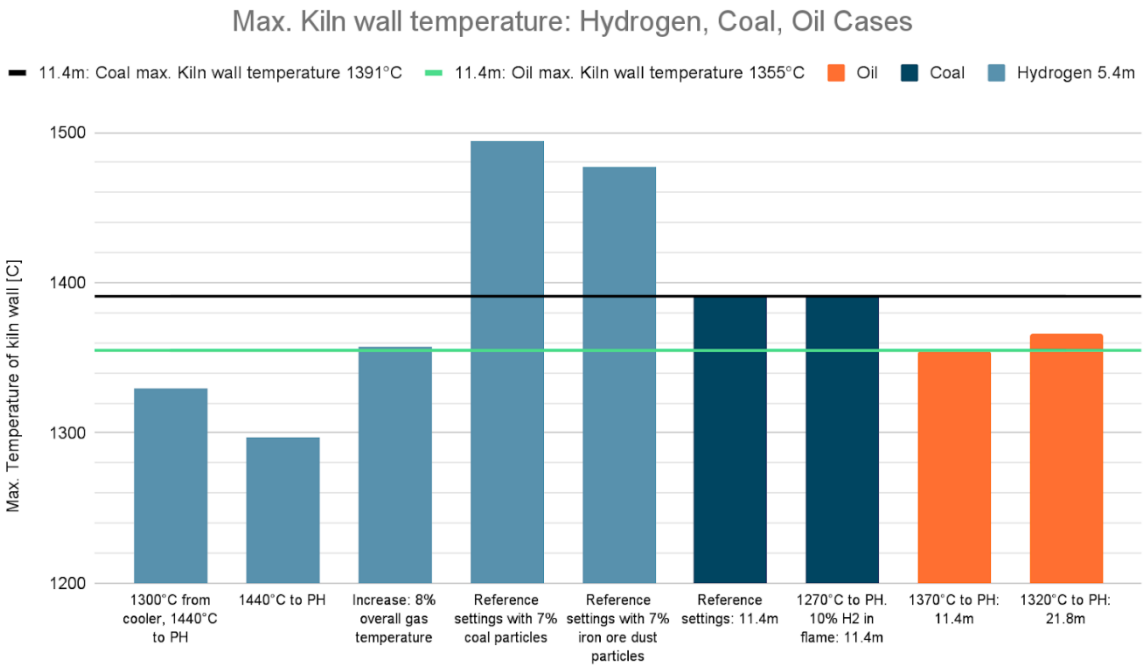

Figure 4.23: The resulting parameter, max. kiln wall temperature, for a selection of cases. Lines that illustrate a desired, max. Kiln wall temperature similar to a coal or oil flame are also included.

5.

Conclusions

In this master thesis work, the heat transfer conditions within a rotary kiln have been analyzed by implementing a hydrogen flame in a heat transfer model in order to find possible options to reduce LKAB's carbon dioxide emissions. The results indicate that it is possible to reach similar heat transfer conditions to the bed material in a rotary kiln for iron ore pellets production, substituting the fossil fuel flames for hydrogen gas. That is, a similar bed temperature exiting the kiln with a hydrogen flame as that of a coal or oil flame appears to be possible. This does, however, require the addition of particles to the flame or an increased gas temperature from the cooler.

The results presented in this master thesis are based on rather extreme conditions for the flames inside the kiln, using hydrogen, coal, or oil as fuels. The flame temperatures assume that of the respective adiabatic flame temperature profiles with various excess of air. From the studies conducted in this master thesis work it can be concluded that, for a hydrogen flame to acquire a bed temperature similar to an oil flame, it would be beneficial to increase the gas temperatures from the cooler section. If a hydrogen flame is to achieve a similar bed temperature exiting the kiln as that of the studied coal flame, influencing the flame by adding coal particles seems to be beneficial. Only a small portion of particles seems to have substantial effects on the heat transfer conditions. However, further research on the impact of influencing either the gas temperature from the cooler or the particle load in the flame is recommended, in order to achieve accurate results.

From the different particles studied in this work, it can be concluded that coal particles in a hydrogen flame seem to have a larger impact on the heat transfer conditions than iron ore dust. To correctly capture the effects on the heat transfer conditions when adding iron ore dust, further research on which optical properties to use is recommended. Another recommendation when studying particles is also to study the effects of the particle size distribution. The effects of dissociation have an impact on the results, which lead to an unsolved energy balance. Since such effects are expected at flame temperatures it should be included to capture the flame temperature profile and further research in this area is recommended as well.

Furthermore, the derived solutions do not provide an even heat transfer load to the pellet bed, if compared with the coal and oil flames. The solutions may also complicate how the kiln should be operated in the grate-kiln process, in order to ensure the desired pellets quality. The resulting kiln wall temperature of the derived solutions may also affect the heat losses and stresses imposed on the kiln during operation. Ultimately, the results and derived solutions may be used for evaluating the implementation of a hydrogen flame in a rotary kiln.

5.1 Recommendations for future work

For future work, the model could be further developed by implementing a more accurate mixing function of air to the flame used as a data input of the temperature profile with the heat transfer model. One example could be to use a temperature profile based on measurements instead of using the adiabatic flame temperatures. Different types of flame shapes could also be investigated and how this affects the heat transfer from the flame to the bed material. As the energy balance over the kiln is in this master thesis work limited by a constant bed temperature entering the kiln, degree of oxidation, and thermal power from the fuel, these parameters could also be studied in sensitivity analyses. The energy balance could also be extended in order to include the whole process, i.e., the grate and the cooler as well. This would allow for examining the effects of increasing the gas temperatures more carefully and how this affects the whole process. Furthermore, investigating the effects of implementing biomass particles in order to substitute the coal particles added to a hydrogen flame, is also recommended for future work. Finally, in terms of experimental work, a recommendation is to investigate the coal with added hydrogen case as a possible co-combustion alternative in the kiln, which may be a first step towards transitioning to hydrogen combustion.

References

[1] Sveriges klimatmål och klimatpolitiska ramverk [Internet]. [Cited 2022-01-27]. Available from: https://www.naturvardsverket.se/amnesomraden/klimatomstallningen/sveriges-klimatarbete/sveriges-klimatmal-och-klimatpolitiska-ramverk/

[2] Klimatomställning som skapar möjligheter [Internet]. [Cited 2022-01-25]. Available from: https://www.lkab.com/sv/nyhetsrum/nyheter/klimatomstallning-som-skapar-mojligheter/

[3] LKAB i korthet [Internet]. [Cited 2022-01-19]. Available from: https://www.lkab.com/sv/om-lkab/lkab-i-korthet/

[4] HYBRIT – för fossilfritt stål [Internet]. [Cited 2022-01-19]. Available from: https://www.lkab.com/sv/om-lkab/teknik-och-processutveckling/forskningssamarbeten/hybrit--for-fossilfritt-stal/

[5] Fossilfri produktion av järnmalmspellets - Luleå tekniska universitet, LTU [Internet]. [Cited 2022-01-19]. Available from: https://www.ltu.se/research/subjects/Processmetallurgi/Nyheter/Fossilfri-produktion-av-jarnmalmspellets-1.202187

[6] HYBRIT – fossilfritt stål - SSAB [Internet]. [Cited 2022-01-19]. Available from: https://www.ssab.com/sv-se/produkter/varumarken/greencoat/sustainable-building-with-greencoat/hybrit-fossil-free-steel?gclid=Cj0KCQiAip-PBhDVARIsAPP2xc0jDOmvwzvUU_D_5i7vzYPCaGzgRw3p_HF6uqtCx2bIUDQJB5SksaEaAg3VEALw_wcB

[7] Lindén E, Thureborn E. Electrification of the heat treatment process for iron ore pelletization at LKAB. [Master thesis]. Gothenburg: Chalmers University of Technology; 2019 [Cited 2022-01-18].

[8] Från gruva till hamn [Internet]. [Cited 2022-01-20]. Available from: https://www.lkab.com/sv/om-lkab/fran-gruva-till-hamn/

[9] Haaf M. Thermodynamic process evaluation of a rotary kiln unit at LKAB Kiruna. [Master thesis]. Gothenburg: Chalmers University of Technology; 2014 [Cited 2022-01-20].

[10] Jonsson CYC, Stjernberg J, Wiinikka H, Lindblom B, Boström D, Öhman M. Deposit formation in a grate-kiln plant for iron-ore pellet production. Part 1: Characterization of process gas particles. Energy and Fuels. 2013;27(10):6159–70.

[11] Gunnarsson A, Andersson K, Adams BR, Fredriksson C. Full-scale 3D-modelling of the radiative heat transfer in rotary kilns with a present bed material. International Journal of Heat and Mass Transfer. 2020;147.

[12] Gunnarsson A, Andersson K, Adams BR, Fredriksson C. Discrete-ordinates modelling of the radiative heat transfer in a pilot-scale rotary kiln. Energies (Basel). 2020;13(9).

[13] Gunnarsson A, Chalmers tekniska högskola. Radiative heat transfer in suspension-fired systems. [Thesis for the degree of Doctor of Philosophy]. Gothenburg: Chalmers University of Technology; 2019 [Cited 2022-01-20].

[14] Derby JJ, Yeckel A. Heat Transfer Analysis and Design for Bulk Crystal Growth: Perspectives on the Bridgman Method. Handbook of Crystal Growth: Bulk Crystal Growth: Second Edition. 2015;2:793–843.

[15] What is Fourier's Law of Thermal Conduction - Definition [Internet]. [Cited 2022-05-20]. Available from: https://www.thermal-engineering.org/what-is-fouriers-law-of-thermal-conduction-definition/

[16] What is Forced Convection - Definition [Internet]. [Cited 2022-05-20]. Available from: https://www.thermal-engineering.org/what-is-forced-convection-definition/

[17] Wiinikka H, Sepman A, Ögren Y, Lindblom B, Nordin LO. Combustion Evaluation of Renewable Fuels for Iron-Ore Pellet Induration. Energy and Fuels. 2019;33(8):7819–29.

[18] Kim J, Yu J, Lee S, Tahmasebi A, Jeon CH, Lucas J. Advances in catalytic hydrogen combustion research: Catalysts, mechanism, kinetics, and reactor designs. International Journal of Hydrogen Energy. 2021;46(80):40073–104.

[19] Schefer RW, Houf WG, Bourne B, Colton J. Spatial and radiative properties of an open-flame hydrogen plume. International Journal of Hydrogen Energy. 2006;31(10):1332–40.

[20] Hutny WP, Lee GK. IMPROVED RADIATIVE HEAT TRANSFER FROM HYDROGEN FLAMES. Int J Hydrogen Energy. 1991; 16(1):47–53.

[21] Dean AM, Bozzelli JW. Combustion Chemistry of Nitrogen. Gas-Phase Combustion Chemistry. 2000;125–341.

[22] Bäckström D, Johansson R, Andersson K, Wiinikka H, Fredriksson C. On the use of alternative fuels in rotary kiln burners — An experimental and modelling study of the effect on the radiative heat transfer conditions. Fuel Processing Technology. 2015;138:210–20.

[23] Normann. F. Personal communication, 2022.

[24] El-Ghafour SAA, El-dein AHE, Aref AAR. Combustion characteristics of natural gas–hydrogen hybrid fuel turbulent diffusion flame. International Journal of Hydrogen Energy. 2010; 35(6):2556–65.

[25] Gunnarsson A, Bäckström D, Johansson R, Fredriksson C, Andersson K. Radiative Heat Transfer Conditions in a Rotary Kiln Test Furnace Using Coal, Biomass, and Cofiring Burners. Energy and Fuels. 2017 [Cited 2022-05-20];31(7):7482–92. Available from: https://pubs.acs.org/doi/pdf/10.1021/acs.energyfuels.7b00083

[26] Querry, M. R.: Optical Constants, Contractor report, US Army Chemical Research, Development and Engineering Center (CRDC), Aberdeen Proving Ground, MD, 418 pp., 1985.

[27] Goodwint DG, Mitchner M. Flyash radiative properties and effects on radiative heat transfer in coal-fired systems. Vol. 32, Inl. J. Hear Mass Transfer. 1989.

[28] Johansson R, Leckner B, Andersson K, Johnsson F. Influence of particle and gas radiation in oxy-fuel combustion. International Journal of Heat and Mass Transfer. 2013;65:143–52.

[29] Zhang XL, Wu GJ, Zhang CL, Xu TL, Zhou QQ. What is the real role of iron oxides in the optical properties of dust aerosols? Atmospheric Chemistry and Physics. 2015;15(21):12159–77.

[30] Thunman H. “Combustion Engineering”. Chalmers University of Technology, 2020.

[31] Gunnarsson. A. Personal communication, 2022.

[32] Eldningsolja 5. [Online]. Available from: https://www.preem.se/contentassets/f069cb7baec44171ac1d318e10e43f70/eldningsolja-504.pdf

Appendix A. Calculations of the adiabatic flame temperature

A.1 Adiabatic flame temperature: Hydrogen

The molar flow rate of hydrogen was determined from the thermal power of the fuel and the heat of reaction, according to Equation, A.1. Since the heat of formation of H_2, N_2 and O_2 is 0, the heat of reaction for hydrogen combustion is that of the heat of formation of H_2O(g), Equation A.2.

$$Thermal\ Power = \Delta h_{rxr} * n_{H2} \rightarrow n_{H2} = Thermal\ Power / \Delta h_{rxr} \quad (A.1)$$

$$\Delta h_{rxr} = -242174\ \frac{J}{moles\ H2} \quad (A.2)$$

The molar flow rates of each component were then determined accoring to Equations A.3, A.4 and A.5.

$$n_{O2} = \frac{1}{2} * n_{H2} \quad (A.3)$$

$$n_{N2} = n_{O2} * \left(\frac{79}{21}\right) \quad (A.4)$$

$$n_{H2O} = n_{H2} \quad (A.5)$$

Note that λ_{max} was calculated according to, Equations A.6, A.7, A.8 and A.9. The maximum molar flowrate of O_2 was determined using the volumetric flow rate of O_2 by, assuming 21% of O_2 in the air flow. Note that, P_{normal} and T_{normal} were equal to 1 bar and 0°C, respectively.

$$V_{O2} = V_{air} * 0.21 \quad (A.6)$$

$$m_{O2} = \frac{P_{normal} * V_{O2} * M_{O2}}{R * T_{normal}} \quad (A.7)$$

$$n_{O2,max} = m_{O2} / M_{O2} \quad (A.8)$$

The maximum available excess air ratio could be calculated according to Equation, A.9.

$$\lambda_{max} = \frac{n_{O2,max} * 2}{n_{H2}} \quad (A.9)$$

From the combustion reaction and the energy balance described in Section 3.2.1, the heat of formation was set up for both the reactants and products. For the reactants, this resulted in Equations A.10, A.11, A.12, and finally A.13. The components with index a and b in Equations A.10-A.12, A.14-A.16, A.40-A.47, A.53-A.58, are constants taken from [30] in order to calculate the specific heat capacity, see Equation 3.2.

$$Hf_{O2,R} = n_{O2} * \lambda * (\Delta Hf_{O2,298K} + [O_{2,a} * \left(T_{air,in} - T_{ref}\right) + \frac{O_{2,b}}{2} * \left(T_{air,in}^2 - T_{ref}^2\right)] \quad (A.10)$$

$$Hf_{N2,R} = n_{N2} * \lambda * (\Delta Hf_{N2,298K} + [N_{2,a} * \left(T_{air,in} - T_{ref}\right) + \frac{N_{2,b}}{2} * \left(T_{air,in}^2 - T_{ref}^2\right)] \quad (A.11)$$

A. Calculations of the adiabatc flame temperature

$$Hf_{H2,R} = n_{H2} * (\Delta Hf_{H2,298K} + [H_{2,a} * \left(T_{H2,in} - T_{ref}\right) + \frac{H_{2,b}}{2} * \left(T_{H2,in}^2 - T_{ref}^2\right)] \quad \text{(A.12)}$$

$$Hf_{reactants} = Hf_{H2,R} + Hf_{N2,R} + Hf_{O2,R} \quad \text{(A.13)}$$

For the products this resulted in Equations A.14, A.15, A.16 and A.17.

$$Hf_{H2O,P} = n_{H2O} * (\Delta Hf_{H2O,298K} + H_2O_{,a} * \left(T_{adiabatic} - T_{ref}\right) + \frac{H_2O_{,b}}{2} * \left(T_{adiabatic}^2 - T_{ref}^2\right)] \quad \text{(A.14)}$$

$$Hf_{N2,P} = n_{N2} * \lambda * (\Delta Hf_{N2,298K} + [N_{2,a} * \left(T_{adiabatic} - T_{ref}\right) + \frac{N_{2,b}}{2} * \left(T_{adiabatic}^2 - T_{ref}^2\right)] \quad \text{(A.15)}$$

$$Hf_{O2,P} = n_{O2} * (1 - \lambda) * (\Delta Hf_{O2,298K} + [O_{2,a} * \left(T_{adiabatic} - T_{ref}\right) + \frac{O_{2,b}}{2} * \left(T_{adiabatic}^2 - T_{ref}^2\right)] \quad \text{(A.16)}$$

$$Hf_{products} = Hf_{H2O,P} + Hf_{N2,P} + Hf_{O2,P} \quad \text{(A.17)}$$

In order to include the effect of dissociation, an equilibrium constant, Kp for the water split was introduced as Equation A.18 [30].

$$Kp = 855 * e^{-29840/T_{adiabatic}} \text{ [30]} \quad \text{(A.18)}$$

Where, Kp may also be defined according to Equation A.19.

$$Kp = \frac{P_{H2}^o * {P_{O2}^o}^{0.5}}{P_{H2O}^o} \quad \text{(A.19)}$$

The total pressure, P_{tot} was assumed as 1 atm and the gases were assumed as ideal gases, thus the partial pressure for each species was written in terms of molar fractions, Y, according to Equation, A.20. This resulted in that Equation A.19 was re-written as Equation A.21.

$$P_i^o = Y_i * P_{tot} \quad \text{(A.20)}$$

$$Kp = \frac{Y_{H2} * {Y_{O2}}^{0.5}}{Y_{H2O}} = 855 * e^{-29840/T_{adiabatic}} \quad \text{(A.21)}$$

The mole fraction of each specie was defined as the molar flow of the specie, i divided by the total molar flow rate, according to Equation A.22. Note that since the adiabatic temperature of the flame is dependent on the molar flows of each specie the total molar flow rate and the equilibrium constant, Kp are dependent on the molar flows in the product gas mix.

$$Y_i = \frac{n_i}{n_{tot}} \quad \text{(A.22)}$$

Thus, each molar flow rate in the product gas mix was written as Equations A.23, A.24, A.25, A.26 and A.27. Note that the subscript d, is the amount of moles/s that are dissipated.

$$n_{H2O} = n_{H2} - n_{H2,d} \quad \text{(A.23)}$$

$$n_{O2,d} = 0.5 * n_{H2,d} \quad \text{(A.24)}$$

$$n_{N2} = 0.5 * n_{H2} * \lambda * \left(\frac{79}{21}\right) \quad \text{(A.25)}$$
$$n_{O2} = 0.5 * n_{H2} * (\lambda - 1) + n_{O2,d} \quad \text{(A.26)}$$
$$n_{tot} = n_{H2O} + n_{O2,d} + n_{N2} + n_{O2} + n_{H2,d} \quad \text{(A.27)}$$

To solve the systems of equations, Equations A.22-A.27, an iterative procedure by, guessing $n_{H2,d}$ until Equation A.21 was satisfied for the corresponding guessed adiabatic flame temperature, $T_{adiabatic}$, was carried out in MatLab.

A.2 Adiabatic flame temperature: Coal & Oil

In order to determine the maximum excess air ratio from Equation A.28, the molar flowrate of the fuel is required. Note that the molar flowrate of oxygen is determined from the air flow to the kiln, which is calculated in Appendix A.1. The molar flowrate of the fuel was calculated according to Equation A.29, where the molar mass and the massflow of the fuel was determined according to Equation A.30 and Equation A.31. To simplify the calculations from the ash contribution, ash was assumed as SiO_2.

$$\lambda_{max} = \frac{n_{O2,max}}{n_{fuel}} \quad \text{(A.28)}$$

$$n_{fuel} = \frac{m_{fuel}}{M_{fuel}} \quad \text{(A.29)}$$

$$M_{fuel} = moist * M_{H2O} + ash * M_{SiO2} + C * M_C + \frac{H}{2} * M_{H2} + \frac{N}{2} * M_{N2} + \frac{O}{2} * M_{O2} + S * M_S \quad \text{(A.30)}$$

$$m_{fuel} = \frac{Thermal\ power\ from\ fuel}{lower\ heating\ value} \quad \text{(A.31)}$$

The molar flow rates of each reactant component were then determined according to Equations A.32, A.33, A.34, A.35, A.36, A.37 and A.38.

$$n_{moist} = \frac{1}{moist * M_{H2O}} * m_{fuel} \quad \text{(A.32)}$$
$$n_{ash} = \frac{1}{ash * M_{SiO2}} * m_{fuel} \quad \text{(A.33)}$$
$$n_C = \frac{1}{C * M_C} * m_{fuel} \quad \text{(A.34)}$$
$$n_{H2} = \frac{1}{\frac{H}{2} * M_{H2}} * m_{fuel} \quad \text{(A.35)}$$
$$n_{N2} = \frac{1}{\frac{N}{2} * M_{N2}} * m_{fuel} \quad \text{(A.36)}$$
$$n_{O2} = \frac{1}{\frac{O}{2} * M_{O2}} * m_{fuel} \quad \text{(A.37)}$$
$$n_S = \frac{1}{S * M_S} * m_{fuel} \quad \text{(A.38)}$$

Where, the required amount of O_2 for the combustion to occur was determined according to Equation A.39.

$$n_{O2,req} = n_C + \frac{1}{2} n_{H2} + n_S - n_{O2} \quad \text{(A.39)}$$

Thus, the heat of formation for the reactants were defined according to Equations A.40, A.41, A.42, A.43, A.44, A.45, A.46, A.47.

$$Hf_{O2,R} = n_{O2,req} * 0.5 * \lambda * (\Delta Hf_{O2,298K} + [O_{2,a} * (T_{air,in} - T_{ref}) + \frac{O_{2,b}}{2} * (T_{air,in}^2 - T_{ref}^2)] \quad (A.40)$$

$$Hf_{N2,R} = (n_{O2,req} * \frac{79}{21} * \lambda - n_{N2}) * (\Delta Hf_{N2,298K} + [N_{2,a} * (T_{air,in} - T_{ref}) + \frac{N_{2,b}}{2} * (T_{air,in}^2 - T_{ref}^2) \quad (A.41)$$

$$Hf_{C,R} = n_C * (\Delta Hf_{C,298K} + [C_{,a} * (T_{in} - T_{ref}) + \frac{C_{,b}}{2} * (T_{in}^2 - T_{ref}^2)] \quad (A.42)$$

$$Hf_{H2O,R} = n_{moist} * (\Delta Hf_{H2O(l),298K} + [H_2O(l)_{.a} * (T_{in} - T_{ref}) + \frac{H_2O(l)_{.b}}{2} * (T_{in}^2 - T_{ref}^2)] \quad (A.43)$$

$$Hf_{H2,R} = n_{H2} * (\Delta Hf_{H2,298K} + [H_{2,a} * (T_{in} - T_{ref}) + \frac{H_{2,b}}{2} * (T_{in}^2 - T_{ref}^2)] \quad (A.44)$$

$$Hf_{N2,R} = n_{N2} * (\Delta Hf_{N2,298K} + [N_{2,a} * (T_{in} - T_{ref}) + \frac{N_{2,b}}{2} * (T_{in}^2 - T_{ref}^2)] \quad (A.45)$$

$$Hf_{S,R} = n_S * (\Delta Hf_{S,298K} + [S_{,a} * (T_{in} - T_{ref}) + \frac{S_{,b}}{2} * (T_{in}^2 - T_{ref}^2)] \quad (A.46)$$

$$Hf_{ash,R} = n_{ash} * (\Delta Hf_{SiO2,298K} + [SiO_{2,a} * (T_{in} - T_{ref}) + \frac{SiO_{2,b}}{2} * (T_{in}^2 - T_{ref}^2)] \quad (A.47)$$

Note that the heat of formation of N_2 is listed twice since it originates from both the fuel composition and the air flow which, may vary in temperature.

The molar flow rate of the produced combustion products were determined according to Equations A.48, A.49, A.50, A.51 and A.52.

$$n_{CO2} = n_C \quad (A.48)$$

$$n_{H2O} = n_{moist} + n_{H2} \quad (A.49)$$

$$n_{N2,p} = (n_{O2,req} * \frac{79}{21} * \lambda + n_{N2}) \quad (A.50)$$

$$n_{O2,p} = n_{O2,req} * (\lambda - 1) \quad (A.51)$$

$$n_{SO2} = n_S \quad (A.52)$$

This resulted in the heat of formation of the combustion products according to Equations A.53, A.54, A.55, A.56, A.57 and A.58.

$$Hf_{CO2,P} = n_{CO2} * (\Delta Hf_{CO2,298K} + [CO_{2,a} * (T_{adiabatic} - T_{ref}) + \frac{CO_{2,b}}{2} * (T_{adiabatic}^2 - T_{ref}^2)] \quad (A.53)$$

$$Hf_{H2O,P} = n_{H2O} * (\Delta Hf_{H2O(g),298K} + [H_2O(g)_{.a} * (T_{adiabatic} - T_{ref}) + \frac{H_2O(g)_{.b}}{2} * (T_{adiabatic}^2 - T_{ref}^2)] \quad (A.54)$$

$$Hf_{N2,P} = n_{N2,P} * (\Delta Hf_{N2,298K} + [N_{2,a} * (T_{adiabatic} - T_{ref}) + \frac{N_{2,b}}{2} * (T_{adiabatic}^2 - T_{ref}^2)] \quad (A.55)$$

$$Hf_{O2,P} = n_{O2,P} * (\Delta Hf_{O2,298K} + [O_{2,a} * (T_{adiabatic} - T_{ref}) + \frac{O_{2.b}}{2} * (T_{adiabatic}^2 - T_{ref}^2)] \quad (A.56)$$

$$Hf_{ash,P} = n_{ash} * (\Delta Hf_{SiO2,298K} + [SiO_{2,a} * (T_{adiabatic} - T_{ref}) + \frac{SiO_{2,b}}{2} * (T_{adiabatic}^2 - T_{ref}^2)] \quad (A.57)$$

$$Hf_{SO2,P} = n_{SO2} * (\Delta Hf_{SO2,298K} + [SO_{2.a} * (T_{adiabatic} - T_{ref}) + \frac{SO_{2,b}}{2} * (T_{adiabatic}^2 - T_{ref}^2)] \quad (A.58)$$

If the dissociation reaction were included and the pressure is assumed as 1 atm, then the equilibrium constant Kp_{CO} was determined according to Equation A.59. [30]:

$$Kp_{CO} = \frac{P_{CO}^o * P_{H2O}^o}{P_{CO2}^o * P_{H2}^o} \rightarrow \{1\ atm\} \rightarrow\ Kp_{CO} = \frac{Y_{CO} * Y_{H2O}}{Y_{CO2} * Y_{H2}} = 33.7 * e^{-\frac{-4094}{T_{adiabatic}}} \text{ [30]} \quad (A.59)$$

A. Calculations of the adiabatc flame temperature

Where, the molar flow rate of CO_2 and H_2would dissociate in an equal amount of mol/s to CO and H_2O, thus, the molar flow rates of the products were determined according to Equations A.60, A.61, A.62, A.63, A.64, A.65, A.66 and A.67.

$$n_{H2} = n_{H2} - n_{H2,d} \quad \text{(A.60)}$$

$$n_{CO2} = n_C - n_{H2,d} \quad \text{(A.61)}$$

$$n_{H2O} = n_{moist} + n_{H2} + n_{H2.d} \quad \text{(A.62)}$$

$$n_{SO2} = n_S \quad \text{(A.63)}$$

$$n_{CO} = n_{H2,d} \quad \text{(A.64)}$$

$$n_{N2,p} = (n_{O2,req} * \frac{79}{21} * \lambda + n_{N2}) \quad \text{(A.65)}$$

$$n_{O2,p} = n_{O2,req} * (\lambda - 1) \quad \text{(A.66)}$$

$$n_{tot} = n_{O2} + n_{N2} + n_{CO2} + n_{H2O} + n_{SO2} + n_{CO} \quad \text{(A.67)}$$

Thus, the molar fraction of each component could be determined, Equations A.68, A.69, A.70, A.71 and A.72, which, was needed to calculate the equilibrium constant, Equation A.59.

$$Y_{CO} = \frac{n_{CO}}{n_{tot}} \quad \text{(A.68)}$$

$$Y_{H2O} = \frac{n_{H2O}}{n_{tot}} \quad \text{(A.69)}$$

$$Y_{CO2} = \frac{n_{CO2}}{n_{tot}} \quad \text{(A.70)}$$

$$Y_{H2} = \frac{n_{H2}}{n_{tot}} \quad \text{(A.71)}$$

The molar flow rate of the dissociated, $n_{H2,d}$ was determined by iteratively guessing the molar flow rate until, Equation A.59 was satisfied for the corresponding guessed adiabatic temperature, $T_{adiabatic}$.

Appendix B. Figures

B.1 Figures: Data input

B.1.1 Figures: Data input: Hydrogen cases

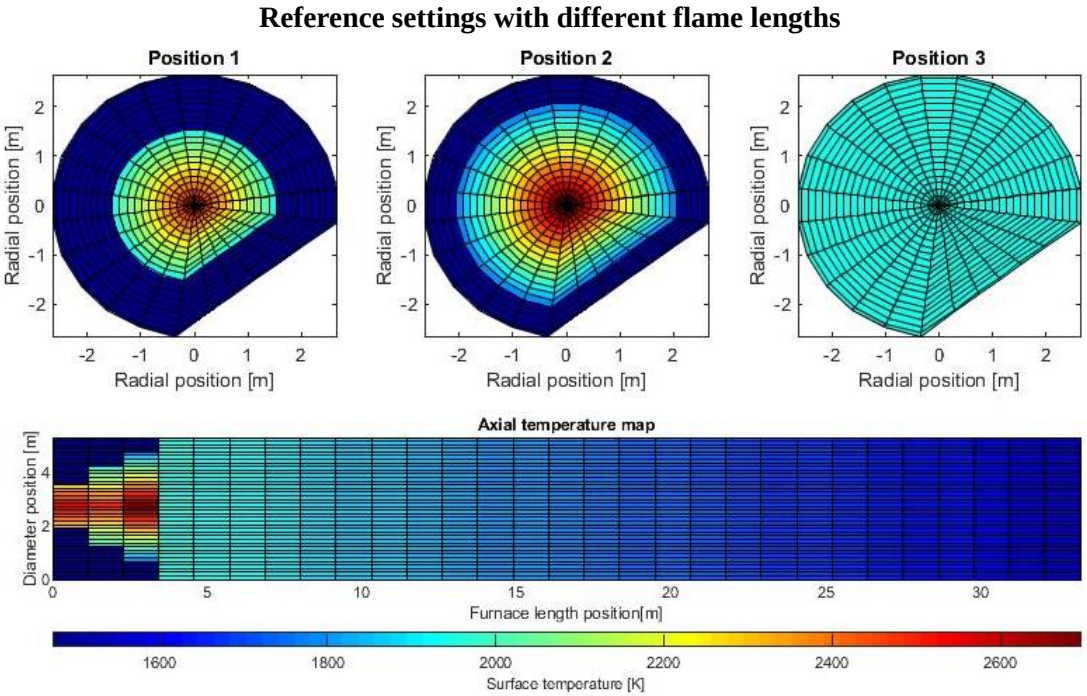

Figure B.1: The data input of the temperature profile for a 3.4m hydrogen flame with the reference settings.

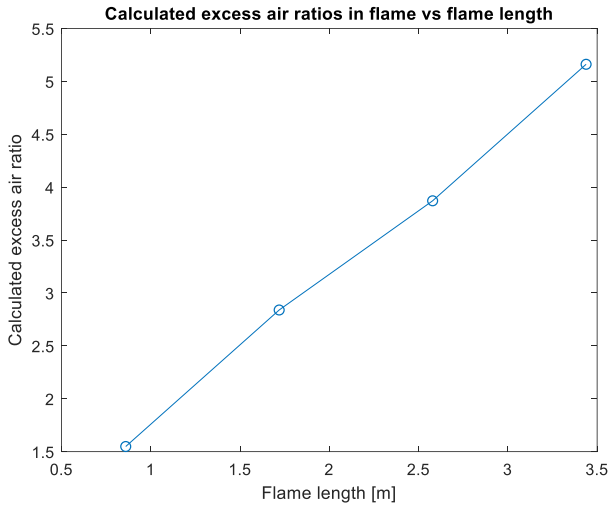

Figure B.2: The data input of the calculated excess air ratios as a function of the flame length, for a 3.4m hydrogen flame.

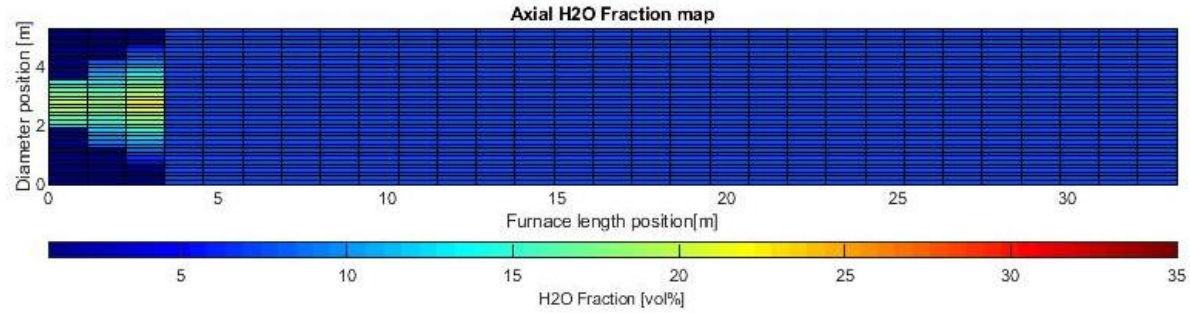

Figure B.3: The data input of the H_2O concentration for a 3.4m hydrogen flame.

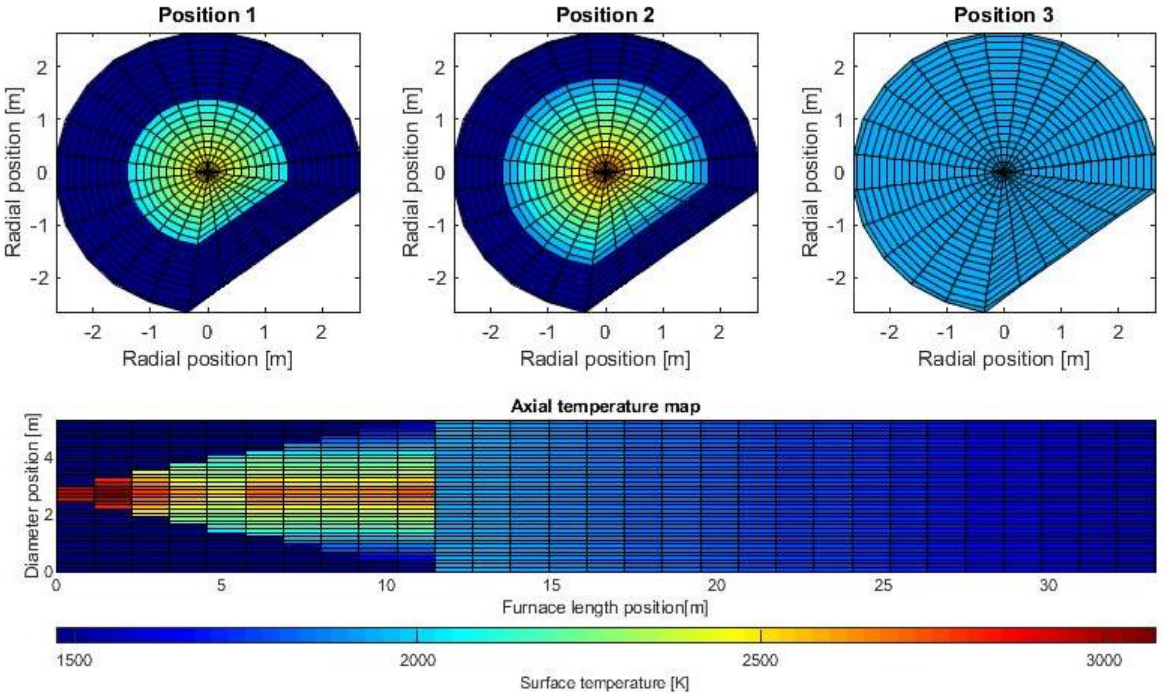

Figure B.4: Data input of the temperature profile for a 11.4m hydrogen flame with the reference settings.

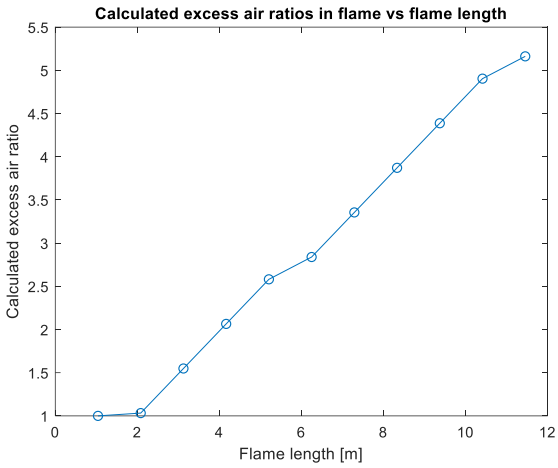

Figure B.5: The data input of the calculated excess air ratios as a function of the flame length, for a 11.4m hydrogen flame.

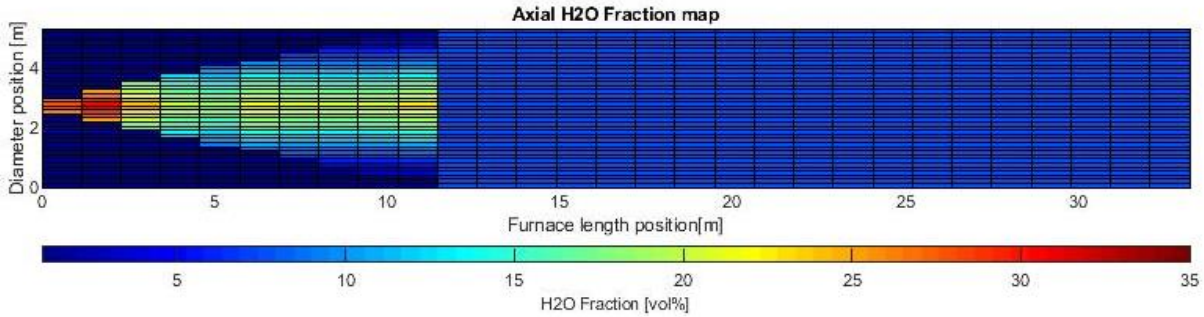

Figure B.6: The data input of the H_2O concentration for a 11.4m hydrogen flame.

Temperature study

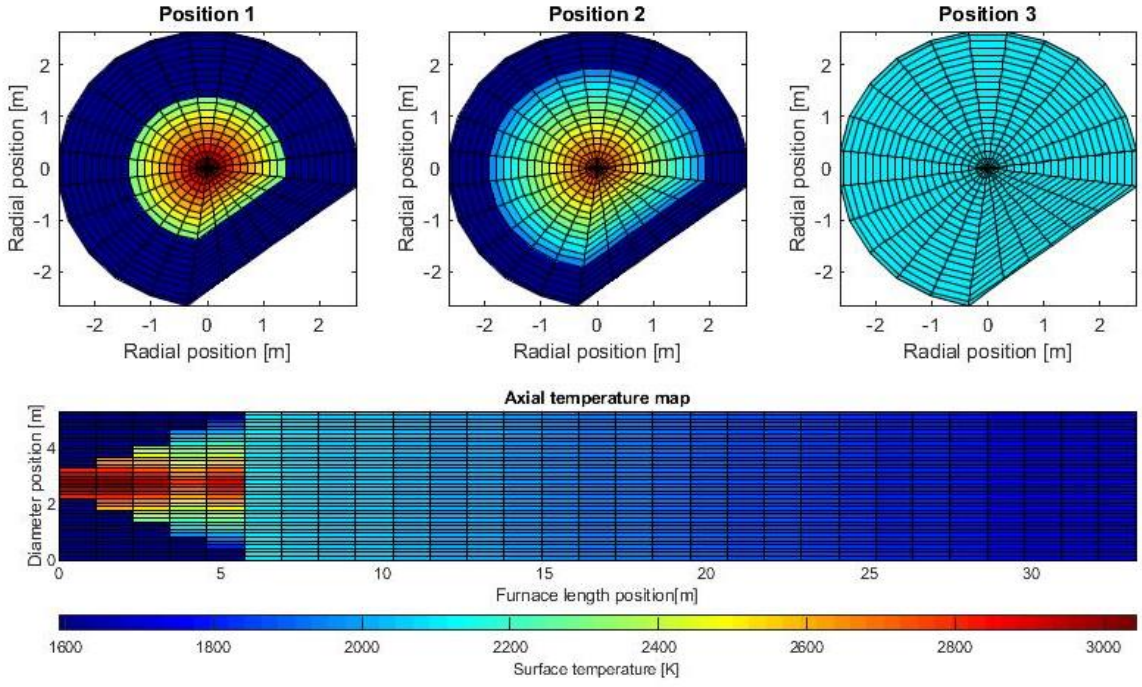

Figure B.7: Data input of the temperature profile for a 5.4m hydrogen flame with 8% gas temperature increase in all cells.

B. Figures

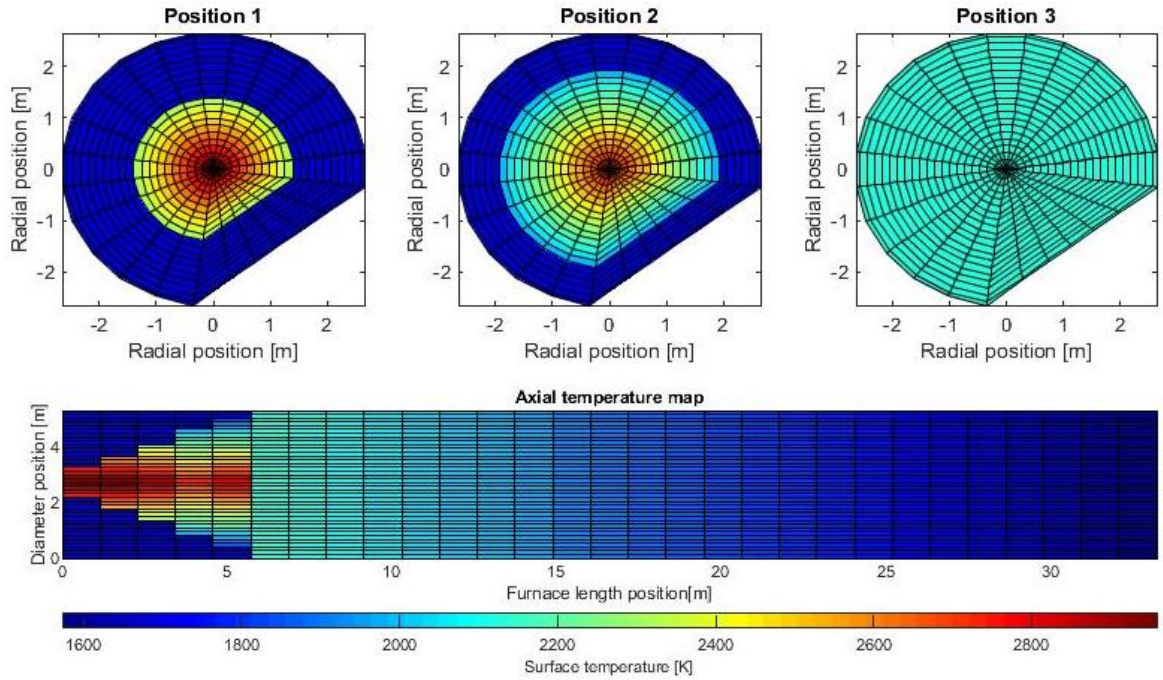

Figure B.8: Data input of the temperature profile for a 5.4m hydrogen flame with a gas temperature of 1400°C from the cooler.

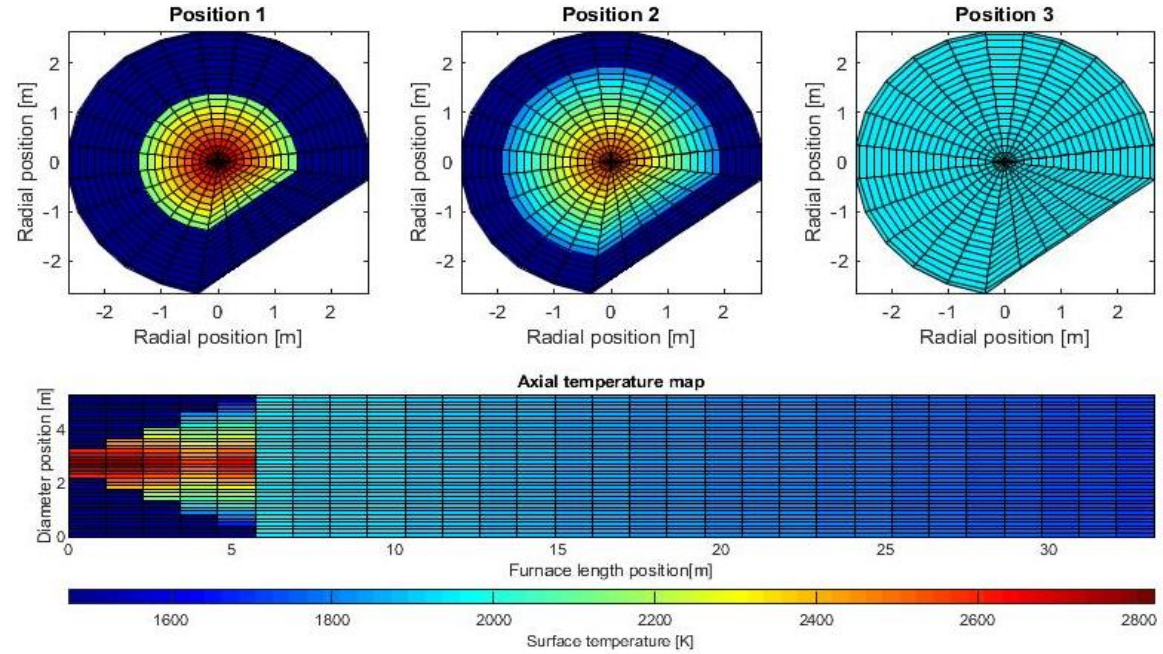

Figure B.9: Data input of the temperature profile for a 5.4m hydrogen flame with a gas temperature of 1440°C to the PH-zone.

B. Figures

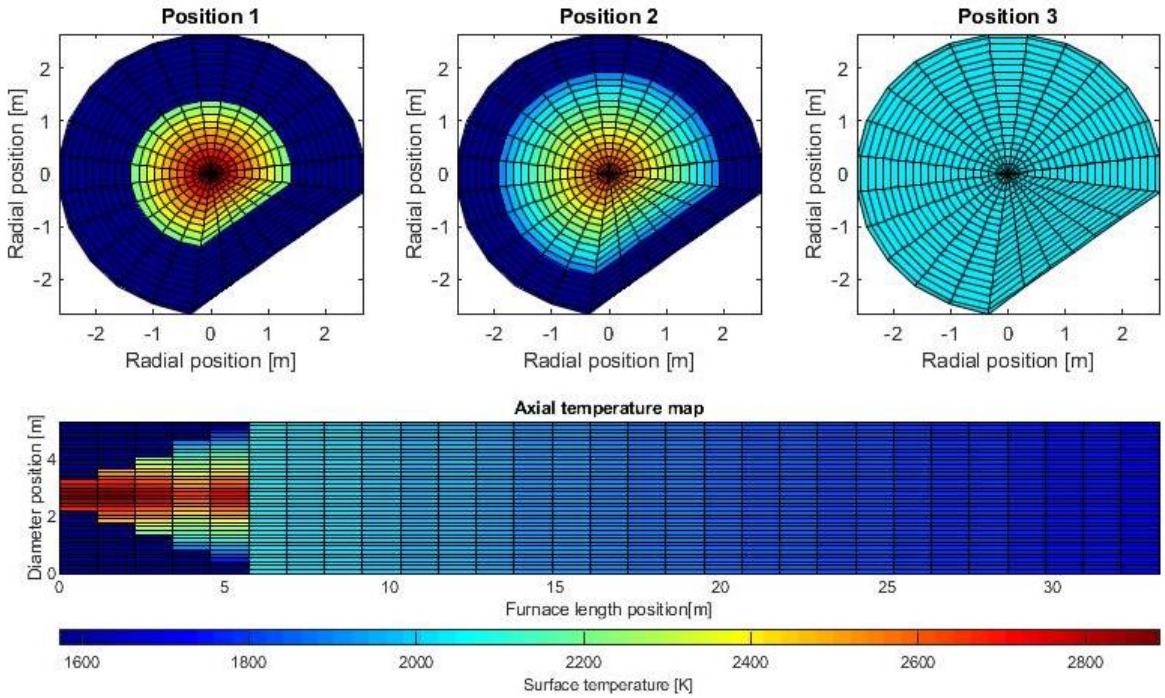

Figure B.10: Data input of the temperature profile for a 5.4m hydrogen flame with a gas temperature of 1440°C to the PH-zone and a gas temperature of 1300°C to the cooler.

Higher cell resolution

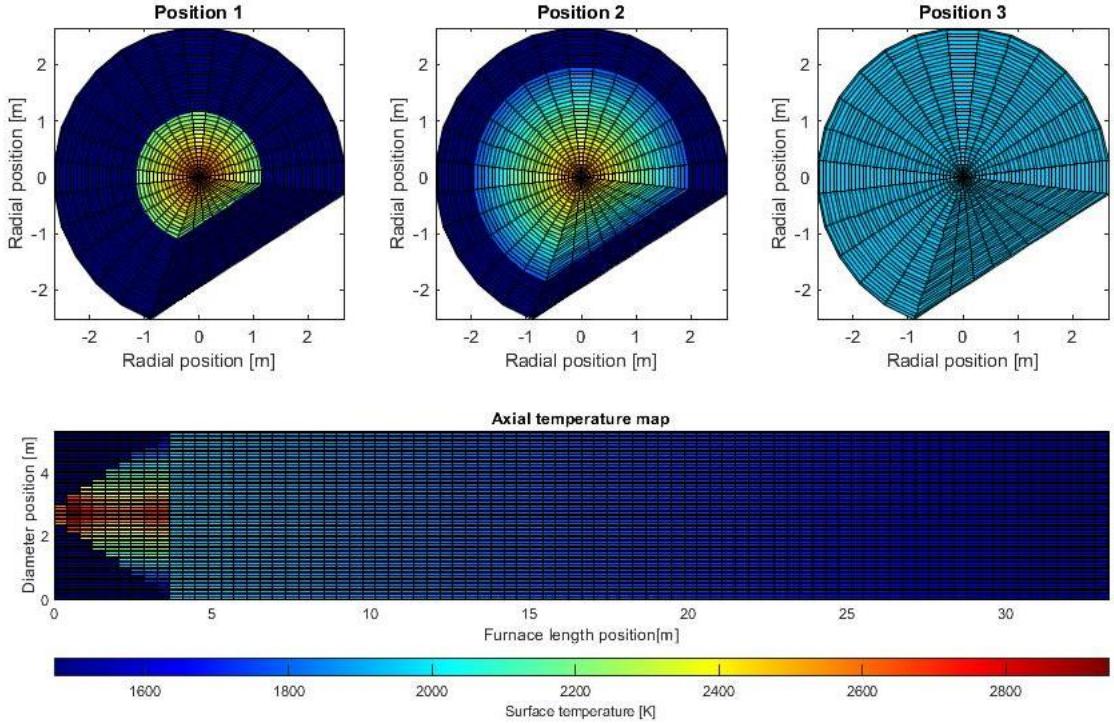

Figure B.11: Data input of the temperature profile for a 3.4m hydrogen flame with higher number of cells.

B. Figures

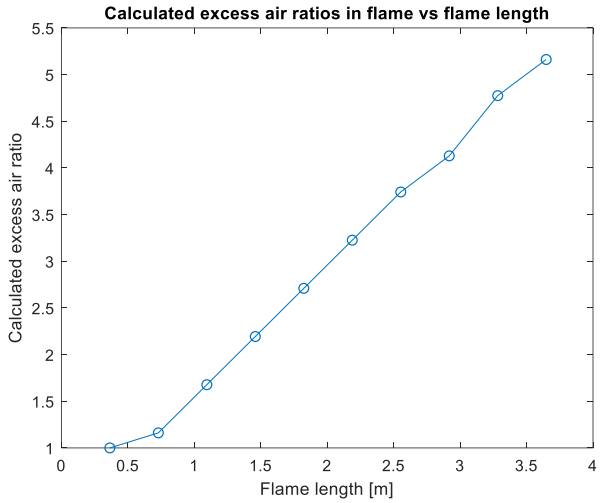

Figure B.12: The data input of the calculated excess air ratios as a function of the flame length, for a 3.4m hydrogen flame with a higher number of cells.

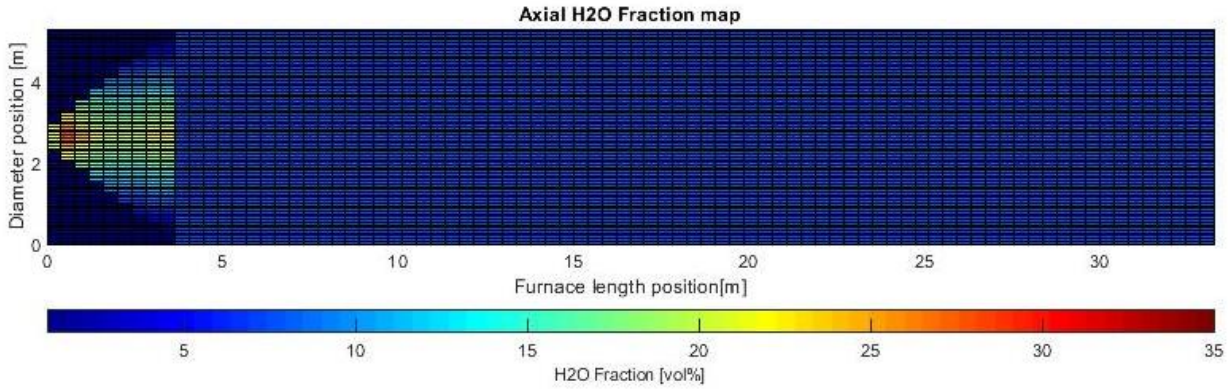

Figure B.13: The data input of the H_2O concentration for a 3.4m hydrogen flame with a higher number of cells.

B. Figures

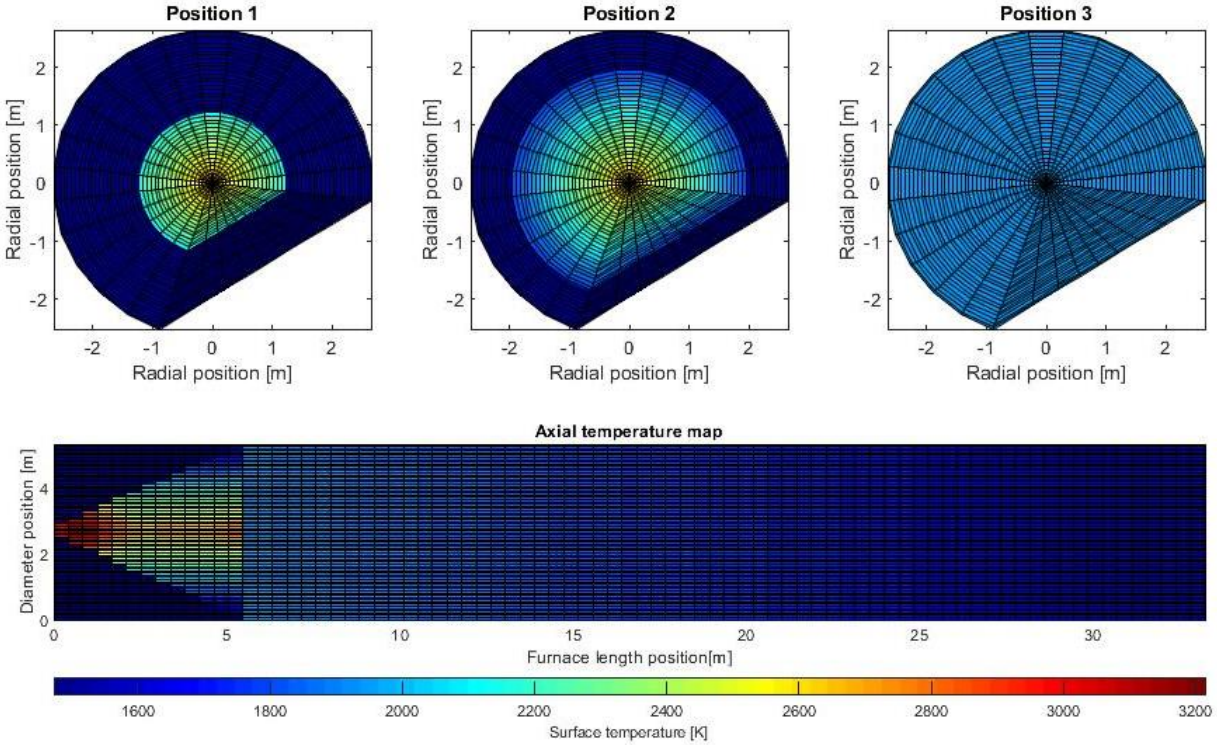

Figure B.14: The data input of the temperature profile for a 5.4m hydrogen flame with a higher number of cells.

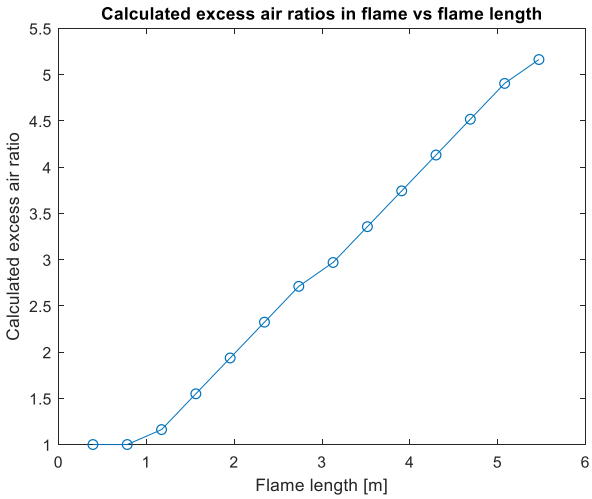

Figure B.15: The data input of the calculated excess air ratios as a function of the flame length, for a 5.4m hydrogen flame with a higher number of cells.

B. Figures

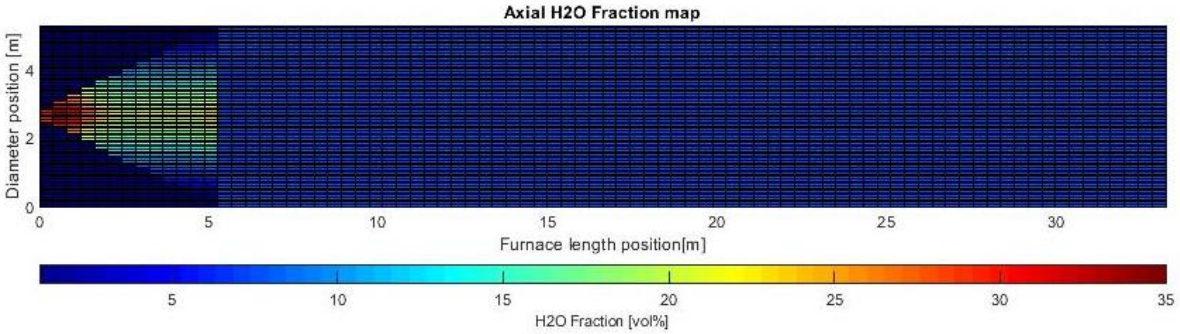

Figure B.16: Data input of the H_2O concentration for a 5.4m hydrogen flame with a higher number of cells.

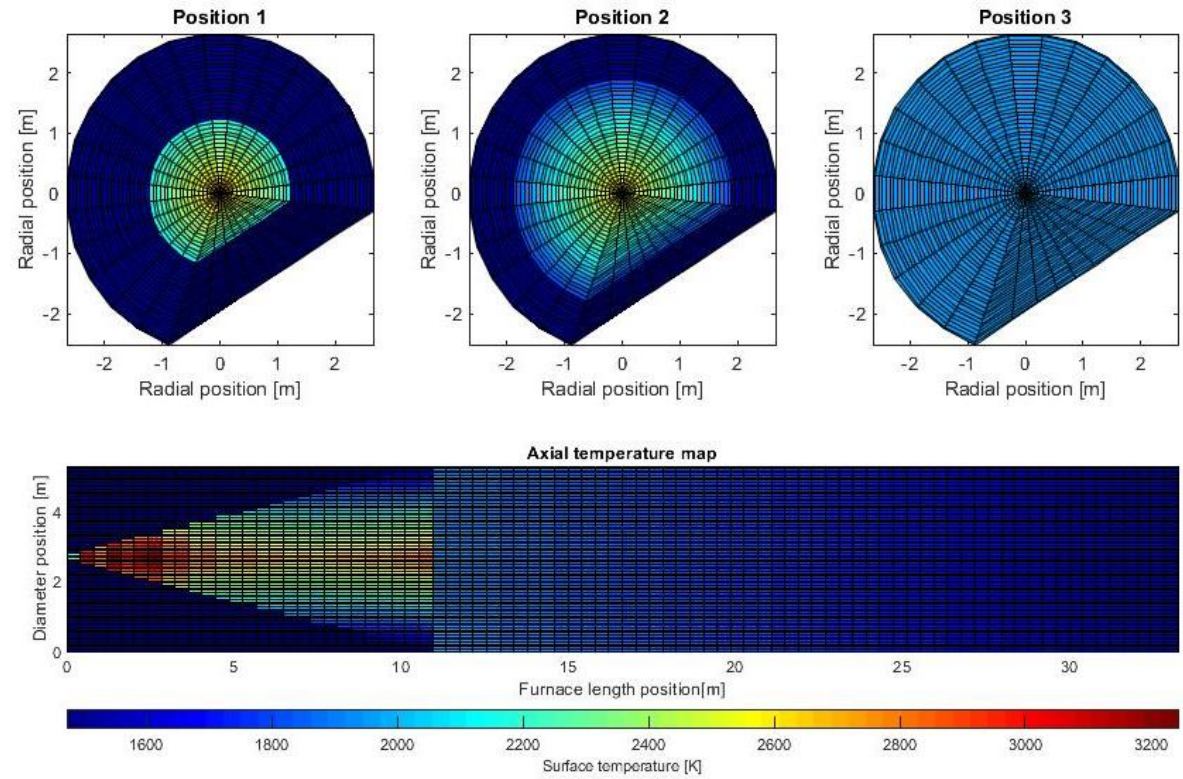

Figure B.17: Data input of the temperature profile for a 11.4m hydrogen flame with a higher number of cells.

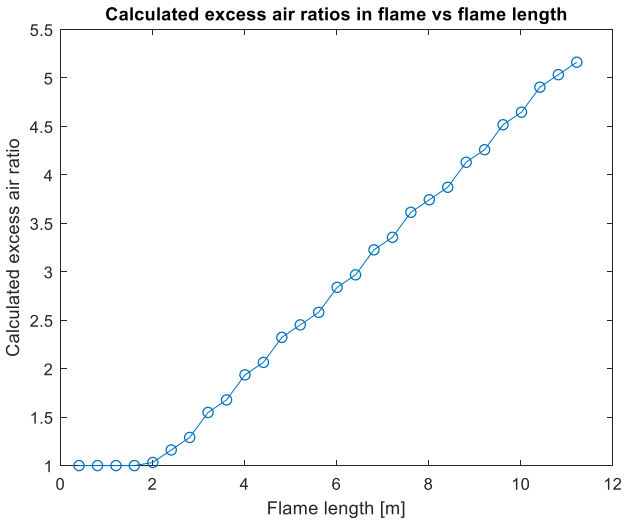

Figure B.18: The data input of the calculated excess air ratios as a function of the flame length, for a 11.4m hydrogen flame with a higher number of cells.

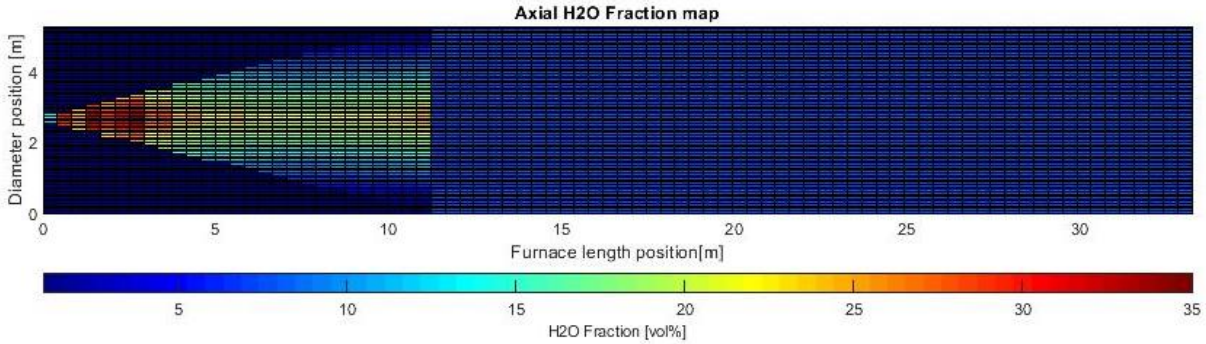

Figure B.19: The data input of the H_2O concentration for a 11.4m hydrogen flame with a higher number of cells.

Table B.1: The data input of the particle concentration for a hydrogen flame with added iron ore dust particles, (IOD) [26].

Flame length [m]	**Added particles in flame [%]**	**Particle concentration $[m^2 particles/m^3 air * 10^{-2}]$**
11.4	3	0.84
5.4	7	1.14
3.4	16	1.86

B.1.2 Figures: Data input: Coal cases

Data input for the 11.4m coal flame are listed in Section 3.4.2. In this section the data input for the 21.8m coal flame is presented.

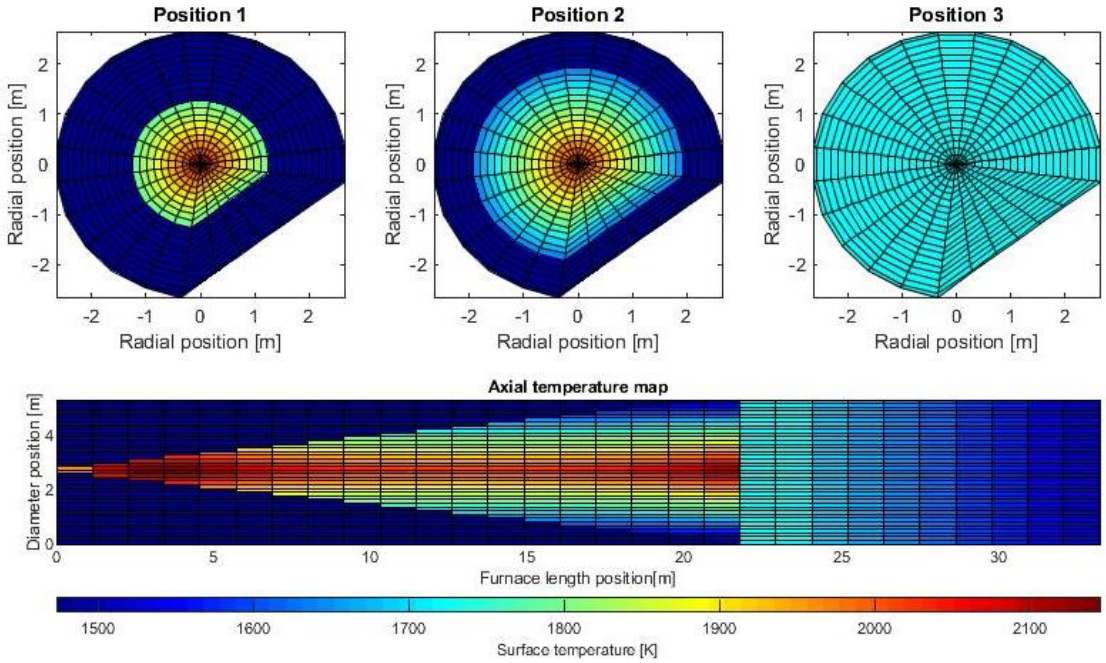

Figure B.20: The data input of the temperature profile for a 21.8m coal flame with a gas temperature of 1230°C to the PH-zone.

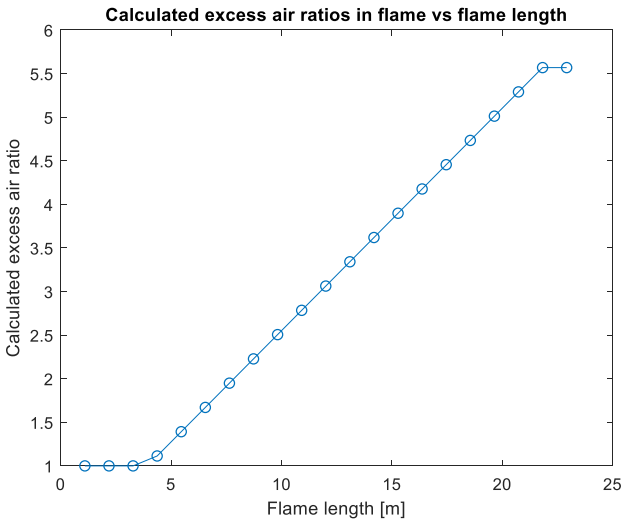

Figure B.21: The data input of the calculated excess air ratios as a function of the flame length, profile for a 21.8m coal flame.

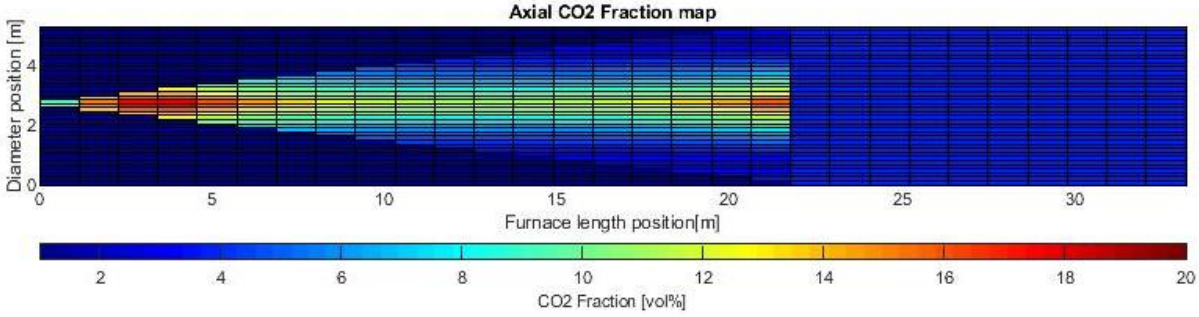

Figure B.22: The data input of the CO_2 concentration for a 21.8m coal flame.

B. Figures

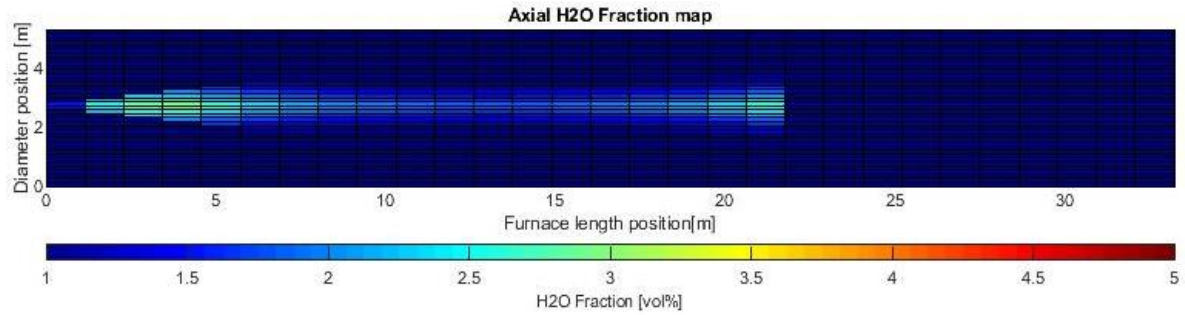

Figure B.23: The data input of the H_2O concentration for a 21.8m coal flame.

Table B.2: The data input of the particle and soot concentration for a 21.8 coal flame.

Particle concentration: Coal flame 21.8m	**Soot concentration: Coal flame 21.8m**
31.6*10^{-2} $[m^2 particles/m^3 air]$	3.90*$10^{-9}$$[m^2 soot/m^3 air]$

Hydrogen added to the coal flame

Soot and particle concentrations are listed in a table at the end of the figures for this study.

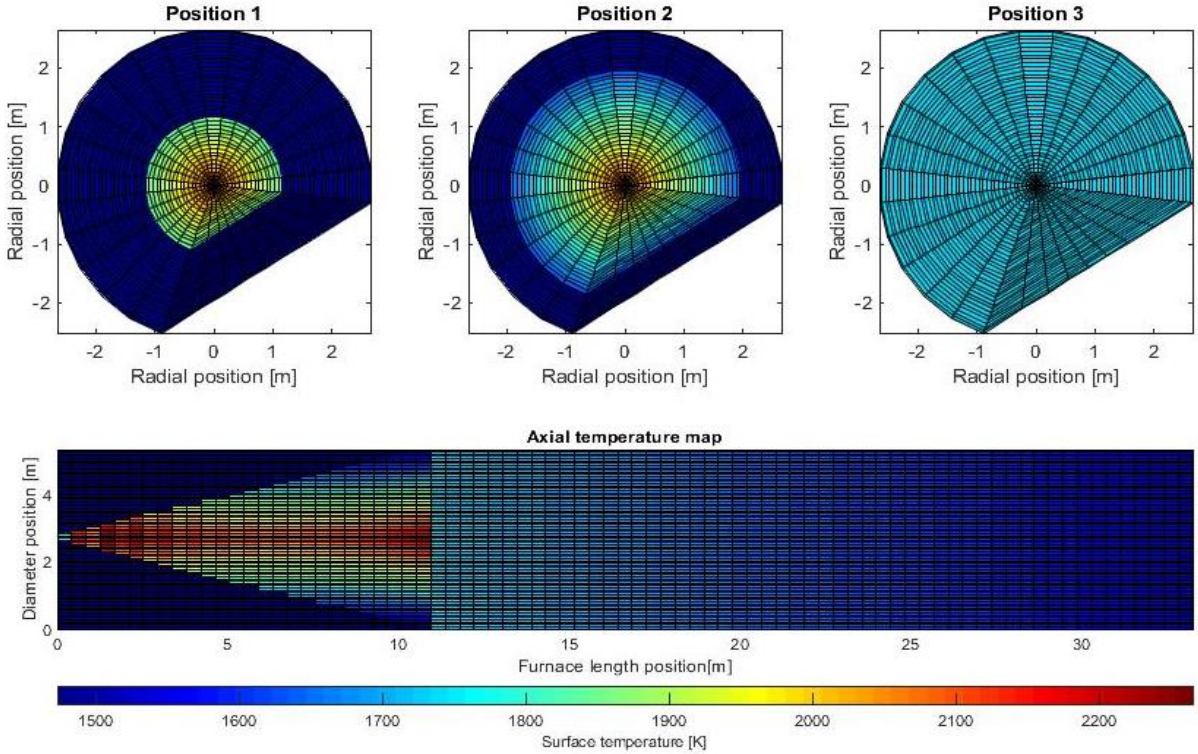

Figure B.24: The data input of the temperature profile for a 11.4m coal flame with 10% added hydrogen.

B. Figures

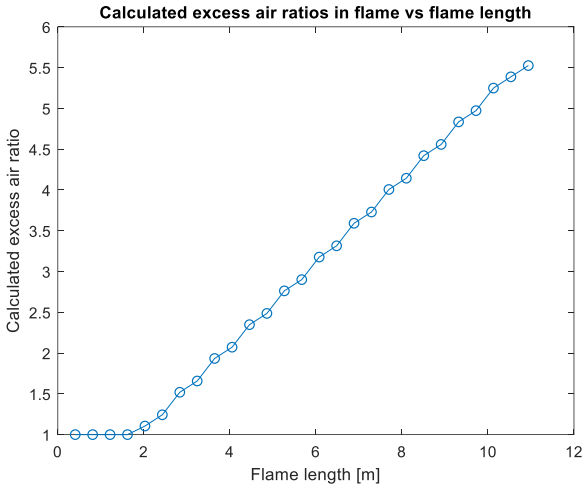

Figure B.25: The data input of the calculated excess air ratios as a function of the flame length, profile for a 11.4m coal flame with 10% added hydrogen.

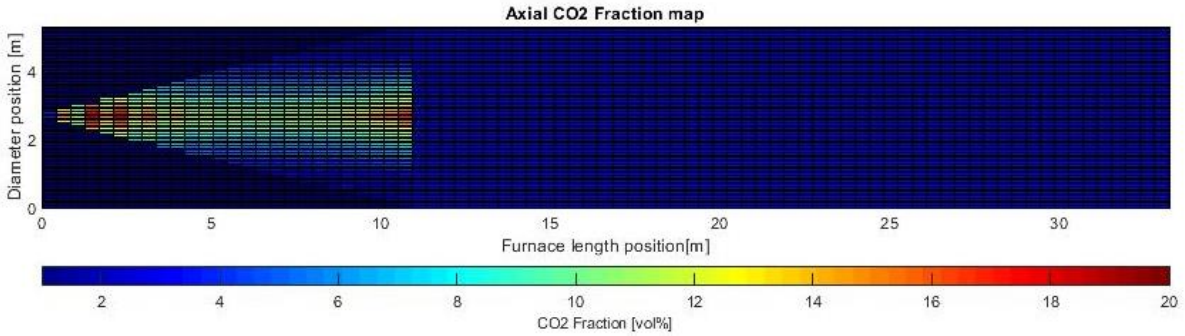

Figure B.26: The data input of the CO_2 concentration for a 11.4m coal flame with 10% added hydrogen.

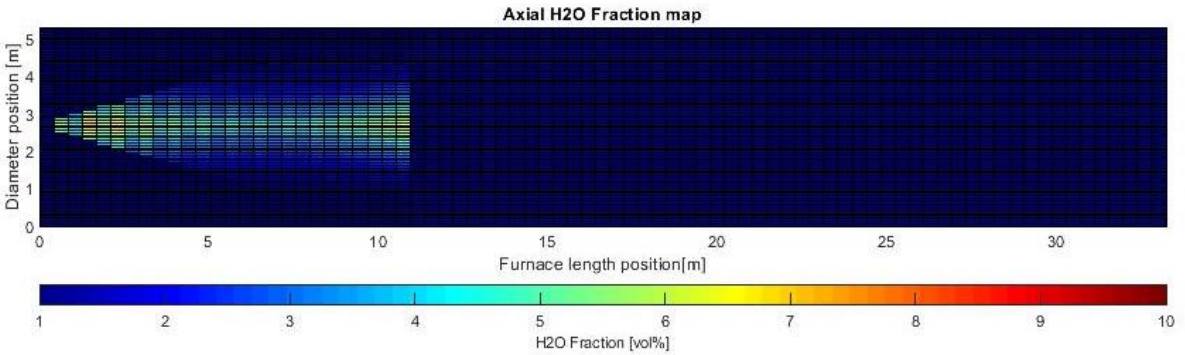

Figure B.27: The data input of the H_2O concentration for a 11.4m coal flame with 10% added hydrogen.

B. Figures

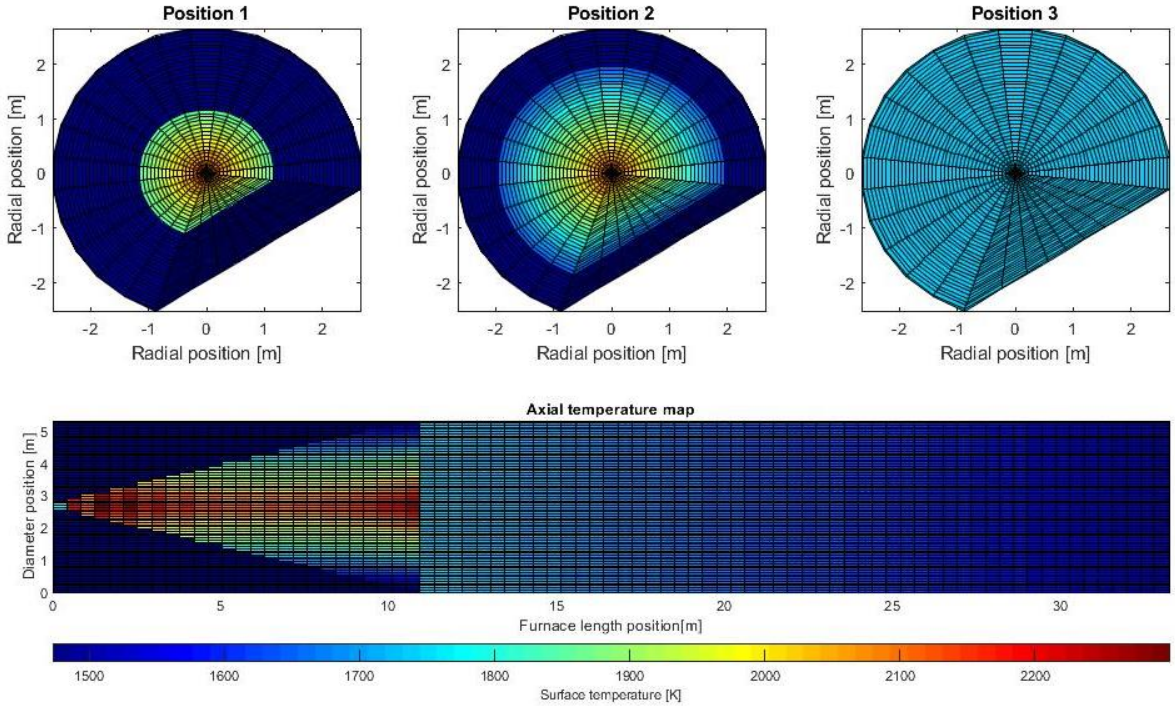

Figure B.28: The data input of the temperature profile for a 11.4m coal flame with 15% added hydrogen.

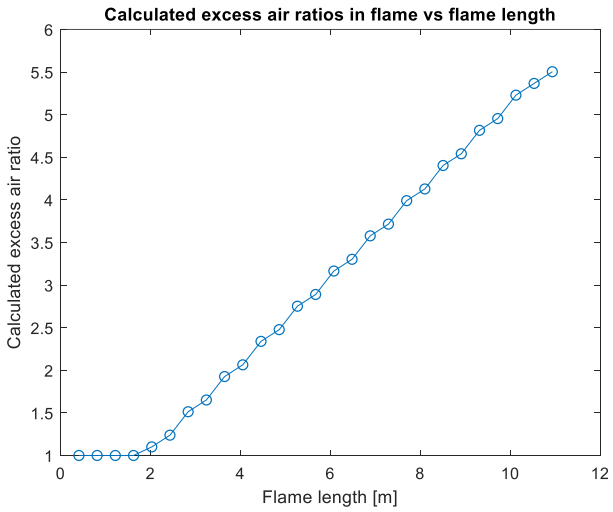

Figure B.29: The calculated excess air ratios vs the flame length for a 11.4m coal with 15% added hydrogen case.

B. Figures

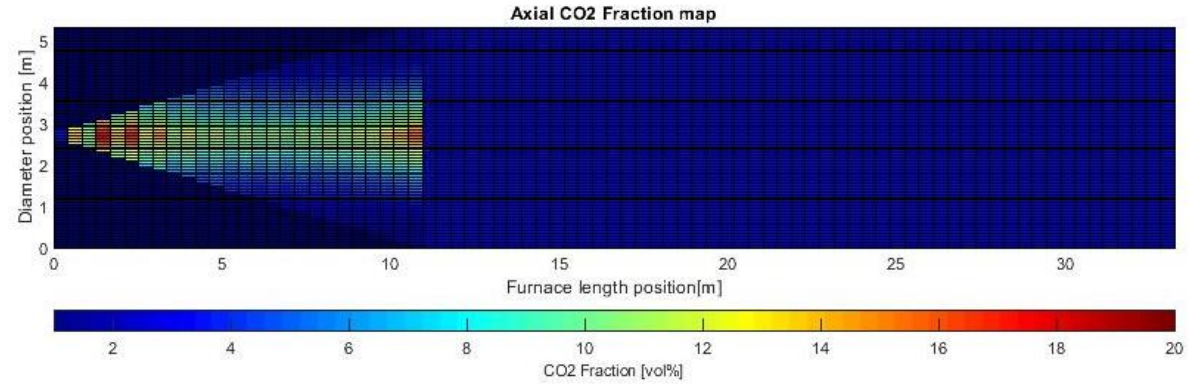

Figure B.30: The data input of the CO_2 concentration for a 11.4m coal with 15% added hydrogen case.

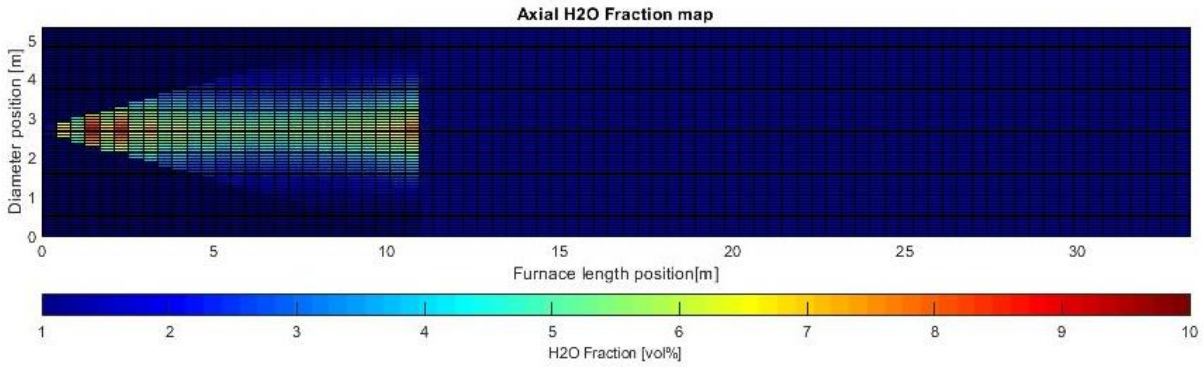

Figure B.31: The data input of the H_2O concentration for a 11.4m coal with 15% added hydrogen case.

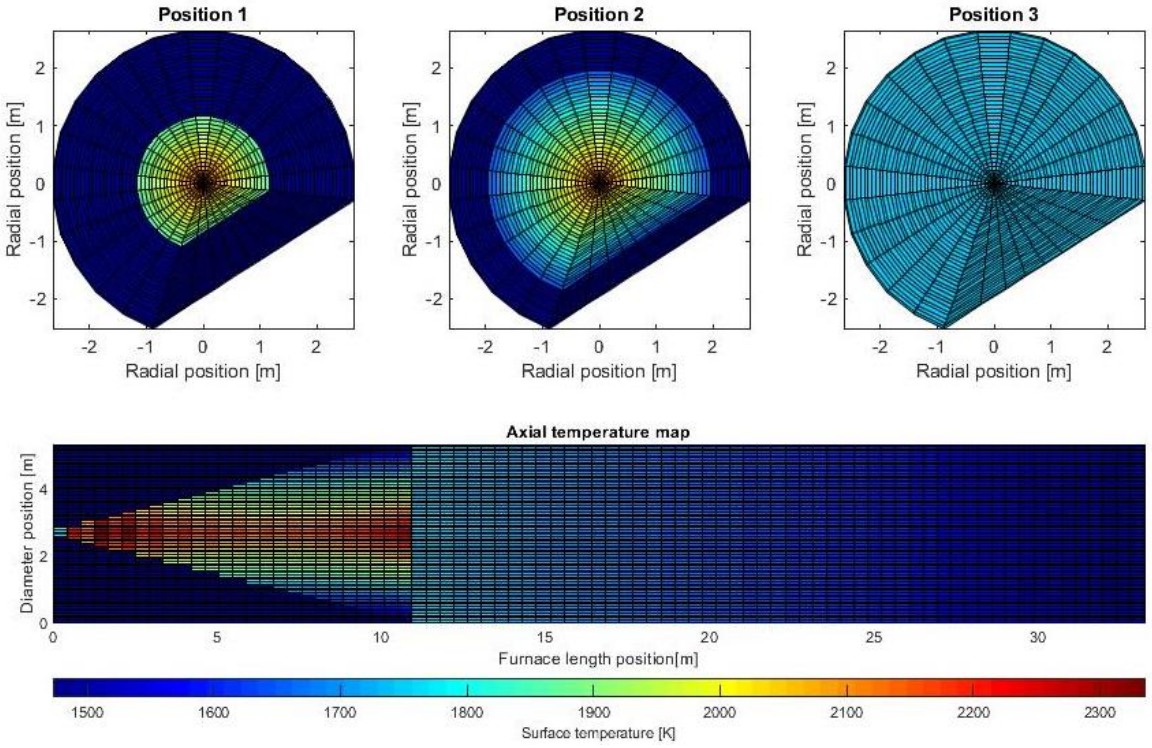

Figure B.32: The data input of the temperature profile for a 11.4m coal flame with 20% added hydrogen.

B. Figures

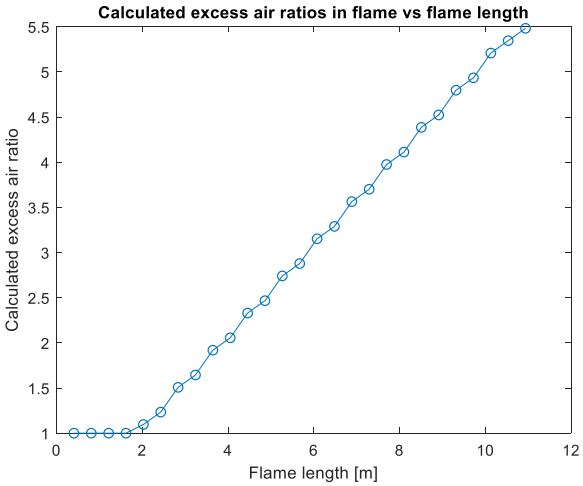

Figure B.33: The calculated excess air ratios vs the flame length for a 11.4m coal with 20% added hydrogen case.

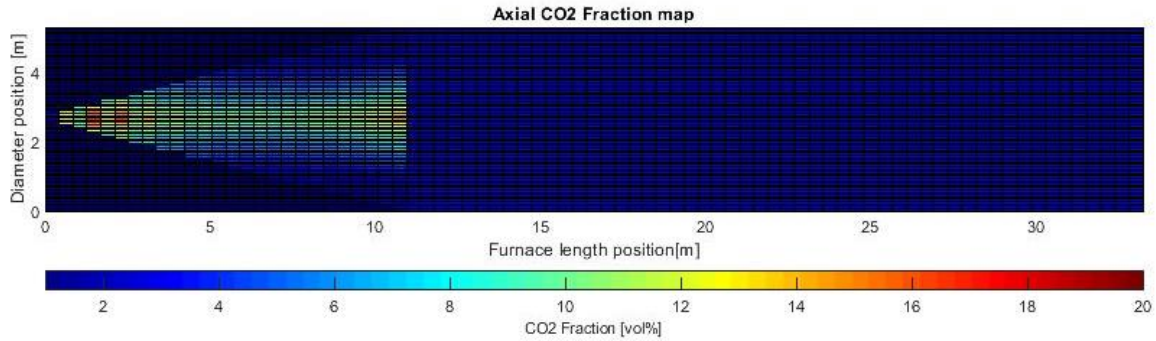

Figure B.34: The data input of the CO_2 concentration for a 11.4m coal with 20% added hydrogen case.

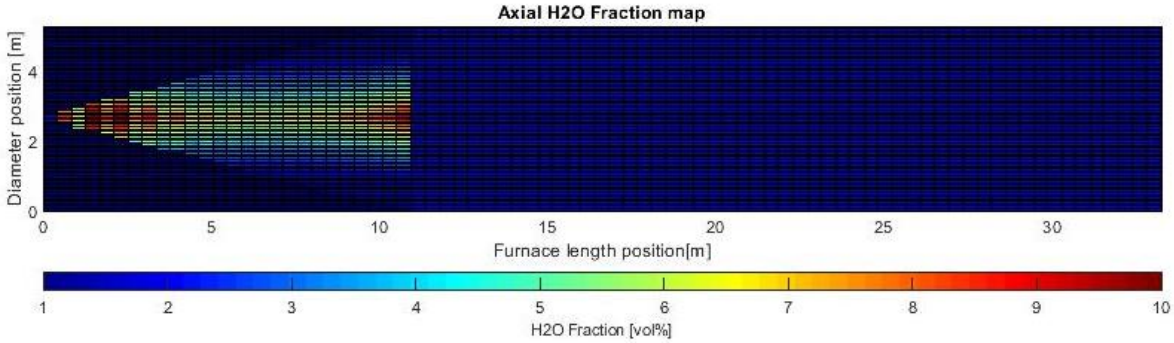

Figure B.35: The data input of the H_2O concentration for a 11.4m coal with 20% added hydrogen case.

Table B.3: The data input of the particle and soot concentration for a 11.4m coal flame with added hydrogen.

Added hydrogen (%)	**Particle concentration $[m^2 particles/m^3 air * 10^{-2}]$**	**Soot concentration $[m^2 soot/m^3 air * 10^{-9}]$**
10	24.3	2.26
15	22.9	2.26
20	21.6	2.26

B.1.3 Figures: Data input: Oil cases

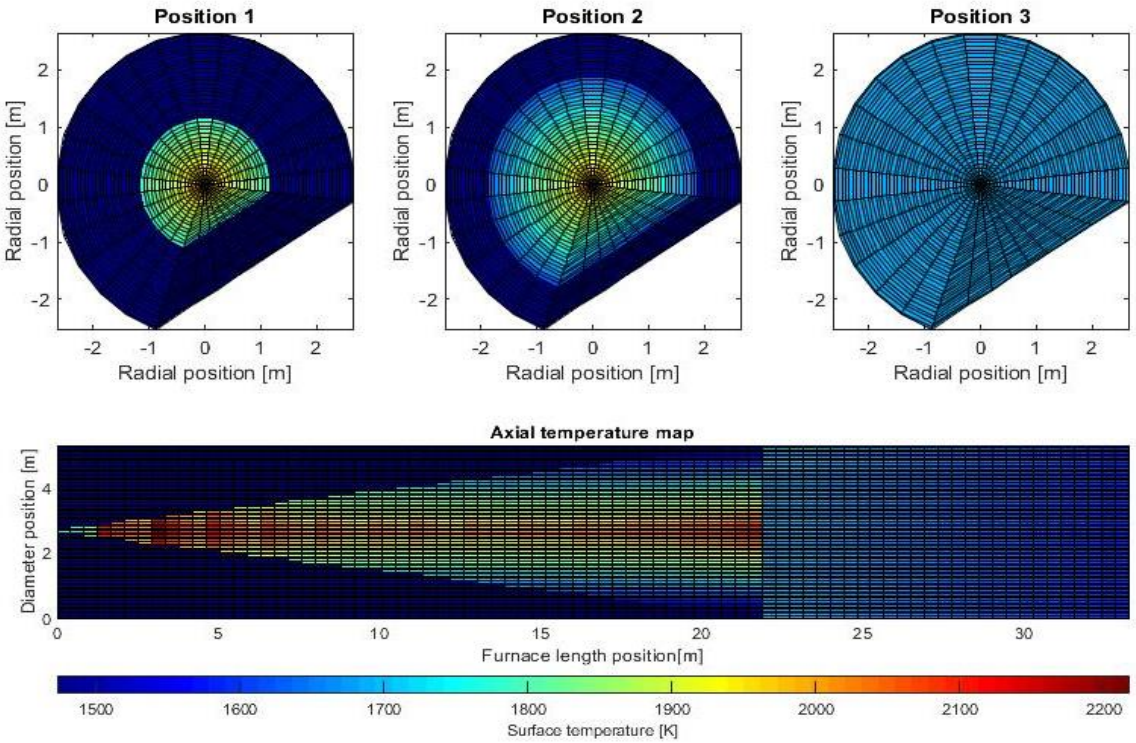

Figure B.36: The data input of the temperature profile for a 21.8m oil flame with a gas temperature of 1320°C to the PH-zone.

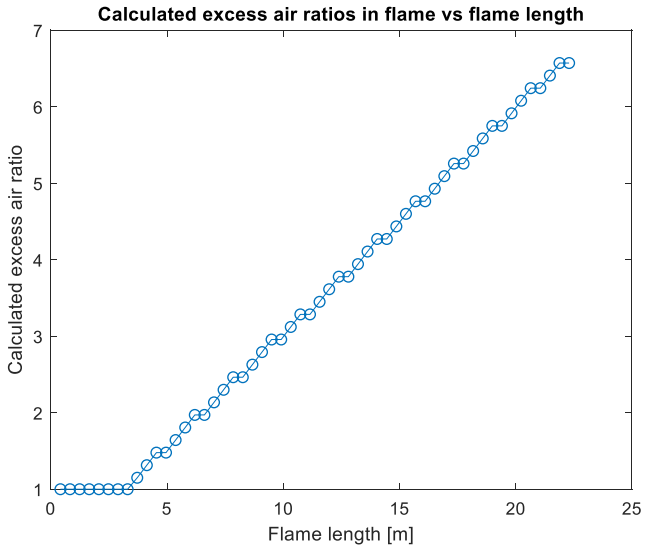

Figure B.37: The calculated excess air ratios vs the flame length for a 21.8m oil flame.

B. Figures

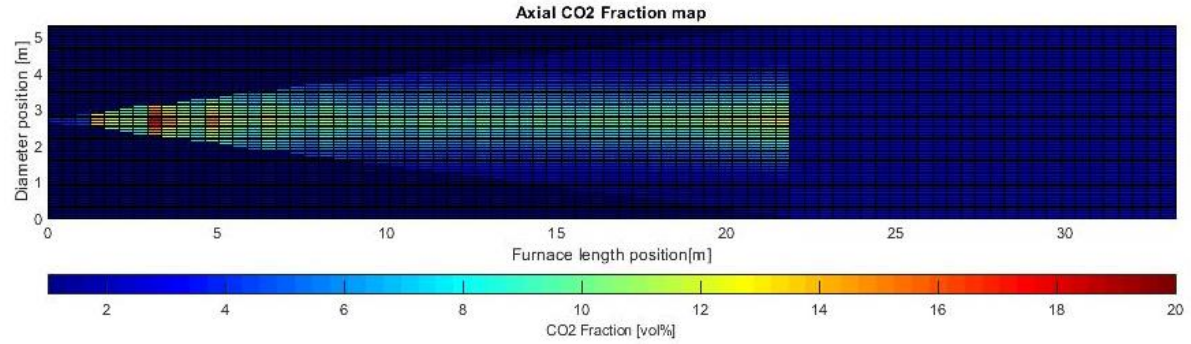

Figure B.38: The data input of the CO_2 concentration for a 21.8m oil flame.

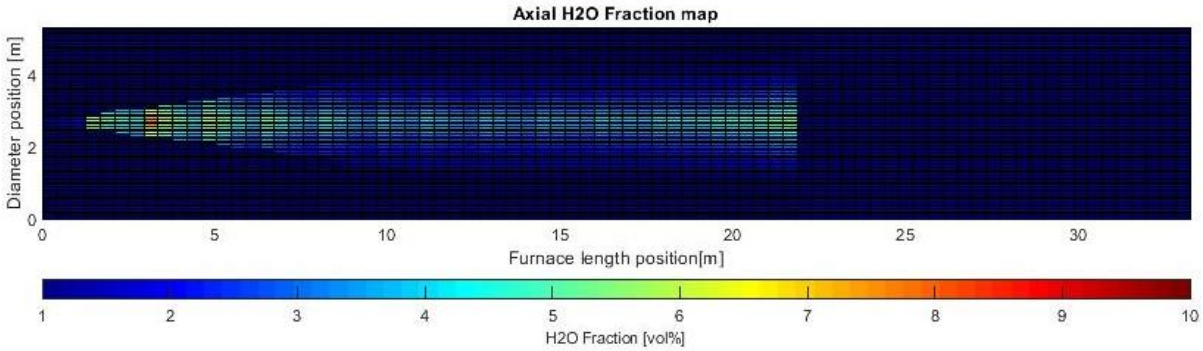

Figure B.39: The data input of the H_2O concentration for a 21.8m oil flame.

Table B.4: The data input of the particle and soot concentration for a 21.8m oil flame. Note that a higher cell resolution was used for this case.

Particle concentration: Oil flame 21.8m	**Soot concentration: Oil flame 21.8m**
$28.6*10^{-2}$ $[m^2 particles/m^3 air]$	$3.58*10^{-9}[m^2 soot/m^3 air]$

B.2 Figures & Tables: Adiabatic flame temperature

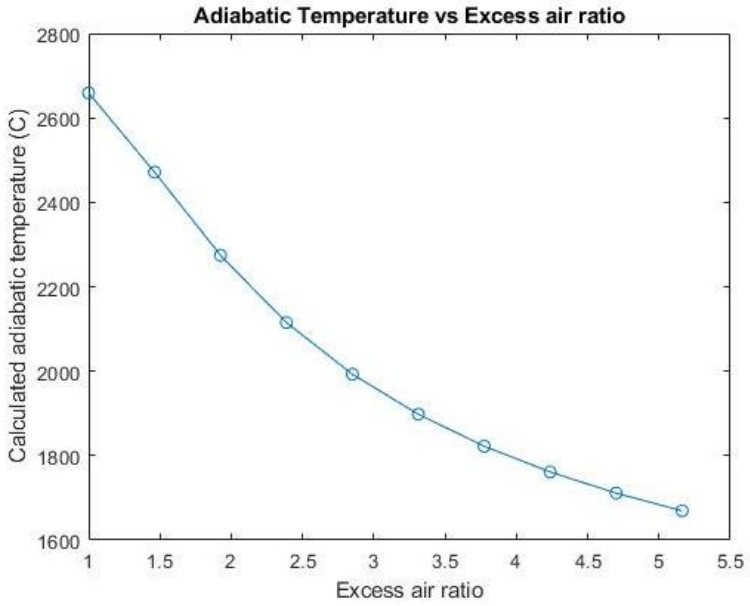

Figure B.40: The adiabatic flame temperature of hydrogen combustion as a function of the excess air ratio with respect to the dissociation of water vapor.

Table B.5: The calculated adiabatic flame temperatures of hydrogen, the H_2O composition in the product gases, and the amount of H_2O that will dissociate.

Excess air ratio	**Adiabatic flame temperature (°C)**	**H_2O composition (vol%)**	**H_2O that dissociates (%)**
1.00	2659	28.3	16.1
1.50	2471	23.5	5.7
1.90	2274	19.3	1.9
2.40	2115	16	0.7
2.90	1993	13.7	0.2
3.30	1898	11.9	0
3.80	1822	10.5	0
4.20	1761	9.4	0
4.70	1711	8.6	0
5.20	1669	7.8	0

B. Figures

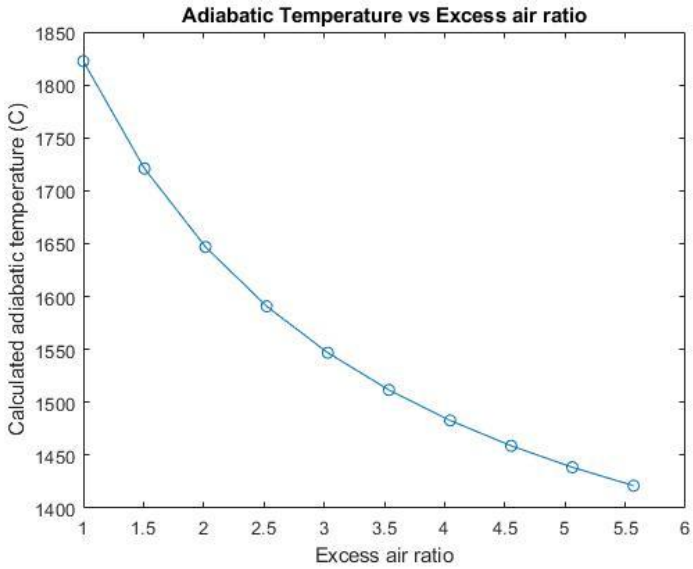

Figure B.41: The adiabatic flame temperature of coal as a function of the excess air ratio, with respect of dissociation.

Table B.6: The tabular data from the adiabatic flame temperature function for coal, with respect to dissociation.

Excess air ratio	**Adiabatic flame temperature (°C)**	**H_2O composition (vol%)**	**CO_2 composition (vol%)**	**H_2 that dissociates (%)**	**CO_2 that dissociates (%)**
1.00	1823	3.30	17.4	96.1	14.9
1.50	1721	2.20	11.7	95.7	14.9
2.00	1647	1.70	8.80	95.3	14.8
2.50	1591	1.40	7.00	95.1	14.8
3.00	1547	1.10	6.00	94.8	14.7
3.50	1512	0.96	5.00	94.6	14.7
4.00	1483	0.80	4.40	94.4	14.7
4.60	1459	0.75	3.90	94.2	14.6
5.10	1439	0.68	3.50	94	14.6
5.60	1421	0.62	3.20	93.9	14.6

B. Figures

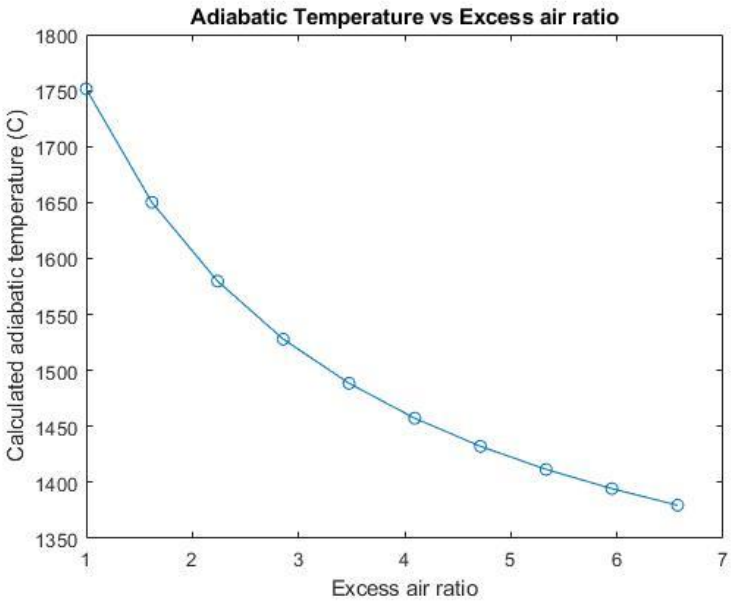

Figure B.42: The adiabatic flame temperature of oil as a function of the excess air ratio, with respect of dissociation

Table B.7: The tabular data from the adiabatic flame temperature function for oil, with respect to dissociation.

Excess air ratio	**Adiabatic flame temperature (°C)**	**H_2O composition (vol%)**	**CO_2 composition (vol%)**	**H_2 that dissociates (%)**	**CO_2 that dissociates (%)**
1.00	1751	7.80	12.0	85.0	35.0
1.60	1650	5.00	7.80	83.0	34.4
2.20	1580	3.60	5.80	81.5	33.7
2.90	1528	2.90	5.00	80.0	33.2
3.50	1488	2.40	4.80	79.0	32.7
4.10	1457	2.00	3.30	78.0	32.4
4.70	1432	1.70	2.80	77.5	32.0
5.30	1412	1.50	2.50	76.7	31.8
6.00	1395	1.40	2.30	76.0	31.4
6.60	1380	1.10	2.00	75.6	31.3

Table B.8: The tabular data from the adiabatic flame temperature function for coal with 10% added hydrogen.

Excess air ratio	**Adiabatic flame temperature (°C)**	**H_2O composition (vol%)**	**CO_2 composition (vol%)**
1.00	1957	6.50	17.2
1.50	1823	4.40	11.6
2.00	1736	3.30	8.80
2.50	1667	2.70	7.00
3.00	1613	2.20	5.90
3.50	1570	1.90	5.00
4.00	1535	1.70	4.40
4.50	1506	1.50	3.90
5.00	1481	1.30	3.50
5.50	1460	1.20	3.20

Table B.9: The tabular data from the adiabatic flame temperature function for coal with 15% added hydrogen.

Excess air ratio	**Adiabatic flame temperature (°C)**	**H_2O composition (vol%)**	**CO_2 composition (vol%)**
1.00	1988	8.20	16.2
1.50	1854	5.50	11.0
2.00	1757	4.20	8.30
2.50	1684	3.40	6.70
3.00	1628	2.80	5.60
3.50	1583	2.40	4.80
4.00	1547	2.10	4.20
4.50	1517	1.90	3.70
5.00	1491	1.70	3.40
5.50	1470	1.50	3.10

Table B.10: The tabular data from the adiabatic flame temperature function for coal with 20% added hydrogen.

Excess air ratio	**Adiabatic flame temperature (°C)**	**H_2O composition (vol%)**	**CO_2 composition (vol%)**
1.00	2022	9.80	15.2
1.50	1880	6.70	10.3
2.00	1778	5.10	7.80
2.50	1702	4.10	6.30
3.00	1644	3.40	5.30
3.50	1597	2.90	4.50
4.00	1559	2.60	4.00
4.50	1528	2.30	3.50
5.00	1501	2.10	3.20
5.50	1479	1.90	2.90

B. Figures